POLITECNICO DI MILANO

Facoltà di Ingegneria Industriale e dell'Informazione

Corso di Laurea Magistrale in Ingegneria Biomedica

POLITECNICO
MILANO 1863

ASSESSMENT OF ASCENDING THORACIC AORTIC ANEURYSM PRIOR AND AFTER VALVE SPARING SURGERY: A PATIENT TAILORED FLUID-STRUCTURE INTERACTION MODEL ENHANCED WITH 4D FLOW MRI

Supervisor: Alberto Redaelli, PhD
Cosupervisor: Alessandro Caimi, PhD
Jonathan Weinsaft, MD

Author:
Guido Nannini
Matr. 905138

Academic Year 2018-2019

Contents

Sommario

Introduzione

Le malattie del sistema cardiovascolare (CVDs) rappresentano la principale causa di morte nel mondo occidentale, provocando circa 17.1 milioni di morti ogni anno (31% delle morti nel mondo). Un terzo dei decessi avviene prematuramente in persone al di sotto dei 70 anni. Le CVDs includono una vasta gamma di patologie (disfunzione cardiaca, malattie delle coronarie, febbre reumatica…), tra queste gli aneurismi dell'aorta toracica (TAA) rappresentano una patologia che affligge 1/10000 persone e causa 152000 morti ogni anno nel mondo. Nel 60% dei casi, i TAA riguardano l'aorta ascendente (aTAA), l'attenzione verrà quindi posta su questi ultimi [1,2].

La procedura chirurgica per l'aTAA consiste nella sostituzione del segmento ascendente con un graft. In genere, anche la valvola aortica è compromessa e viene sostituita con una protesi meccanica o biologica suturata al graft, tuttavia nei pazienti che presentano ancora lembi valvolari aortici sani, è possibile una ricostruzione *valve-sparing* (VSR), cioè "risparmiatrice della valvola". Il "criterio di dimensione" rappresenta il gold standard per decidere se operare un paziente con chirurgia elettiva: si interviene su aneurismi il cui diametro eccede 5.5 cm. La scelta di intervenire o meno è tuttavia arbitraria e dipende dal medico, statisticamente il 31% dei pazienti con aTAA ha delle complicanze severe prima che l'aneurisma raggiunga la dimensione critica [2]. La chirurgia elettiva è una procedura consolidata con un tasso di insuccesso molto basso (0.2%). A 13 anni il tasso di sopravvivenza è ancora >81%, tuttavia possono verificarsi delle complicazioni, principalmente insufficienza della valvola aortica, formazione di un TAA in aorta discendete ed endocarditi acute che portano a febbre reumatica [3]. L'inserimento un graft altera la fluidodinamica del sangue, specialmente in aorta discendente, dove si osservano velocità e sforzi di taglio (WSS) più elevati [4]. L'alterazione dell'emodinamica rappresenta una causa di innesco del processo aterogenico [5-7], perciò la sua analisi può rappresentare un utile strumento nel follow-up clinico. L'approccio più utilizzato per studiare la fluidodinamica postoperativa è la risonanza magnetica con contrasto di fase (PC-MRI o 4D flow). Il 4D flow è una tecnica che permette di effettuare misurazioni *in vivo* delle componenti della velocità del sangue nell'aorta del paziente, da cui è possibile derivare streamlines, WSS ed altre grandezze.

Nonostante le sue potenzialità, il 4D flow ha delle limitazioni: (i) la risoluzione spaziale e temporale sono limitate, (ii) gli artefatti da movimento (e.g. il battito del cuore) non possono essere evitati, (iii) non cattura aspetti del flusso a scale minori della dimensione del voxel. Il WSS viene calcolato come gradiente spaziale di velocità, perciò la misura da 4D flow può essere inaccurata. I modelli numerici possono andare oltre questi limiti e fornire, non solo misure più accurate di WSS ed indici associati, ma anche un'analisi dell'interazione tra parete arteriosa e sangue. In questo lavoro di tesi verrà utilizzato un modello di interazione fluido-struttura (FSI) per comparare l'emodinamica di un paziente prima e dopo una VSR ed analizzare il ruolo del graft in PET nel comportamento strutturale e fluidodinamico dell'aorta a seguito della chirurgia.

Stato dell'arte

Negli ultimi anni si è sviluppato un interesse crescente per la modellazione FSI. In letteratura si possono trovare vari studi [8-17], che si concentrano su configurazioni fisiologiche o patologiche dell'aorta. Savabi *et al*. [17] hanno usato un modello FSI per valutare le forze emodinamiche e la risposta strutturale in prossimità dei barorecettori. La geometria è stata ricostruita da MRI e come condizioni al contorno (BCs) è stato applicata una portata fisiologica (inlet) e un profilo di pressione fisiologico (outlet). La parete è stata assunta elastico-lineare. Il WSS e lo sforzo di von Mises sono risultati più elevati in prossimità dei barorecettori (alle biforcazioni dei rami sopraortici); la deformazione circonferenziale è stata misurata e suggerita come criterio per valutare il funzionamento dei barorecettori. Campobasso *et al.* [8] hanno eseguito una analisi FSI sugli effetti dell'irrigidimento della parte arteriosa. La geometria è stata ricostruita da immagini MRI e come BCs sono stati imposti un profilo di velocità paziente-specifico (inlet), portata paziente specifico (outlet sopraortici) e un modello Windkessel (aorta discendente). La parete è stata assunta elastico-lineare. È stato osservato un incremento dello sforzo in parete all'aumentare della rigidezza della stessa, ed il picco di sforzo è stato suggerito come criterio per valutare il rischio di rottura dell'aneurisma. Mendez *et al.* [9] hanno confrontato diversi approcci di modellazione (fluidodinamica computazionale (CFD) ed FSI). La geometria è stata ricostruita da immagini angiografiche di tomografia computerizzata, la parete aortica è stata assunta anistropa iperelastica e come BCs sono stati applicati un profilo fisiologico (inlet) e dei modelli Windkessel (outlet). I loro risultati suggeriscono che i risultati della CFD e dell'FSI non presentino differenze significative a causa dell'irrigidimento della parete dell'aTAA.

Questi studi mostrano le potenzialità dell'approccio FSI nella procedura clinica, ma presentano aspetti da migliorare: (i) utilizzare un profilo uniforme in ingresso è una sovra-semplificazione, che non considera l'asimmetria della velocità in ingresso. (ii) È stato provato [18] che le BCs di Windkessel sono la miglior opzione che riproduce fedelmente l'emodinamica in aorta. (iii) La geometria dell'aorta deve essere ricostruita interamente (radice, arco, discendente). (iv) Nessuna analisi è stata condotta sulla condizione post-operativa. Al meglio delle conoscenze dell'autore, non è mai stata effettuata una analisi FSI per confrontare l'emodinamica prima e a seguito della chirurgia elettiva per pazienti con aTAA. Ciò ha definito le basi per il seguente lavoro di tesi.

Materiali e metodi

Lo scopo di questo lavoro è realizzare un modello FSI che consista in due simulazioni numeriche: una per la configurazione pre-intervento, l'altra post-intervento. In parallelo al modello FSI è stato sviluppato un modello CFD, per determinare se è possibile ottenere risultati analoghi, con un modello meno costoso. I risultati delle simulazioni numeriche sono stati comparati con un'analisi 4D flow precedentemente condotta. Il workflow adottato è il seguente:

- Acquisizione MRA e PC-MRI
- Segmentazione: le immagini MRA sono state segmentate per ricostruire la geometria.
- Meshing: il dominio fluido e solido sono stati discretizzati in elementi finiti.
- Assegnamento delle proprietà dei materiali: le proprietà del sangue, del tessuto arterioso e del PET sono state reperite in letteratura.
- Condizioni al contorno: il profilo di velocità di ingresso paziente specifico è stato estratto dalla PC-MRI e i parametri di Windkessel sono stati impostati agli outlet.
    - Simulazione FSI (2 cicli)
    - Simulazione CFD (2 cicli)
- Postprocessing

Geometria and mesh

Un'angiografia a risonanza magnetica (MRA) ed un'acquisizione in contrasto di fase (PC-MRI) sono state eseguita prospetticamente su un paziente di 48 anni, prima e dopo l'intervento. Le immagini di MRA sono state segmentate per ricostruire l'STL dell'anatomia, che è stato poi co-registrato alla PC-MRI ed importato in Autodesk Meshmixed. L'STL è stato quindi smussato e

tagliato per generare le sezioni di ingresso e uscita del fluido. La parete è stata estrusa in direzione normale di 2 mm [19,20], per ottenere il dominio solido, cioè la parete arteriosa (**Figura 1**).

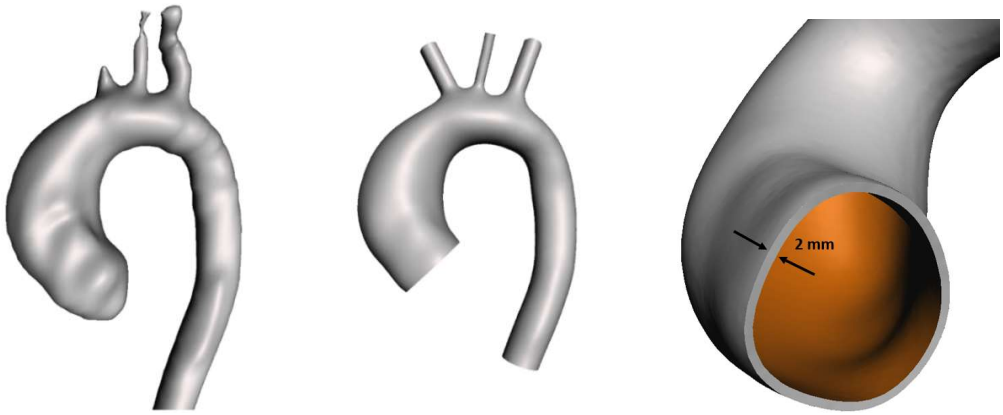

Figura 1. Geometria 3D pre-intervento del dominio fluido, ricostruita dalla segmentazione dell'MRI (a) e corretta in Meshmixer (b). Zoom sull'inlet del domino solido (c).

L'STL dell'anatomia post-intervento è stato sovrapposto alle immagini MRA in ParaView, e tagliato lungo il sito di sutura per generare il graft in PET in aorta ascendente (**Figure 2a**).

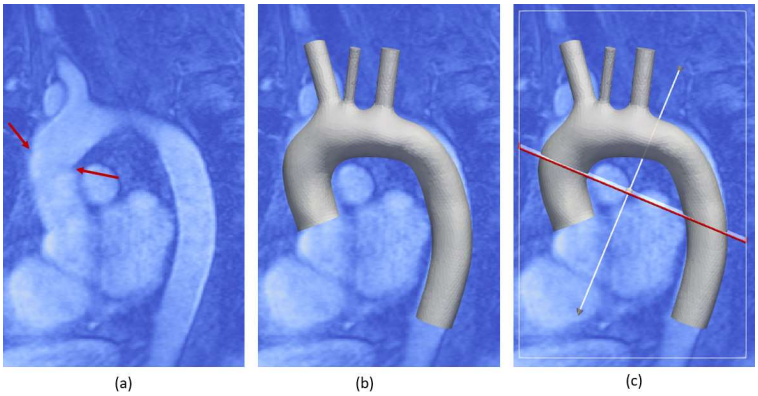

Figura 2. Immagini MRI in cui il sito di sutura è evidenziato con due frecce rosse (a) e geometria STL coregistrata (b). Il piano di taglio è mostrato in (c).

Il dominio fluido e quello solido sono stati discretizzati in ANSYS, dopo un'analisi di sensitività, con ~2.7 milioni e ~500k elementi tetraedrici, rispettivamente (**Figura 3**). La dimensione caratteristica della mesh è 1 mm e 1.25 mm per la mesh fluida e solida rispettivamente. Per la mesh fluida, è stata utilizzata una mesh dinamica, poiché le pareti si deformano durante la simulazione, ottenuta combinando gli schemi *smoothing* e *remeshing* disponibili in ANSYS.

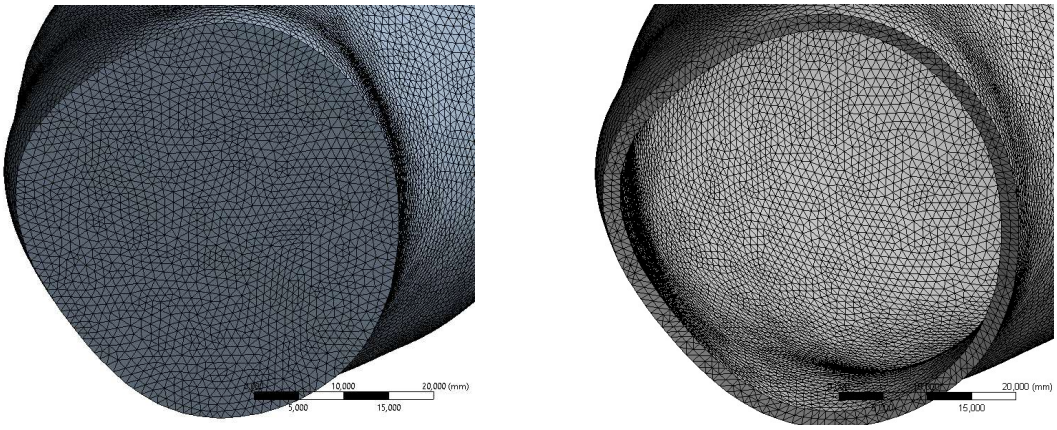

(a) (b)

Figura 3. Viualizzazione della mesh fluida (a) e solida (b). Zoom sull'inltet dell'aorta.

Proprietà dei materiali

Tre materiali interagiscono nel modello: il sangue, la parete arteriosa e il graft in PET. Il sangue è stato modellato come un fluido newtoniano con densità $\rho = 1060$ kg/m^3 [21] e viscosità $\mu = 4$ cP [22]. Il flusso è stato assunto laminare [17]. Il tessuto della parete è stato modellato come un materiale isotropo elastico-lineare, con modulo di Young $E = 1.5$ MPa, coefficiente di Poisson $\nu = 0.4$, e densità $\rho = 1120$ kg/m^3 [23]. Il PET è stato modellato come un materiale isotropo elastico-lineare, con modulo di Young $E = 11.84$ Mpa, coefficiente di Poisson $\nu = 0.3$ e densità pari a 600 kg/m^3 [24].

Condizioni al contorno

Sulla superficie interna del dominio solido è stata imposta un'interfaccia fluido-struttura come condizione di carico; le estremità sono state fissate (spostamento = 0). All'ingresso del dominio fluido è stato assegnato un profilo di velocità paziente specifico ottenuto con un codice MATLAB™ sviluppato dal nostro gruppo. La velocità è stata assegnata attraverso le sue componenti per riprodurre correttamente l'asimmetria e l'inclinazione del profilo entrante (**Figura 4**). Alle uscite è stato assegnato come BC il modello a tre elementi di Windkessel (WK3), che consiste in una resistenza caratteristica (Z), una compliance (C) ed una resistenza distale (R). C ed R sono in parallelo. I parametri del modello WK3 sono stati calcolati con relazioni da letteratura [14, 25-27] e sono riportati in **Tabella I**. Sulla parete del vaso è stata applicata la condizione no-slip (velocità nulla a parete).

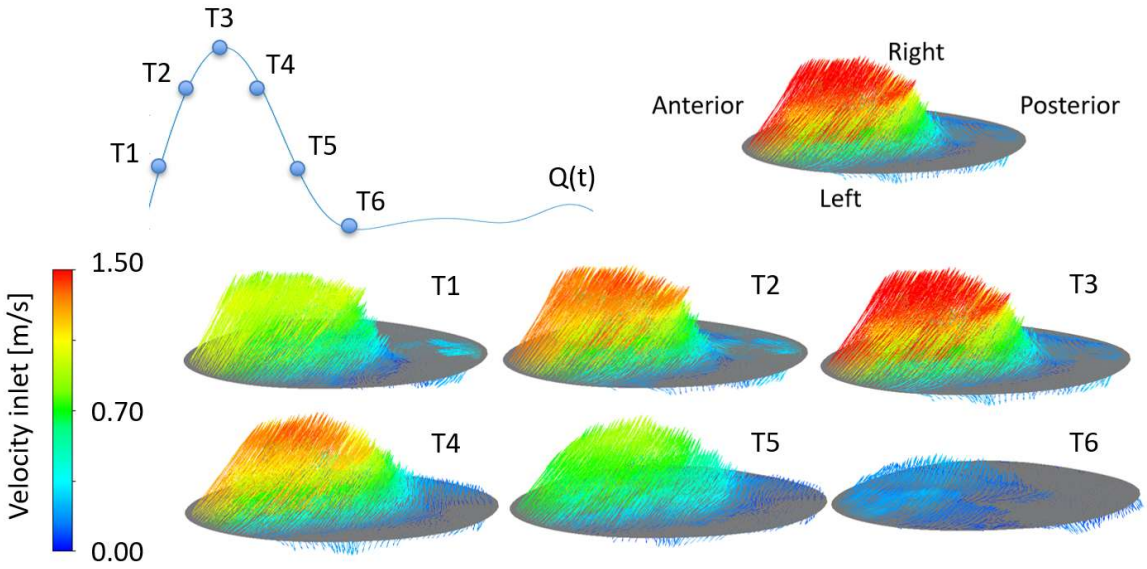

Figura 4. Profilo di velocità in ingresso a diversi istanti del ciclo cardiaco. La figura evidenzia l'asimmetria del profilo: all'estradosso dell'ascendente il sangue ha velocità più elevata.

Outlet	***Z***	***C***	***R***
BCA	5.39×10^{7}	2.14×10^{-9}	7.62×10^{8}
LCCA	1.35×10^{8}	1.00×10^{-9}	1.61×10^{9}
LSA	5.68×10^{7}	1.14×10^{-9}	1.47×10^{9}
DAO	1.08×10^{7}	1.00×10^{-8}	1.64×10^{8}

Outlet	***Z***	***C***	***R***
BCA	3.33×10^{7}	3.23×10^{-9}	5.08×10^{8}
LCCA	1.14×10^{8}	1.51×10^{-9}	1.05×10^{9}
LSA	5.29×10^{7}	1.72×10^{-9}	9.63×10^{8}
DAO	1.04×10^{7}	1.51×10^{-8}	1.06×10^{8}

Tabella I. Valori utilizzati per il modello Windkessel (pre-intervento a sinistra, post a destro). I valori sono riportati in unità S.I., Pa·s/m^3 per le resistenze e m^3/Pa per le compliance.

Soluzione numerica

L'analisi FSI è stata condotta in ANSYS v.17.2 (ANSYS Inc., Canonsburg, PA, USA), con un *time step* di 1 ms, accoppiando il solutore strutturale (ANSYS Mechanical) e quello fluido (ANSYS Fluent), con il tool System Coupling, incluso nel pacchetto ANSYS. È stata adottata la descrizione cinematica ALE. Le simulazioni di due cicli cardiaci hanno richiesto una media di 10 giorni, utilizzando 24 CPU.

Il solutore strutturale scelto utilizza lo schema di Newton-Raphson per risolvere l'equazione che governa il problema agli elementi finiti nell'approccio agli spostamenti:

$$\mathbf{M}\,\ddot{\bar{u}} + \mathscr{C}\,\dot{\bar{u}} + \mathbf{K}\,\bar{u} = \bar{\mathbf{f}}, \qquad \text{con } \mathscr{C} = 5650 \cdot \mathbf{M} + 0.1 \cdot \mathbf{K} \tag{1}$$

Dove **M**, $\mathscr{C}$ e **K** sono rispettivamente le matrici di massa, viscosa e di rigidezza, $\bar{\mathbf{f}}$ è il vettore di carico e $\bar{\ddot{\boldsymbol{u}}}$, $\bar{\dot{\boldsymbol{u}}}$ e $\bar{\boldsymbol{u}}$ sono l'accelerazione, la velocità e lo spostamento nodale. La matrice viscosa è definita tramite uno smorzamento di Rayleigh [28].
Il solutore fluido utilizza l'algoritmo PISO (*Pressure-Implicit with Splitting of Operators*) per risolvere le equazioni di continuità e di Navier Stokes nella configurazione ALE.

$$\begin{cases} \rho\left(\frac{\partial \mathbf{v}}{\partial t} + \left(\left(\mathbf{v} - \mathbf{v}_{\mathrm{g}}\right) \cdot \nabla\right)\mathbf{v}\right) = -\nabla p + \mu \nabla^2 \mathbf{v} \\ \nabla \cdot \mathbf{v} = 0 \end{cases} \tag{2}$$

Dove ρ è la densità del fluido, $\mathbf{v}$ la velocità, $\mathbf{v}_{\mathrm{g}}$ la velocità della mesh, p la pressione e μ la viscosità dinamica.

Simulazioni CFD

In parallelo alla simulazione FSI è stata eseguita un'analisi CFD con le stesse BCs per confrontare i risultati. Inoltre, è stata condotta una analisi di sensitività delle condizioni al contorno di ingresso sul modello pre-operazione, testando tre diversi profili di ingresso: uno piatto, uno parabolico e uno paziente specifico.

Postprocessing

Il WSS è stato confrontato al picco sistolico (in occorrenza del massimo) tra i modelli pre e post-intervento. Il WSS gioca un ruolo fondamentale nell'innesco del processo aterogenico, specialmente se cambia in modulo e direzione nel tempo [5,6], pertanto è stato calcolato l'OSI (*oscillatory shear index*). Lo sforzo medio percepito dalla parete arteriosa è invece espresso dal TAWSS (*time average WSS*). Le velocità sono state visualizzate come streamlines e mappe su dei piani di sezione, per confrontare i risultati delle simulazioni numeriche con il 4D flow. La pressione è stata estratta all'ingresso del modello e confrontata con quella sistolica e diastolica misurata clinicamente. Lo sforzo principale, la deformazione principale e lo spostamento della parete arteriosa sono stati confrontati qualitativamente, con mappe di distribuzione.

Risultati

Sensitività alle condizioni di ingresso

Il confronto delle streamlines in aorta ascendente con mostra un pattern molto diverso nel caso dei profili piatto e parabolico rispetto al 4D flow, mentre c'è un buon accordo nel caso del profilo di

velocità paziente specifico: solo questo riproduce correttamente l'asimmetria del profilo di ingresso ed i vortici che si formano in ascendente, nel corretto range di velocità (**Figura 5**).

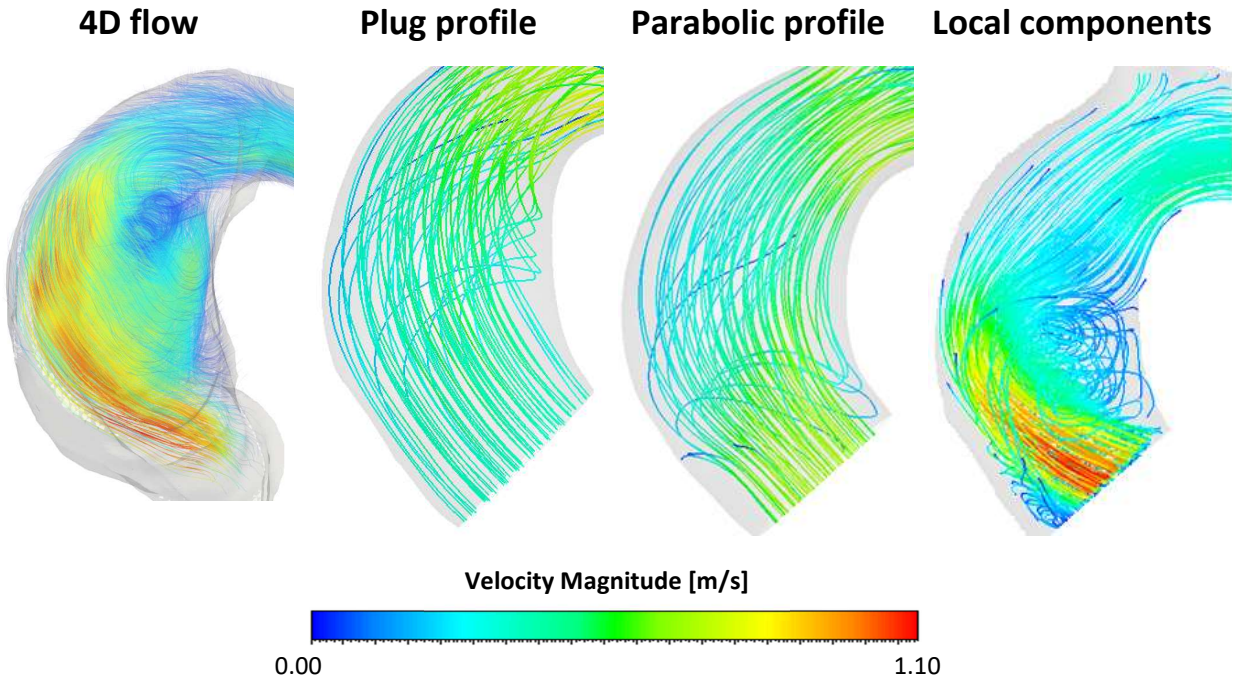

Figura 5. Streamlines al picco sistolico ottenute con 4D flow e 3 simulazioni CFD con diverse condizioni di ingresso. Solo la CFD paziente specifico è in grado di riprodurre correttamente il pattern in ascendente.

Sensitività al metodo risolutivo: FSI v. CFD

Il confronto tra le velocità ottenute da 4D flow, FSI e CFD è stato fatto su 6 piani di sezione (3 in ascendente e 3 in discendente) con un'ANOVA. Sia nel caso pre-intervento che post-intervento, non è stata rilevata una differenza statistica ($p>0.05$) tra le velocità da FSI e da 4D flow, mentre è stata osservata una differenza marcata tra CFD e 4D flow, specialmente in aorta discendente, sia nel modello pre-intervento (in cui la differenza è maggiore) che post-intervento (**Figura 6**).

Le steamlines sono state confrontate al picco sistolico tra FSI e 4D flow. Nel modello pre-operazione è stato osservato un buon accordo tra le due, con una corretta inclinazione e asimmetria del profilo di ingresso e formazione di vortici all'intradosso dell'aorta ascendente. Il pattern di streamlines è concorde anche nel modello post-operazione, che mostra un flusso sostenuto senza ricircoli.

Inoltre, è stato effettuato un confronto qualitativo tra le mappe di velocità sui piani di sezione dell'aorta. In generale si osserva una buona riproduzione del pattern di velocità con velocità più elevate nel modello CFD (**Figura 7**).

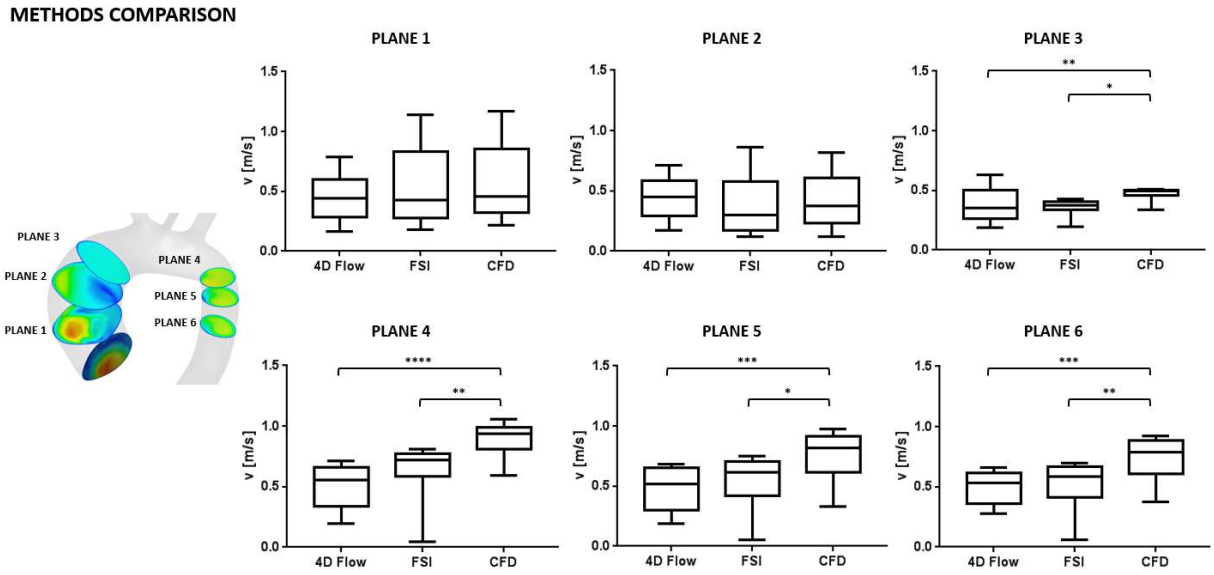

Figura 6. ANOVA della distribuzione di velocità su 6 piani di sezione: 4D flow v. FSI v. CFD. Gli asterischi indicano il *p*-value: * = $p<0.05$, ** = $p<0.01$, *** = $p<0.001$ and **** = $p<0.0001$.

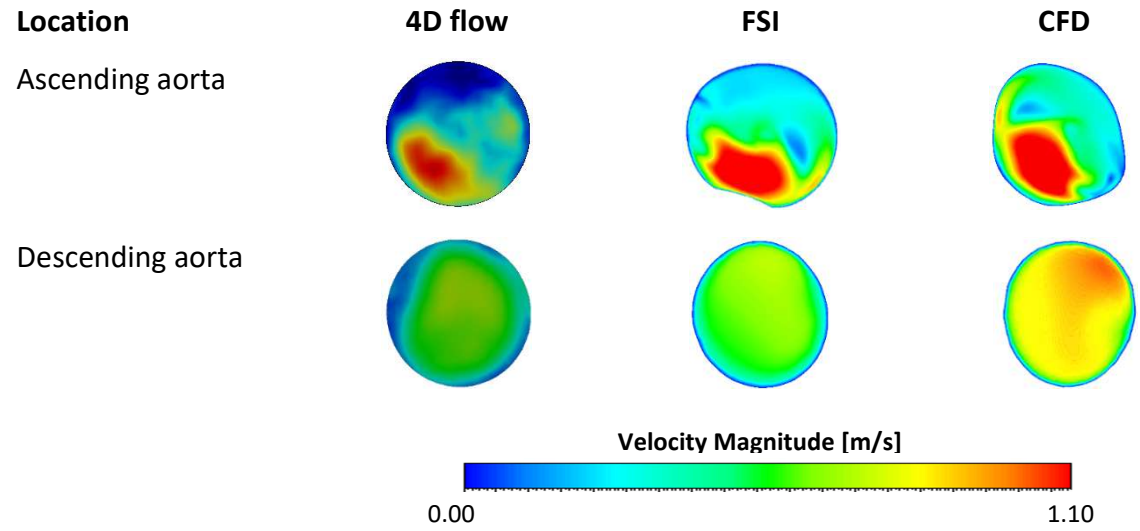

Figura 7. Pattern di velocità su due piani di sezione (in ascendente e discendente) per il modello pre-operazione.

Pre-intervento vs. post-intervento

Il WSS sistolico assume un valore massimo in aorta discendente maggiore del 28% nel caso post, rispetto al modello pre-intervento. È stata osservata una distribuzione di OSI con valori più elevati nel modello pre-intervento, con OSI prossimi a 0.5 (soglia critica) in aorta ascendente e all'intradosso della discendente. La distribuzione di TAWSS non rivela differenza significativa (**Figura 8**). È stato effettuato un *t*-test delle distribuzioni di WSS, OSI e TAWSS in aorta discendete, trovando WSS significativamente ($p<0.001$) più elevati ed OSI significativamente

minori ($p<0.01$) nel modello post-intervento. La distribuzione del TAWSS non mostra differenza statistica significativa tra i due casi (**Figura 9**).

Lo sforzo in parete risulta significativamente alterato nel modello post-intervento: lungo il sito di sutura del graft si osserva un'intensificazione degli sforzi con valori di circa 500kPa, causata dal mismatch di compliance tra graft e parete arteriosa.

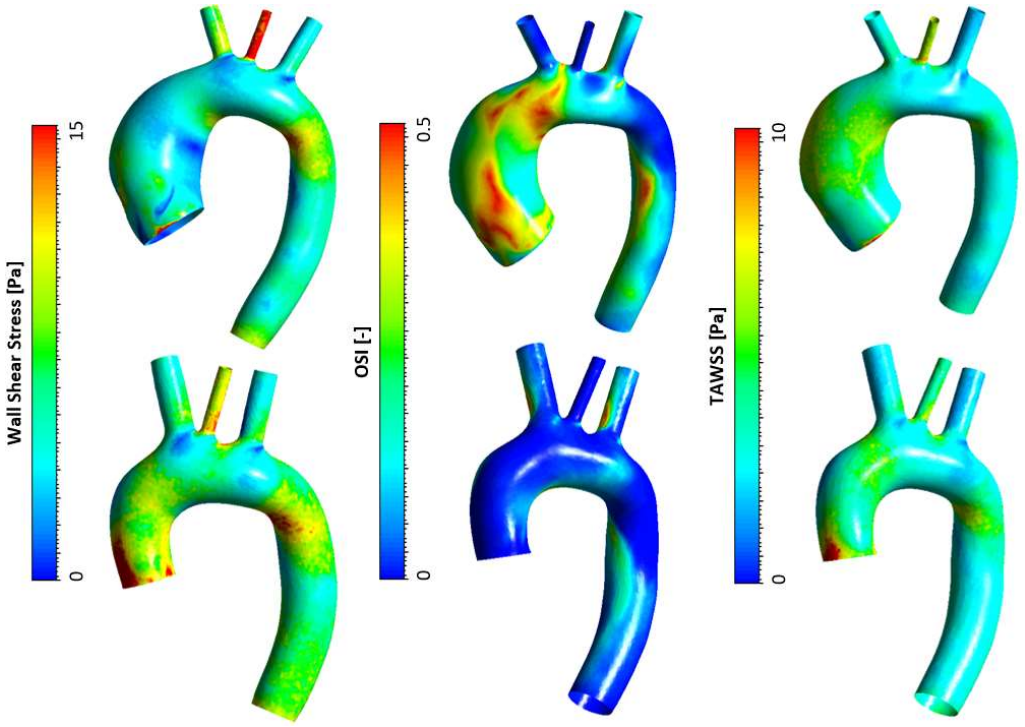

Figura 8. Distribuzione di WSS, OSI e TAWSS ottenuti dall'analisi FSI. Configurazione pre-intervento (riga superiore) e post-intervento (riga inferiore).

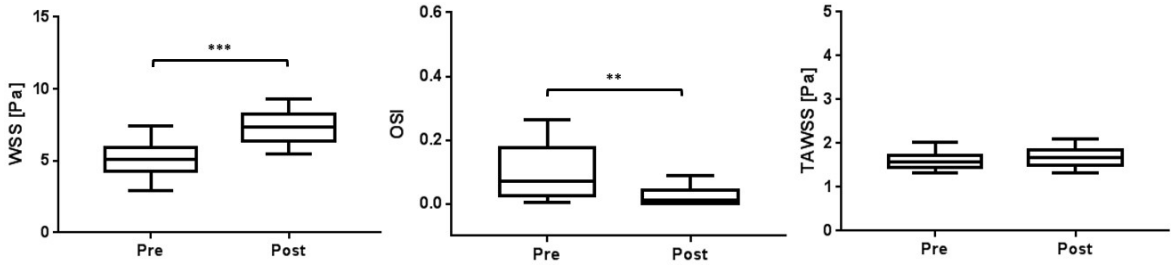

Figura 9. *t*-test della distribuzione di WSS, OSI e TAWSS ottenuti dall'analisi FSI in discendente. Gli asterischi indicano il *p*-value: * = $p<0.05$, ** = $p<0.01$, *** = $p<0.001$ and **** = $p<0.0001$.

Discussione

Con questo lavoro di tesi, si è sviluppato un approccio innovativo per la valutazione dell'emodinamica in pazienti operati con chirurgia VSR per aTAA. È stato utilizzato un modello FSI combinato con la PC-MRI, per una fedele riproduzione della biomeccanica aortica.

Il confronto dei risultati dell'FSI con il 4D flow ha fornito una validazione del modello ed ha mostrato che la CFD, anche se ben condizionata, è un approccio sovra-semplificato. Per riprodurre correttamente la biomeccanica dell'aorta, è necessaria un'analisi FSI.
Il confronto tra diverse condizioni di ingresso del flusso ha mostrato che soltanto un profilo paziente specifico riproduce correttamente tutti gli aspetti emodinamici in ascendente.
Il risultato del confronto tra pre e post-intervento è in accordo con precedenti studi condotti con l'analisi 4D flow [4]: le velocità e il WSS aumentano notevolmente in discendente dopo la chirurgia VSR. Alti WSS in discendente rappresentano un fattore di rischio per l'innesco del processo aterogenico e quindi la formazione di un TAA. La distribuzione di OSI presenta valori significativamente più bassi nel modello post-intervento, con valore massimo all'intradosso della discendente. Pertanto, dopo la chirurgia VSR, l'aorta discendente rappresenta la regione di maggiore rischio per la formazione di un TAA. L'intensificazione degli sforzi lungo il sito di sutura è un aspetto significante: il compliance-mismatch dovuto al cambio repentino di rigidezza dei tessuti causa un significativo aumento dello sforzo. Precedenti studi [38] hanno suggerito che il picco di sforzo a parete come parametro per valutare il rischio di accrescimento e rottura dell'aneurisma, pertanto un approfondimento di questo aspetto è auspicabile.

Conclusioni

Il modello FSI sviluppato fornisce un'analisi approfondita della biomeccanica di una aorta patologica e poi ricostruita con operazione VSR. Il modello è in grado di riprodurre le condizioni di lavoro dell'aorta del paziente e permette di analizzare sia aspetti fluidodinamici che strutturali.
Il confronto tra approccio FSI e CFD ha dimostrato che una semplice CFD fornisce risultati non attendibili (sovrastimati). Inoltre, si è dimostrato che l'abilità nel riprodurre correttamente la fluidodinamica aortica non dipende soltanto dalle corrette condizioni al contorno di ingresso, ma anche dal tipo di approccio numerico adottato.
Questo lavoro getta le basi per una promettente metodologia per l'ottimizzazione della procedura chirurgica per il trattamento degli aTAA, essendo in grado di prevedere – per uno specifico paziente – le regioni in cui la fluidodinamica risulta alterata e, di conseguenze, il rischio di innesco del processo aterogenico è più elevato. Sviluppi futuri per questo lavoro potrebbero consistere nel riprodurre il workflow proposto su un più ampio gruppo di pazienti ed indagare gli effetti che diversi tipi di graft (e.g. diversa lunghezza, rigidezza…) inducono.

Bibliografia

[1] “World Health Organization.” [Online]. Available: https://www.who.int/health-topics/cardiovascular-diseases/#tab=tab_1.

[2] K. H. Chau and J. A. Elefteriades, “Natural history of thoracic aortic aneurysms: Size matters, plus moving beyond size,” Prog. Cardiovasc. Dis., vol. 56, no. 1, pp. 74–80, 2013, doi: 10.1016/j.pcad.2013.05.007.

[3] R. De Paulis et al., “Long-term results of the valve reimplantation technique using a graft with sinuses,” J. Thorac. Cardiovasc. Surg., vol. 151, no. 1, pp. 112–119, 2016, doi: 10.1016/j.jtcvs.2015.08.026.

[4] M. Gaudino, C. Lau, M. Munjal, D. Avgerinos, and L. N. Girardi, “Contemporary outcomes of surgery for aortic root aneurysms: A propensity-matched comparison of valve-sparing and composite valve graft replacement,” J. Thorac. Cardiovasc. Surg., vol. 150, no. 5, pp. 1120-1129.e1, 2015, doi: 10.1016/j.jtcvs.2015.07.015.

[5] J. M. Zhang, L. P. Chua, D. N. Ghista, S. C. M. Yu, and Y. S. Tan, “Numerical investigation and identification of susceptible sites of atherosclerotic lesion formation in a complete coronary artery bypass model,” Med. Biol. Eng. Comput., vol. 46, no. 7, pp. 689–699, 2008, doi: 10.1007/s11517-008-0320-4.

[6] D. N. Ku, D. P. Giddens, C. K. Zarins, and S. Glagov, “Pulsatile flow and atherosclerosis in the human carotid bifurcation. Positive correlation between plaque location and low and oscillating shear stress,” Arteriosclerosis, vol. 5, no. 3, pp. 293–302, 1985, doi: 10.1161/01.atv.5.3.293.

[7] H. Meng, V. M. Tutino, J. Xiang, and A. Siddiqui, “High WSS or Low WSS? Complex interactions of hemodynamics with intracranial aneurysm initiation, growth, and rupture: Toward a unifying hypothesis,” Am. J. Neuroradiol., vol. 35, no. 7, pp. 1254–1262, 2014, doi: 10.3174/ajnr.A3558.

[8] R. Campobasso, F. Condemi, M. Viallon, P. Croisille, S. Campisi, and S. Avril, “Evaluation of Peak Wall Stress in an Ascending Thoracic Aortic Aneurysm Using FSI Simulations: Effects of Aortic Stiffness and Peripheral Resistance,” Cardiovasc. Eng.

[9] V. Mendez, M. Di Giuseppe, and S. Pasta, “Comparison of hemodynamic and structural indices of ascending thoracic aortic aneurysm as predicted by 2-way FSI, CFD rigid wall

simulation and patient-specific displacement-based FEA," Comput. Biol. Med., vol. 100, no. May, pp. 221–229, 2018, doi: 10.1016/j.compbiomed.2018.07.013.

[10] F. Cuomo, S. Roccabianca, D. Dillon-Murphy, N. Xiao, J. D. Humphrey, and C. A. Figueroa, "Effects of age-associated regional changes in human central artery mechanics on systemic hemodynamics revealed by computational modeling," PLoS One, vol. 12, no. 3, pp. 1–21, 2017, doi: 10.7302/Z24B2Z7Z.

[11] T. Khamdaeng and P. Terdtoon, "Regional pulse wave velocity and stress in aneurysmal arch-shaped aorta," Biomed. Mater. Eng., vol. 29, no. 4, pp. 527–549, 2018, doi: 10.3233/BME-181007.

[12] R. Jayendiran, B. Nour, and A. Ruimi, "Fluid-structure interaction (FSI) analysis of stent-graft for aortic endovascular aneurysm repair (EVAR): Material and structural considerations," J. Mech. Behav. Biomed. Mater., vol. 87, no. May, pp. 95–110, 2018, doi: 10.1016/j.jmbbm.2018.07.020.

[13] C. J. Drewe, L. P. Parker, L. J. Kelsey, P. E. Norman, J. T. Powell, and B. J. Doyle, "Haemodynamics and stresses in abdominal aortic aneurysms: A fluid-structure interaction study into the effect of proximal neck and iliac bifurcation angle," J. Biomech., vol. 60, pp. 150–156, 2017, doi: 10.1016/j.jbiomech.2017.06.029.

[14] N. Xiao, J. Alastruei, and C. A. Figueroa, "A systematic comparison between 1-D and 3-D hemodynamicsin compliant arterial models," Int. Journey Numer. methods Biomed. Eng., 2014.

[15] S. Lin, X. Han, Y. Bi, S. Ju, and L. Gu, "Fluid-structure interaction in abdominal aortic aneurysm: Effect of modeling techniques," Biomed Res. Int., vol. 2017, 2017, doi: 10.1155/2017/7023078.

[16] P. Reymond, P. Crosetto, S. Deparis, A. Quarteroni, and N. Stergiopulos, "Physiological simulation of blood flow in the aorta: Comparison of hemodynamic indices as predicted by 3-D FSI, 3-D rigid wall and 1-D models," Med. Eng. Phys., vol. 35, no. 6, pp. 784–791, 2013, doi: 10.1016/j.medengphy.2012.08.009.

[17] R. Savabi, M. Nabaei, S. Farajollahi, and N. Fatouraee, "Fluid structure interaction modeling of aortic arch and carotid bifurcation as the location of baroreceptors," Int. J. Mech. Sci., vol. 165, no. July 2019, 2020, doi: 10.1016/j.ijmecsci.2019.105222.

[18] S. Pirola et al., “On the choice of outlet boundary conditions for patient-specific analysis of aortic flow using computational fluid dynamics,” J. Biomech., vol. 60, pp. 15–21, 2017, doi: 10.1016/j.jbiomech.2017.06.005.

[19] C.-Y. Liu, D. Chen, D. A. Bluemke, and W. G. Hundley, “Evolution of aortic wall thickness and stiffness with atherosclerosis: Long-term follow up from the Multi-Ethnic Study of Atherosclerosis (MESA),” HHS Public Access, vol. 69, no. 1, pp. 110–120, 2015, doi: 10.1016/j.socscimed.2009.04.010.Are.

[20] W. Karel van den Hengel, “Abdominal aortic wall thickness and compliance The possibilities to measure and the effect of variation in the analysis of aneurysms,” Blood, no. April, 2008.

[21] J. D. Cutnell and K. W. Johnson, Physics (4th Edition, Volume 1). 1997.

[22] L. Dintenfass, Blood Viscosity, Hyperviscosity & Hyperviscosaemia. Springer Science & Business Media, 1985.

[23] T. Khamdaeng, J. Luo, J. Vappou, P. Terdtoon, and E. E. Konofagou, “Arterial stiffness identification of the human carotid artery using the stress – strain relationship in vivo,” Ultrasonics, vol. 52, no. 3, pp. 402–411, 2012, doi: 10.1016/j.ultras.2011.09.006.

[24] G. Tasca et al., “Aortic Root Biomechanics After Sleeve and David Sparing Techniques: A Finite Element Analysis,” Ann. Thorac. Surg., vol. 103, no. 5, pp. 1451–1459, 2017, doi: 10.1016/j.athoracsur.2016.08.003.

[25] J. F. Ladisa et al., “Computational simulations for aortic coarctation: Representative results from a sampling of patients,” J. Biomech. Eng., vol. 133, no. 9, 2011, doi: 10.1115/1.4004996.

[26] A. S. Les et al., “Quantification of hemodynamics in abdominal aortic aneurysms during rest and exercise using magnetic resonance imaging and computational fluid dynamics,” Ann. Biomed. Eng., vol. 38, no. 4, pp. 1288–1313, 2010, doi: 10.1007/s10439-010-9949-x.

[27] P. Reymond, F. Merenda, F. Perren, D. Rüfenacht, and N. Stergiopulos, “Validation of a one-dimensional model of the systemic arterial tree,” Am. J. Physiol. - Hear. Circ. Physiol., vol. 297, no. 1, pp. 208–222, 2009, doi: 10.1152/ajpheart.00037.2009.

[28] T. E. Tezduyar, S. Sathe, T. Cragin, B. Nanna, and M. Schwaa, “Modelling of fluid–structure interactions with the space–time finite elements: Arterial fluid mechanics,” Int. J. Numer. Methods Fluids, vol. 54, no. October 2010, pp. 901–922, 2007, doi: 10.1002/fld.

Abstract

Introduction

Cardiovascular diseases (CVDs) represent the leading cause of death in the Western World, taking approximatively 17.1 million lives each year (31% of all death worldwide). One third of deaths occur prematurely in people under 70 years of age. CVDs include a wide range of pathologies (heart disorders, coronary disease, rheumatic fever…), among these thoracic aortic aneurysm (TAA) represents a condition affecting ~1/10000 persons that causes 152000 deaths per year worldwide. Since TAAs of the ascending aorta (aTAA), represent 60% of aortic aneurysms, the focus will be shifted on them [1] [2].

Surgical procedure for the treatment of aTAA consists in composite graft replacement of the ascending segment. Generally, the aortic valve is compromised too and gets substituted with a mechanical or biological valve sutured to the graft, however in patients that still have normal aortic valve leaflets, a valve-sparing reconstruction (VSR) is possible. The "dimensional criterion" represent the gold standard to decide whether to operate a patient with elective surgery: patients with aneurysm larger than 5.5 cm must be operated. However, the choice to intervene is arbitrary and depends on the physician and statistically, 31% of patients affected by aTAA suffer from acute complication before the aneurysm reaches its critical size [2].

Elective surgery for the reconstruction of the ascending aorta is a consolidated procedure with very low unsuccess rate (0.2%). At 13 years from the surgery, the survival rate is still >81%, however some complications may occur, mainly including aortic valve insufficiency, descending TAA formation and acute endocarditis that may lead to rheumatic fever [3]. The implantation of a prosthetic graft causes alteration in blood fluid dynamics, especially in the descending aorta, where higher velocities and wall shear stress (WSS) can be observed [4]. Altered hemodynamics represents one of the causes of the atherogenic process starting [5-7], thus, its analysis can be a useful tool in clinical follow up. The most common tool exploited to study postsurgical fluid dynamics in patient treated for aTAA is phase contrast magnetic resonance imaging (PC-MRI, or 4D flow). 4D flow is a technique that permits an *in vivo* measurement of velocity field in the patient's aorta, from which streamlines, WSS, etc. can be derived.

Despite its potentialities, 4D flow has some limitations: (i) spatial resolution is limited (temporal too), (ii) motion artifacts cannot be avoided (e.g. heart motion), (iii) fails to capture aspect of the flow at sub-voxel scale. WSS is derived from spatial gradient of velocity, thus 4D flow results may be not accurate. Numerical models can go beyond these limitations and provide not only accurate values of WSS and related indexes, but also a deep insight into the interaction between the arterial wall and blood. In this work of thesis, a fluid-structure interaction (FSI) approach will be exploited to compare the hemodynamics of a patients prior and after VSR, and deepen the role played by the graft in the structural and fluid dynamic behavior of the aorta after the surgery.

State of Art

In the last years, a growing interest developed for FSI aortic modeling. In literature various works can be found [8-17], focusing on the physiologic or pathologic configuration of the aorta. Savabi *et al*. [17] used an FSI approach to assess the hemodynamic forces and structural response in proximity of baroceptors. They reconstructed the geometry of the aorta from MRI images and applied as boundary conditions physiological flow rate (inlet) and pressure (outlets) waveforms. Wall was assumed linear elastic. Wall shear stresses and Von-Mises stresses were found to be higher in the bifurcations of supra-aortic branches; circumferential stretch was measured and proposed as criterion for baroceptors functioning. Campobasso *et al.* [8] performed an FSI analysis on the effect of the stiffening of the arterial wall. The geometry of the proximal thoracic aorta was reconstructed from MRI images and the following boundary conditions were set: a patient specific velocity profile (inlet), patient specific flow rates (supra-aortic outlets) and Windkessel model (descending aorta). Arterial wall was assumed linear elastic. They observed an increase in wall stress when the aortic wall became stiffer and thus, proposed the peak wall stress as a risk evaluation parameter for the rupture of the aneurysm. Mendez *et al.* [9] compared different modeling approaches (computational fluid dynamics (CFD) and FSI). The geometry was reconstructed from electrocardiogram-gated computed tomography angiography, the aortic wall was assumed anisotropic hyperelastic and the following boundary conditions were set: a flow rate from literature (inlet) and Windkessel models (outlets). Their findings suggested that, due to wall stiffening, the results provided by CFD and FSI are not significantly different.

These studies show the potentialities that FSI approach may offer in clinical procedures but presented aspects to be improved: (i) Using a uniform flow rate waveform as inlet boundary

conditions is a simplified assumption that neglects the skewness of the inlet velocity profile. (ii) It has been proven in other works [18] that Windkessel outlet boundary conditions are the best option to properly replicate the hemodynamics in the aorta. (iii) The aorta must be reconstructed entirely (root, arch, descending). (iv) No study has been carried on the postsurgical configuration. To the best of author's knowledge, no FSI analysis has been conducted to compare the hemodynamics before and after elective surgery for aTAA patients. This set the basis for the current thesis work.

Material and Methods

This work of thesis aims to develop an FSI model consisting in two numerical simulations: one reproducing the presurgical condition, the other reproducing the postsurgical. In parallel with the FSI model, a CFD model was developed, to determine whether is possible or not to obtain similar results with a less expensive model. Results from numerical simulations were compared with 4D flow analysis. The workflow that was adopted is the following:

- MRA and PC-MRI acquisition.
- Segmentation: MRA images were segmented to reconstruct the geometry.
- Meshing: the solid and fluid domain were discretized in finite elements.
- Material properties assignment: properties of blood, arterial tissue and PET were found in literature.
- Boundary conditions: patient specific inlet velocity was extracted from PC-MRI and Windkessel parameters were tuned for the outlets.
    - FSI simulations (2 cycle)
    - CFD simulations (2 cycle)
- Postprocessing

Geometry and meshing

Magnetic resonance angiography (MRA) and phase contrast acquisition (PC-MRI) were prospectively performed, on a 48-years-old male patient, pre and post-operatively. Segmentation was performed on MRA images to reconstruct the STL of the anatomy, that was co-registered to PC-MRI and imported in Autodesk Meshmixer. The STL was smoothed and cut to generate flow inlet and outlets. The wall was extruded in normal direction by 2 mm [19-20], to generate the solid domain (i.e. aortic wall). **Figure 1** illustrates the resulting geometry.

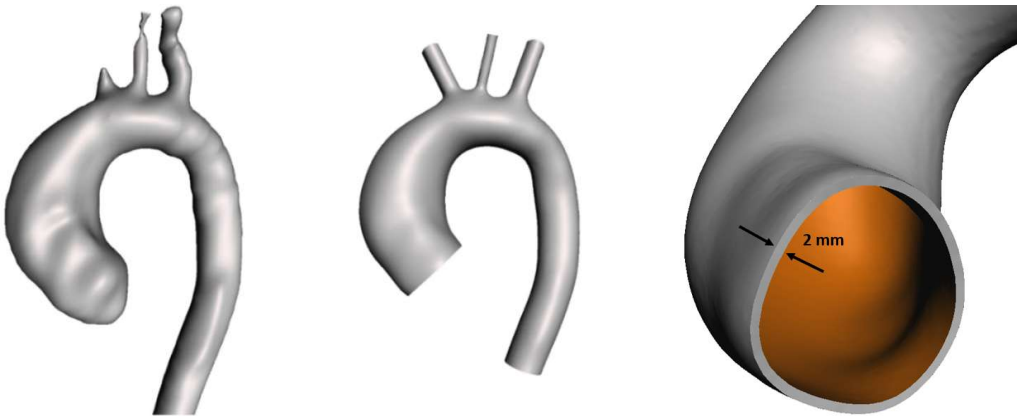

Figure 1. Presurgical 3D geometry of the fluid domain reconstructed through segmentation of MRI (a) and then adjusted in Meshmixer (b). Zoom-in of the inlet of the solid domain (c).

The postsurgical STL was overlapped to MRA images in ParaView, to cut it along the suture site and generate the PET graft in the ascending segment (**Figure 2a**).

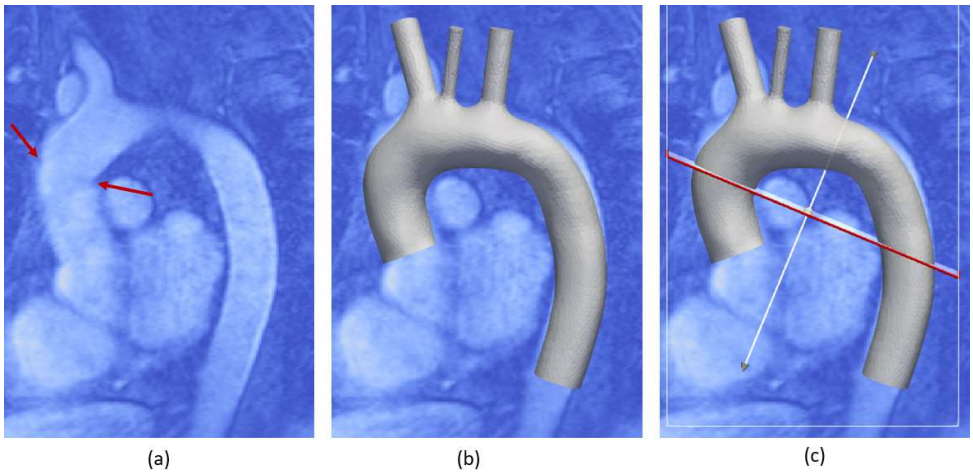

Figure 2. Figure shows MRI images where suture site is highlighted by the red arrows (a) and the STL geometry co-registered (b). The slicing plane is showed in (c).

The solid and fluid domain were discretized in ANSYS – after a sensitivity analysis – with ~2.7 million and ~500k tetrahedral elements respectively (**Figure 3**). The average size of the elements is 1 mm for the fluid mesh and 1.25 mm for the structural mesh. Dynamic meshing was exploited for the fluid mesh, since the wall deforms throughout the simulation. A combination of the smoothing (spring constant = 0.1) and remeshing (maximum cell skewness =0.85, face skewness = 0.8, length scale = 0.5–1.5 mm) scheme was adopted.

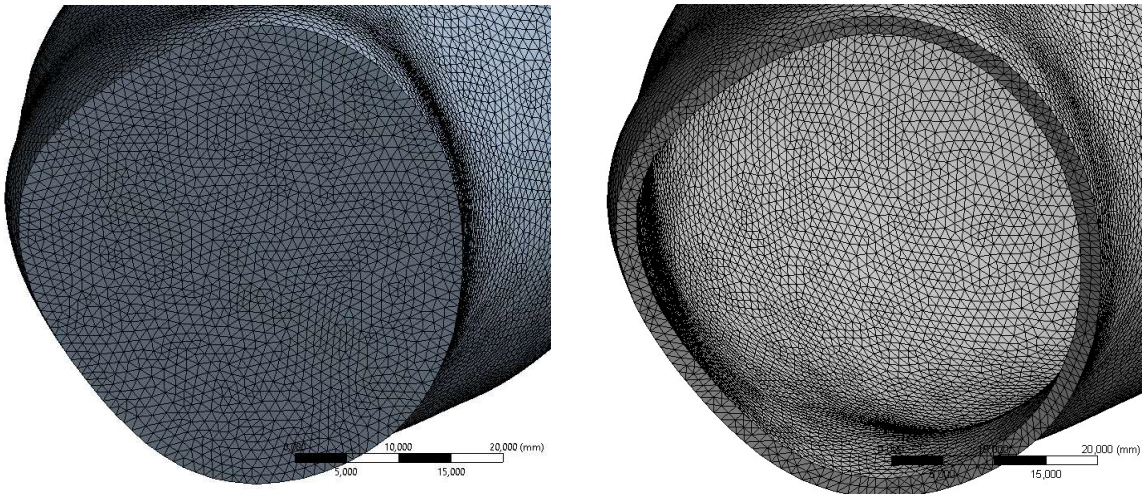

(a) (b)

Figure 3. Viualization of the computational mesh of the fluid (a) and solid (b) domain. Zoom-in on the aortic inlet.

Material properties

Three materials interact in the model: blood (that was treated as a fluid), arterial wall tissue and PET graft. Blood was modeled as a Newtonian fluid with a density $\rho = 1060$ kg/m^3 [21] and a viscosity equal to $\mu = 4$ cP [22]. Flow was assumed to be laminar [17]. Arterial wall tissue was modeled as an isotropic linear elastic material, with a Young's modulus $E = 1.5$ MPa, a Poisson ratio $\nu = 0.4$, a density $\rho = 1120$ kg/m^3 [23]. PET was modeled as an isotropic linear elastic material, with a Young's modulus $E = 11.84$ MPa and a Poisson ratio $\nu = 0.3$ and density equal to 600 kg/m^3 [24].

Boundary conditions

At the inner surface of the solid domain, a fluid-solid interface was applied as load condition; at each extremity, no displacement was allowed. At the inlet of the fluid domain, a patient specific velocity profile – obtained through an in-house MATLAB™ code – was assigned. Velocity was set through its components to reliably reproduce the skewness of the profile and its inflow angle (**Figure 4**). The three-elements Windkessel (WK3) model – consisting in a proximal (or characteristic) resistance Z, a capacitor C and a distal resistance R (C and R are in parallel) – was set as boundary condition at each outlet. The WK3 parameters were evaluated through equations from literature [14,25-27] and are summarized in **Table I**. On the wall of the fluid domain, the no-slip boundary condition was applied.

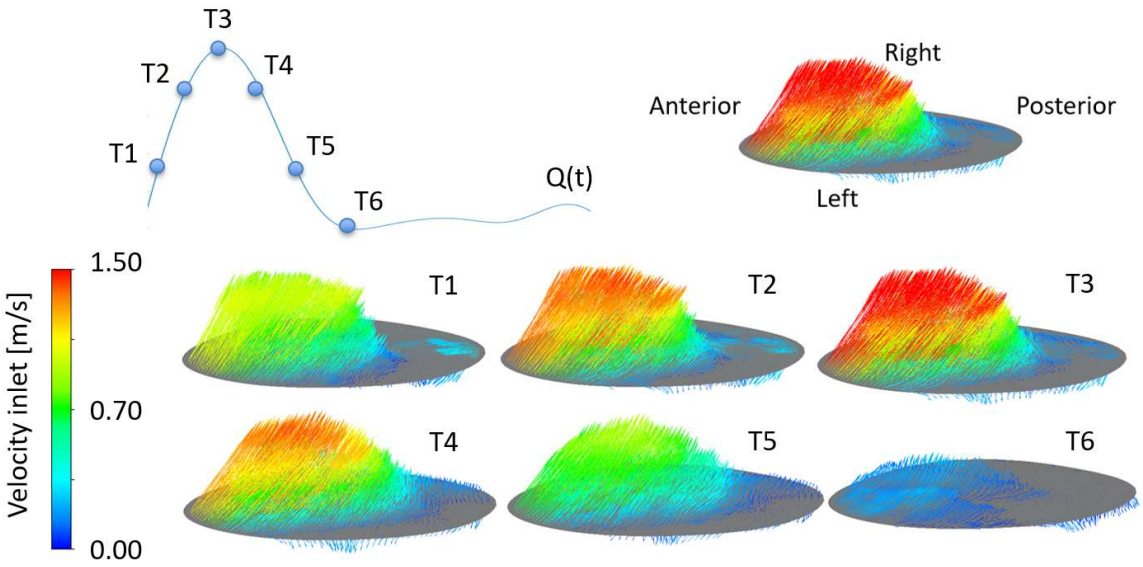

Figure 4. Inlet velocity profile at different time instant during the cardiac cycle. Figure highlight the skewness of the profile; higher velocities are located at the extrados of the ascending aorta, on the anterior side.

Outlet	*Z*	*C*	*R*
BCA	5.39×10^{7}	2.14×10^{-9}	7.62×10^{8}
LCCA	1.35×10^{8}	1.00×10^{-9}	1.61×10^{9}
LSA	5.68×10^{7}	1.14×10^{-9}	1.47×10^{9}
DAO	1.08×10^{7}	1.00×10^{-8}	1.64×10^{8}

Outlet	*Z*	*C*	*R*
BCA	3.33×10^{7}	3.23×10^{-9}	5.08×10^{8}
LCCA	1.14×10^{8}	1.51×10^{-9}	1.05×10^{9}
LSA	5.29×10^{7}	1.72×10^{-9}	9.63×10^{8}
DAO	1.04×10^{7}	1.51×10^{-8}	1.06×10^{8}

Table I. Used values of the *RCR* Windkessel model for the pre (left) and post-operation (right) model. ***Z*** = proximal resistance, ***C*** = compliance, ***R*** = peripheral resistance. Values are given in S.I. units, Pa·s/m^3 for resistances and m^3/Pa for compliances.

Numerical solution

FSI analysis was run in ANSYS v.17.2 (ANSYS Inc., Canonsburg, PA, USA) with a time step $\Delta t = 0.001$ s, coupling the structural solver – ANSYS Mechanical – and the fluid solver – ANSYS Fluent – using the embedded System Coupling module. ALE kinematic description was exploited. Simulations of two cardiac cycle took an average of 10 days running on 24 cores on a cluster server.

The structural solver solved the governing equation (**Equation 1**) of the finite element problem in the displacement-based approach using Newton-Raphson scheme.

$$\mathbf{M}\,\ddot{\bar{u}} + \mathscr{C}\,\dot{\bar{u}} + \mathbf{K}\,\bar{u} = \bar{\mathbf{f}}, \qquad \text{with } \mathscr{C} = 5650 \cdot \mathbf{M} + 0.1 \cdot \mathbf{K} \tag{1}$$

Where **M**, $\mathscr{C}$ and **K** are respectively the mass, viscous and stiffness matrix, $\bar{\mathbf{f}}$ is the load vector and $\bar{\ddot{\boldsymbol{u}}}$, $\bar{\dot{\boldsymbol{u}}}$ and $\bar{\boldsymbol{u}}$ are the nodal acceleration, velocity and displacement respectively. Viscous matrix was defined through a Rayleigh damping [28].

The fluid solver used the *Pressure-Implicit with Splitting of Operators* (PISO) algorithm to solve the Navier-Stokes and continuity equations (**Equation 2**) in the ALE configuration.

$$\begin{cases} \rho\left(\frac{\partial \mathbf{v}}{\partial t} + \left(\left(\mathbf{v} - \mathbf{v}_{\mathrm{g}}\right) \cdot \nabla\right)\mathbf{v}\right) = -\nabla p + \mu \nabla^2 \mathbf{v} \\ \nabla \cdot \mathbf{v} = 0 \end{cases} \tag{2}$$

Where ρ is the fluid density, $\mathbf{v}$ the velocity, $\mathbf{v}_{\mathrm{g}}$ the velocity of the mesh, p the pressure and μ the dynamic viscosity.

CFD simulations

In parallel with FSI, a CFD simulation with the same boundary conditions was performed to compare results. Furthermore, a sensitivity analysis of the inlet boundary conditions was performed for the presurgical model, testing three different inflow: a flat velocity profile, a parabolic velocity profile and the patient specific velocity profile.

Postprocessing

WSS were compared between the pre and post-intention model at systolic peak, when they reach their maximum. WSS plays a fundamental role in the triggering of the atherogenic process, especially when changes in direction and modulus [5,6]. Thus, the oscillatory shear index (OSI) was computed. The average shear stress experienced by the wall tissue was expressed through the time average wall shear stress (TAWSS). Velocities were visualized as streamlines and contours on section planes, to compare results from numerical simulations and 4D flow analysis. Pressure was exported at the inlet and compared with clinically measured systolic and diastolic pressures. The maximum principal stress, the maximum principal strain and displacement distribution of the wall were qualitatively compared with contour plots.

Results

Sensitivity to inlet boundary condition.

The comparison of the streamlines in the ascending aorta showed a very different patter with the flat and parabolic profile, while a good agreement was observed with the patient specific velocity

profile: that's the only boundary condition that allows to capture the skewness of the profile and vortical structure formations in a correct velocity range (**Figure 5**).

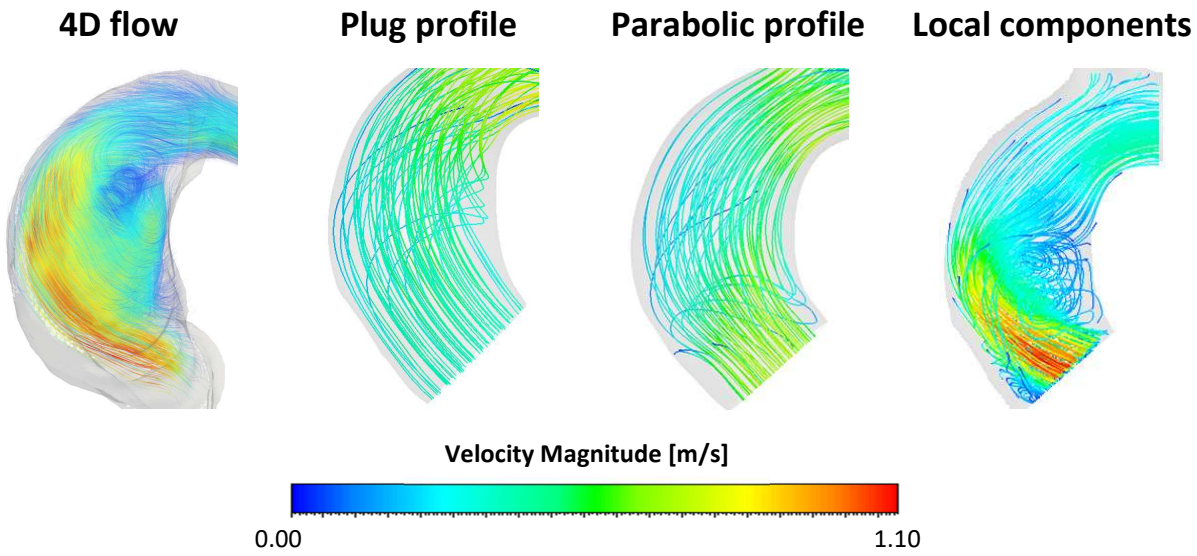

Figure 5. Streamlines at systolic peak obtained with 4D flow and 3 simulations with different boundary condition. Only the local velocity components profile was able to properly capture the hemodynamic in the ascending aorta.

Sensitivity to solution method: FSI v. CFD

The comparison between 4D flow, FSI and CFD velocity population was performed on six cross sectional planes (3 in ascending aorta, 3 in descending aorta) with an ANOVA. Both for the presurgical and postsurgical model, no significant difference was obtained (p>0.05) between FSI and 4D flow velocities, while a marked difference was observed in the descending aorta between CFD and 4D flow, both in the pre and postsurgical model. Difference was more marked in the pre-intervention configuration (**Figure 6**).

Streamlines were compared at systolic peak between the two FSI models and 4D flow analysis. A good agreement was found in the presurgical case, with correct inflow skewness and angle and vortical structures formation in the intrados of the ascending aorta. Streamlines pattern matched in the postsurgical case too, which showed a sustained flow with no recirculation.

Furthermore, a qualitative comparison was achieved between the velocity contours on cross sectional planes of the aorta. A good agreement of the contour pattern was generally observed, with significantly higher velocity in the CFD model (**Figure 7**).

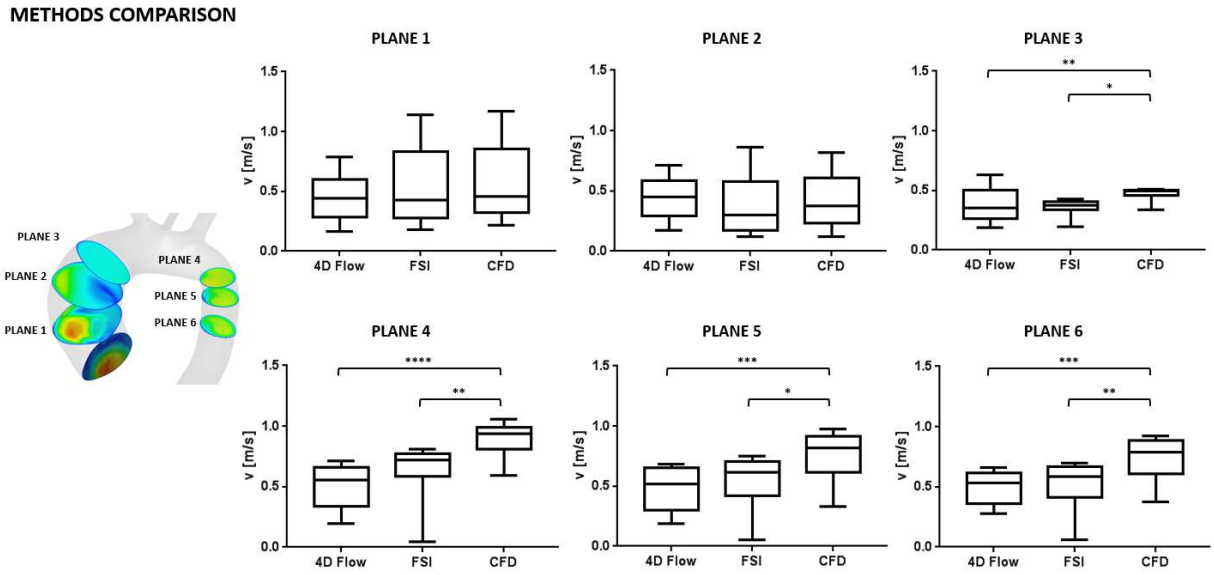

Figure 6. ANOVA of velocity distribution in presurgical model on 6 planes: 4D flow v. FSI v. CFD. Asterisks indicate the *p*-value: * = $p<0.05$, ** = $p<0.01$, *** = $p<0.001$ and **** = $p<0.0001$.

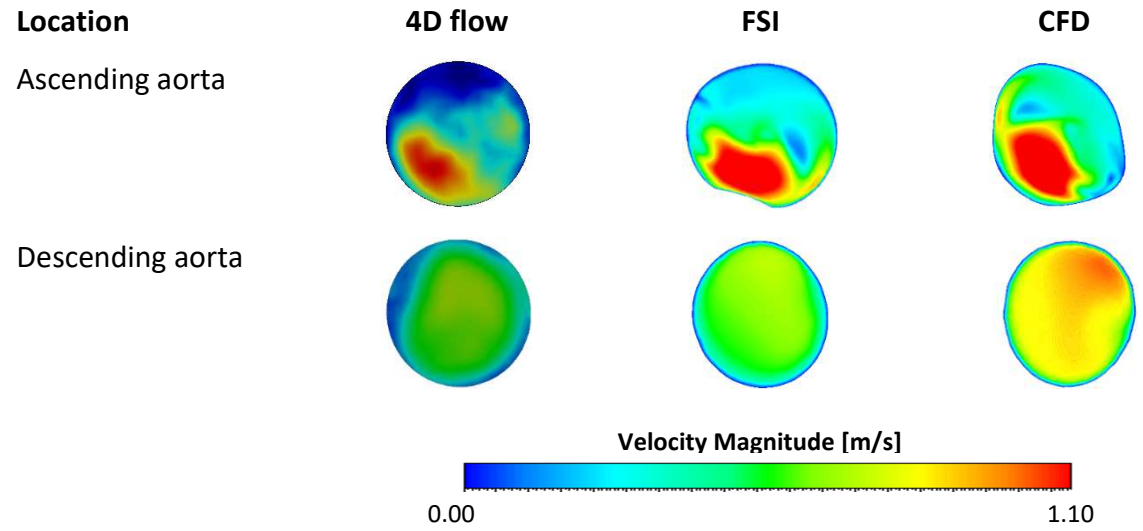

Figure 7. Velocity pattern on cross sectional plane in ascending and descending aorta for presurgical model.

Pre-intervention v. post-intervention

Systolic peak WSS reached a maximum value in descending aorta, in post-intervention model, greater by 28% than in pre-intervention model. OSI distribution assumed higher values in the presurgical model, with OSI close to 0.5 (critical threshold) in the ascending aorta and in the intrados of descending aorta. No significant difference was observed in TAWSS distribution (**Figure 8**). An *t*-test of WSS, OSI and TAWSS distribution in the descending aorta was performed.

Significantly higher WSS (p<0.001) and lower OSI (p<0.01) were found in the postsurgical case. No statistical difference was obtained for TAWSS (**Figure 9**).

The intramural stress was significantly altered in the postsurgical model: an intensification of stresses with values of ~500kPa was observed along the suture site, due to the compliance mismatch.

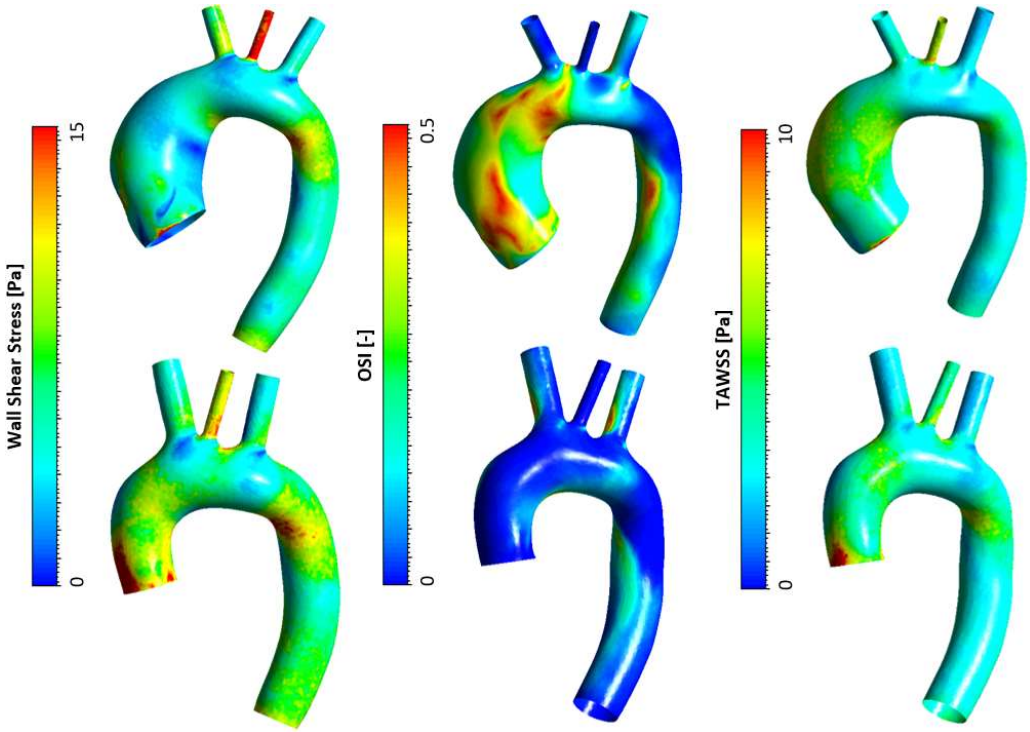

Figure 8. WSS, OSI and TAWSS distributions obtained from FSI analysis. Presurgical (top row) and postsurgical (bottom row) configurations.

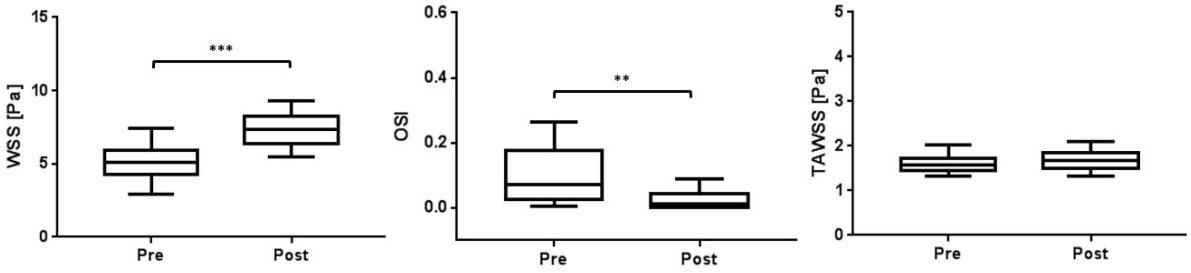

Figure 9. Results of *t*-test of WSS, OSI and TAWSS in the descending aorta obtained from FSI analysis. Asterisks indicate the *p*-value: * = p<0.05, ** = p<0.01, *** = p<0.001 and **** = p<0.0001.

Discussion

With this thesis work an innovative approach for the assessment of the hemodynamics in patients operated for aTAA with VSR technique was developed. FSI modeling combined with PC-MRI boundary conditions, was exploited for a reliable reproduction of patient's aortic biomechanics.

The comparison of FSI results with 4D flow provided a validation of the model and proved that CFD, even if well-conditioned, is an oversimplified approach. FSI analysis is necessary to properly replicate the aortic biomechanics.

The comparison of different inlet boundary conditions revealed that only the patient specific profile was able to properly capture the hemodynamics in the ascending aorta.

The comparison between the pre and postsurgical configurations showed results in agreement with previous studies [4] performed with 4D flow analysis: velocities and WSS significantly increase in the descending aorta after valve sparing surgery. High WSS in the descending tract represent a risk factor for the atherogenic process triggering, and consequently the formation of a TAA in descending aorta. The OSI distribution was characterized by significantly lower values in the postsurgical case, that assumed maximum value in the descending aorta intrados. Thus, after VSR surgery, descending aorta represent a risky region for TAA development.

The intensification of stress along the suture site is a significant aspect to be considered. The compliance mismatch due to the sharp change in stiffness between graft and native wall caused and significant increase in wall stress. Previous studies [8] suggested peak wall stress as a parameter to evaluate the aneurysm growing, thus an insight of this aspect would be recommended.

Conclusion

The developed FSI model provided a comprehensive insight into the biomechanics of a pathologic and a VSR treated aorta. The model was able to reproduce the operative condition of the vessel and permitted to investigate both fluid dynamics and structural aspects. The comparison between FSI and CFD approach demonstrated that, a simpler CFD provides unreliable results. Furthermore, we demonstrated that the ability to reproduce properly the aortic fluid dynamics doesn't depend on the boundary conditions only, but also on the type of modeling approach that is adopted.

The current work set the basis to a promising methodology for the optimization of surgical procedure for the treatment of aTAAs, since it is able to predict – for a specific patient – regions where the fluid dynamics results altered and consequently the atherogenic process will most likely take place. A further development for this study may consist in reproduce this modeling on a wider pool of patients and investigate the effect that different graft (e.g. different length, stiffness…) induce.

Bibliography

[1] "World Health Organization." [Online]. Available: https://www.who.int/health-topics/cardiovascular-diseases/#tab=tab_1.

[2] K. H. Chau and J. A. Elefteriades, "Natural history of thoracic aortic aneurysms: Size matters, plus moving beyond size," Prog. Cardiovasc. Dis., vol. 56, no. 1, pp. 74–80, 2013, doi: 10.1016/j.pcad.2013.05.007.

[3] R. De Paulis et al., "Long-term results of the valve reimplantation technique using a graft with sinuses," J. Thorac. Cardiovasc. Surg., vol. 151, no. 1, pp. 112–119, 2016, doi: 10.1016/j.jtcvs.2015.08.026.

[4] M. Gaudino, C. Lau, M. Munjal, D. Avgerinos, and L. N. Girardi, "Contemporary outcomes of surgery for aortic root aneurysms: A propensity-matched comparison of valve-sparing and composite valve graft replacement," J. Thorac. Cardiovasc. Surg., vol. 150, no. 5, pp. 1120-1129.e1, 2015, doi: 10.1016/j.jtcvs.2015.07.015.

[5] J. M. Zhang, L. P. Chua, D. N. Ghista, S. C. M. Yu, and Y. S. Tan, "Numerical investigation and identification of susceptible sites of atherosclerotic lesion formation in a complete coronary artery bypass model," Med. Biol. Eng. Comput., vol. 46, no. 7, pp. 689–699, 2008, doi: 10.1007/s11517-008-0320-4.

[6] D. N. Ku, D. P. Giddens, C. K. Zarins, and S. Glagov, "Pulsatile flow and atherosclerosis in the human carotid bifurcation. Positive correlation between plaque location and low and oscillating shear stress," Arteriosclerosis, vol. 5, no. 3, pp. 293–302, 1985, doi: 10.1161/01.atv.5.3.293.

[7] H. Meng, V. M. Tutino, J. Xiang, and A. Siddiqui, "High WSS or Low WSS? Complex interactions of hemodynamics with intracranial aneurysm initiation, growth, and rupture: Toward a unifying hypothesis," Am. J. Neuroradiol., vol. 35, no. 7, pp. 1254–1262, 2014, doi: 10.3174/ajnr.A3558.

[8] R. Campobasso, F. Condemi, M. Viallon, P. Croisille, S. Campisi, and S. Avril, "Evaluation of Peak Wall Stress in an Ascending Thoracic Aortic Aneurysm Using FSI Simulations: Effects of Aortic Stiffness and Peripheral Resistance," Cardiovasc. Eng.

[9] V. Mendez, M. Di Giuseppe, and S. Pasta, "Comparison of hemodynamic and structural indices of ascending thoracic aortic aneurysm as predicted by 2-way FSI, CFD rigid wall

simulation and patient-specific displacement-based FEA," Comput. Biol. Med., vol. 100, no. May, pp. 221–229, 2018, doi: 10.1016/j.compbiomed.2018.07.013.

[10] F. Cuomo, S. Roccabianca, D. Dillon-Murphy, N. Xiao, J. D. Humphrey, and C. A. Figueroa, "Effects of age-associated regional changes in human central artery mechanics on systemic hemodynamics revealed by computational modeling," PLoS One, vol. 12, no. 3, pp. 1–21, 2017, doi: 10.7302/Z24B2Z7Z.

[11] T. Khamdaeng and P. Terdtoon, "Regional pulse wave velocity and stress in aneurysmal arch-shaped aorta," Biomed. Mater. Eng., vol. 29, no. 4, pp. 527–549, 2018, doi: 10.3233/BME-181007.

[12] R. Jayendiran, B. Nour, and A. Ruimi, "Fluid-structure interaction (FSI) analysis of stent-graft for aortic endovascular aneurysm repair (EVAR): Material and structural considerations," J. Mech. Behav. Biomed. Mater., vol. 87, no. May, pp. 95–110, 2018, doi: 10.1016/j.jmbbm.2018.07.020.

[13] C. J. Drewe, L. P. Parker, L. J. Kelsey, P. E. Norman, J. T. Powell, and B. J. Doyle, "Haemodynamics and stresses in abdominal aortic aneurysms: A fluid-structure interaction study into the effect of proximal neck and iliac bifurcation angle," J. Biomech., vol. 60, pp. 150–156, 2017, doi: 10.1016/j.jbiomech.2017.06.029.

[14] N. Xiao, J. Alastruei, and C. A. Figueroa, "A systematic comparison between 1-D and 3-D hemodynamicsin compliant arterial models," Int. Journey Numer. methods Biomed. Eng., 2014.

[15] S. Lin, X. Han, Y. Bi, S. Ju, and L. Gu, "Fluid-structure interaction in abdominal aortic aneurysm: Effect of modeling techniques," Biomed Res. Int., vol. 2017, 2017, doi: 10.1155/2017/7023078.

[16] P. Reymond, P. Crosetto, S. Deparis, A. Quarteroni, and N. Stergiopulos, "Physiological simulation of blood flow in the aorta: Comparison of hemodynamic indices as predicted by 3-D FSI, 3-D rigid wall and 1-D models," Med. Eng. Phys., vol. 35, no. 6, pp. 784–791, 2013, doi: 10.1016/j.medengphy.2012.08.009.

[17] R. Savabi, M. Nabaei, S. Farajollahi, and N. Fatouraee, "Fluid structure interaction modeling of aortic arch and carotid bifurcation as the location of baroreceptors," Int. J. Mech. Sci., vol. 165, no. July 2019, 2020, doi: 10.1016/j.ijmecsci.2019.105222.

[18] S. Pirola et al., “On the choice of outlet boundary conditions for patient-specific analysis of aortic flow using computational fluid dynamics,” J. Biomech., vol. 60, pp. 15–21, 2017, doi: 10.1016/j.jbiomech.2017.06.005.

[19] C.-Y. Liu, D. Chen, D. A. Bluemke, and W. G. Hundley, “Evolution of aortic wall thickness and stiffness with atherosclerosis: Long-term follow up from the Multi-Ethnic Study of Atherosclerosis (MESA),” HHS Public Access, vol. 69, no. 1, pp. 110–120, 2015, doi: 10.1016/j.socscimed.2009.04.010.Are.

[20] W. Karel van den Hengel, “Abdominal aortic wall thickness and compliance The possibilities to measure and the effect of variation in the analysis of aneurysms,” Blood, no. April, 2008.

[21] J. D. Cutnell and K. W. Johnson, Physics (4th Edition, Volume 1). 1997.

[22] L. Dintenfass, Blood Viscosity, Hyperviscosity & Hyperviscosaemia. Springer Science & Business Media, 1985.

[23] T. Khamdaeng, J. Luo, J. Vappou, P. Terdtoon, and E. E. Konofagou, “Arterial stiffness identification of the human carotid artery using the stress – strain relationship in vivo,” Ultrasonics, vol. 52, no. 3, pp. 402–411, 2012, doi: 10.1016/j.ultras.2011.09.006.

[24] G. Tasca et al., “Aortic Root Biomechanics After Sleeve and David Sparing Techniques: A Finite Element Analysis,” Ann. Thorac. Surg., vol. 103, no. 5, pp. 1451–1459, 2017, doi: 10.1016/j.athoracsur.2016.08.003.

[25] J. F. Ladisa et al., “Computational simulations for aortic coarctation: Representative results from a sampling of patients,” J. Biomech. Eng., vol. 133, no. 9, 2011, doi: 10.1115/1.4004996.

[26] A. S. Les et al., “Quantification of hemodynamics in abdominal aortic aneurysms during rest and exercise using magnetic resonance imaging and computational fluid dynamics,” Ann. Biomed. Eng., vol. 38, no. 4, pp. 1288–1313, 2010, doi: 10.1007/s10439-010-9949-x.

[27] P. Reymond, F. Merenda, F. Perren, D. Rüfenacht, and N. Stergiopulos, “Validation of a one-dimensional model of the systemic arterial tree,” Am. J. Physiol. - Hear. Circ. Physiol., vol. 297, no. 1, pp. 208–222, 2009, doi: 10.1152/ajpheart.00037.2009.

[28] T. E. Tezduyar, S. Sathe, T. Cragin, B. Nanna, and M. Schwaa, “Modelling of fluid–structure interactions with the space–time finite elements: Arterial fluid mechanics,” Int. J. Numer. Methods Fluids, vol. 54, no. October 2010, pp. 901–922, 2007, doi: 10.1002/fld.

Chapter 1
Introduction

Chapter summary

In this chapter an overview on the anatomy, physiology and pathologies of the aorta will be given. Attention will focus on aneurysm of the ascending thoracic aorta (aTAA), and the surgical procedures performed for the reconstruction of the aortic root. In the last section, an insight into phase contrast magnetic resonance imaging (PC-MRI) and its potentialities and limitations for the measurement of hemodynamic quantities will be provided.

1.1 Anatomy and physiology

Cardiovascular system is an organs system that carries oxygen, nutrients and hormones within human body, as well as waste products (e.g. carbon dioxide) that get removed later. It is composed by three main elements: the heart, blood and the vessels [1]. A brief description of these components is provided below.

1.1.1 The heart

The heart consists of four chambers: two atria and two ventricles, separated by the interventricular septum (**Figure 1.1**). Atria receive blood from the body – the right one from systemic circulation through vena cava, the left one from pulmonary circulation through pulmonary vein – while ventricles pump blood towards the body – the right one to lungs through pulmonary artery, the left one to systemic circulation through the aorta – in order to guarantee flow unidirectionality. Atria and ventricles are separated by the tricuspid and mitral valve, pulmonary and aortic valve separate the ventricles from pulmonary artery and aorta respectively. Valves open and close passively due pressure difference upstream and downstream the valve itself. This four valves system permits to maintain a one-way flow of blood in the heart [1].

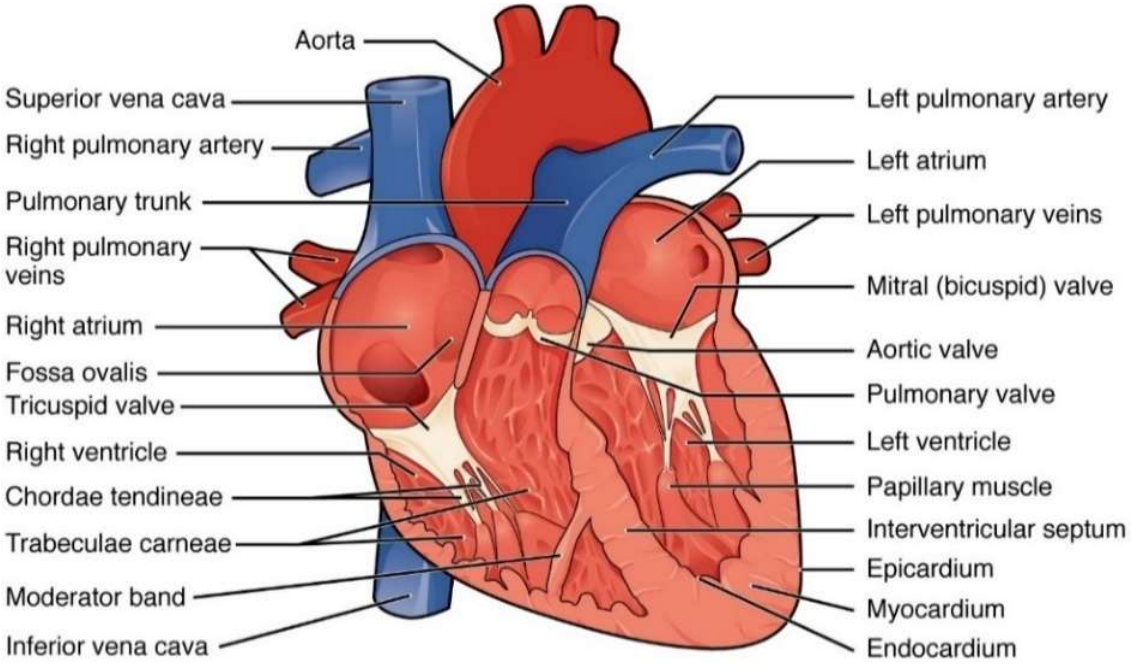

Figure 1.1. Anterior view of the heart showing the four chambers, the major vessels and their early branches, as well as the four valves [2].

Heart serves as a pulsatile pump for blood, in a lifespan it can push into circulation up to 200 million liter [3]. A cardiac cycle (**Figure 1.2**) is divided in two phases: systole and diastole. Systole is generally identified as the time interval between the mitral valve closure instant and the end of ejection, diastole is the retainer [1]. One cycle consists in the following sequence of events:

- *Ventricular filling*: after the tricuspid and mitral valve open at the beginning of diastole the ventricles start to fill. The process is enhanced by the elastic recoil from systolic configuration.
- *Atrial systole*: once the ventricles are filled, the atria contract causing a reverse pressure gradient across the mitral and tricuspid valve, that close.
- *Blood ejection*: an electric stimulus initiates the ventricular contraction, that causes a sharp increase in blood pressure. When pressure exceeds the afterload, the pulmonary and aortic valve open and the cardiac output is ejected. When the ejected blood starts to decelerate, pressure decreases leading to the closure of the pulmonary and aortic valve.

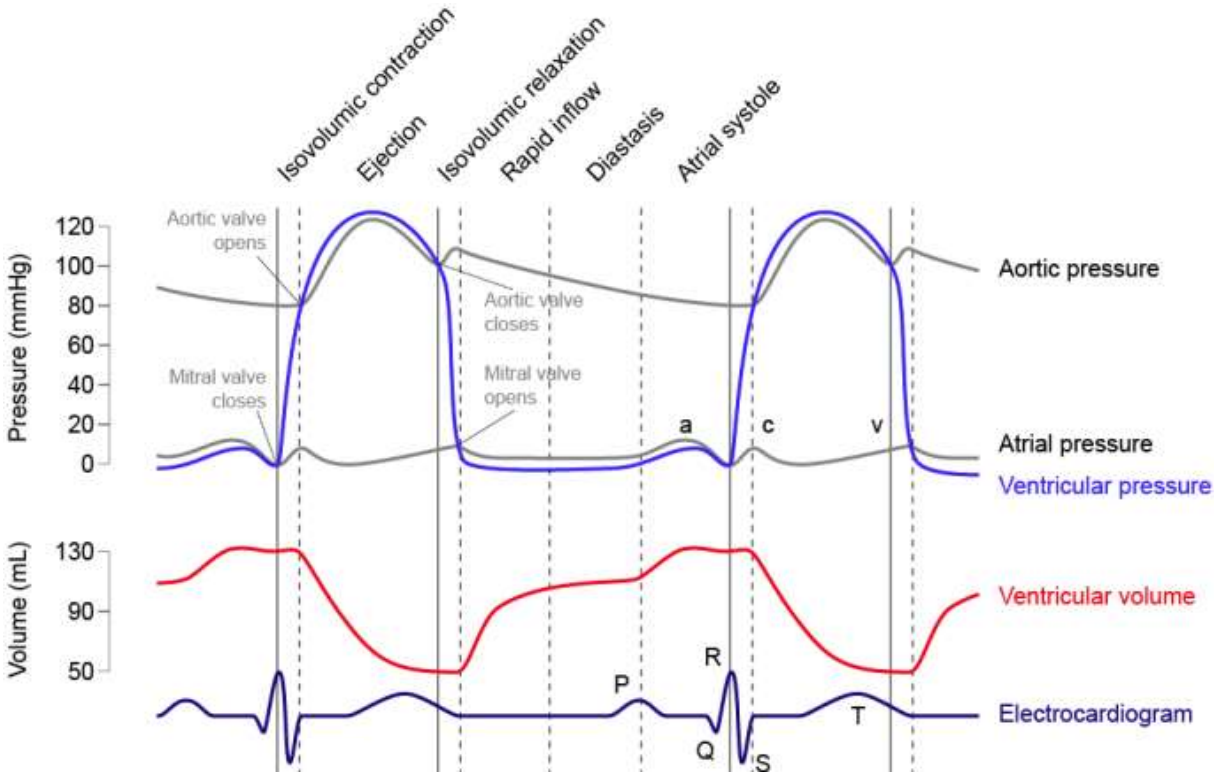

Figure 1.2. From the top: pressure waveforms of the left atrium and ventricle (mmHg); variation of the left ventricle volume (mL); electrocardiogram (ECG).

1.1.2 The blood

Blood is one of human body connective tissue. It consists of specialized cells that reside in a liquid extracellular matrix, the plasma. The corpuscular part of blood is called hematocrit and it's a suspension of mainly red blood cells (RBCs), white blood cells (WBCs) and platelets (~45% of blood volume). The plasma is a liquid (~55% of blood volume) that consist of water, metabolites and ions. RBCs are made up of a compound called hemoglobin, a protein that binds to oxygen and carry it through the body, WBCs protect body against infection and platelets are involved in the clotting process (i.e. blood coagulation) [4].

1.1.3 The vessels

Blood flows through human body within blood vessels. The circulation (**Figure 1.3**) is divided in two sub-system: the pulmonary and the systemic circulation. Pulmonary circulation carries blood through lungs and toward the left atrium, systemic circulation carries blood through the rest of organs and towards the right atrium.

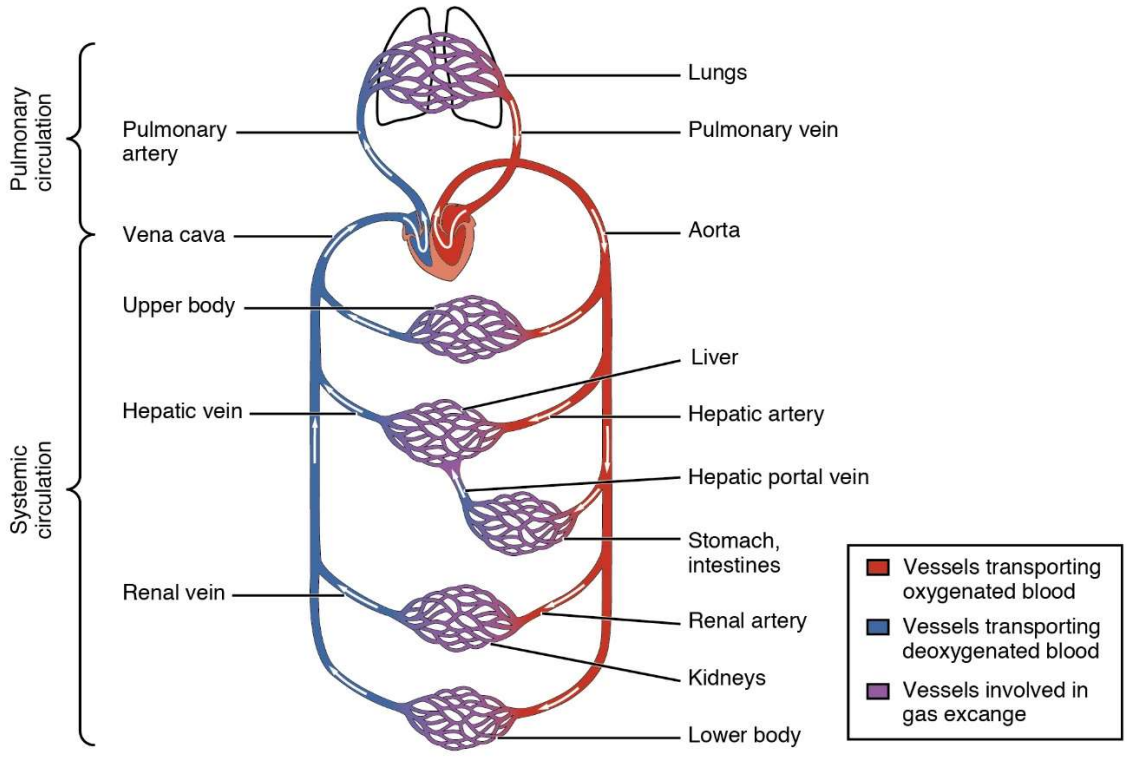

Figure 1.3. Pulmonary circuit moves blood from the right heart to the lungs and back to the left heart. Systemic circuit moves blood from the left heart through the whole body and back to the right heart. Arrows indicates the directionality of the flow [2].

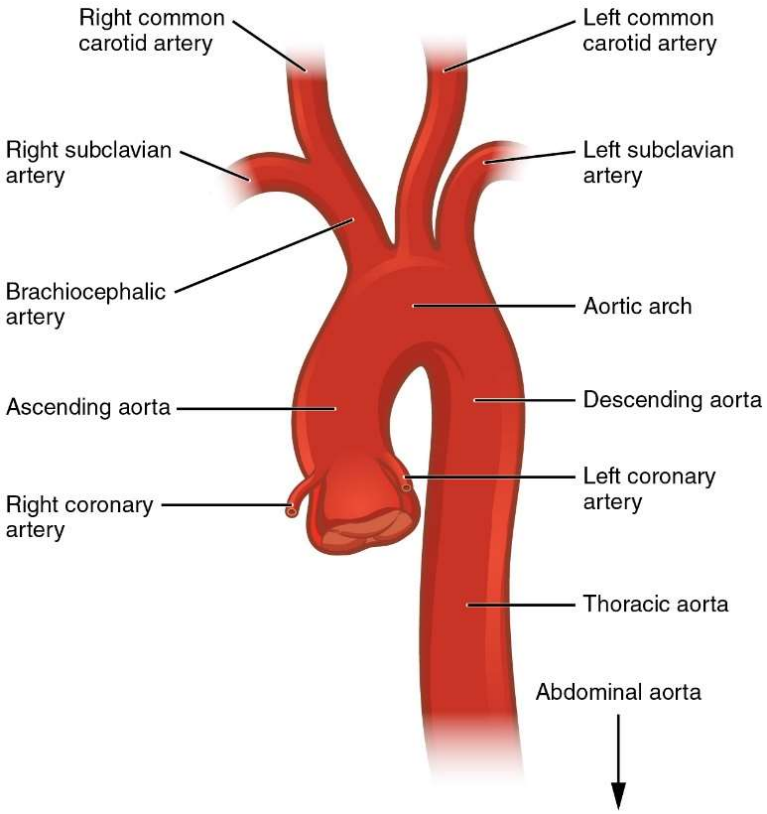

Figure 1.4. Anatomy of the thoracic and proximal abdominal aorta [2].

Vessels are classified in arteries, which carry oxygenated blood, capillaries, very small arterial branches where mass exchange process between organs and blood actually takes place, and veins, that carry deoxygenated blood back to the right atrium [1].

The aorta (**Figure 1.4**) is the main artery of the systemic circulation and the largest artery of the whole circulatory system. It originates from the left ventricle outflow tract (LVOT) and consists of different sectors: the aortic root (or sinuses of Valsava), the ascending thoracic aorta, the aortic arch – from which arteries perfusing the upper-body arise – the descending thoracic aorta and the abdominal tract, from which the celiac truck arises and perfuses visceral organs. The aorta ends with the aorto-iliac junction at the level of the lumbar vertebra L4, where it splits into the two iliac arteries, that perfuse legs. Aortic inner diameter reduces from the root to the iliac junction, with an average value of 25 mm [1] [5].

All of the arteries that form the systemic circulation arise from the aorta or from one of the aortic branches. The first main branches are the two coronary arteries, these originate from the sinuses of Valsalva and perfuses the heart during the diastolic phase.

From the aortic arch three branches arise (**Figure 1.4**) that perfuse the upper part of the body:

- Brachiocephalic trunk (BCA), that gives rise in turn to the right subclavian (RSA) and right common carotid artery (RCCA). Those perfuse the right arm and the right part of the neck respectively.
- Left common carotid artery (LCCA), that perfuses the left part of the neck.
- Left subclavian artery (LSA), that perfuses the left arm.

Variations in the aortic arch and its branches are not rare. Rarely, the left common carotid artery may originate from the right-sided brachiocephalic artery rather than the aortic arch. In other individuals, the left common carotid and the brachiocephalic artery may have a common origin. In even rare cases, the brachiocephalic artery may give rise to all 3 branches [6].

1.2 Histology of blood vessels

Arteries are elastic multilayer structures with compliant features. The microstructure of the arterial wall varies with the location along the vascular tree and consequently their compliant capability, but regardless of its location, all arteries consist of three layers: *tunica intima*, *tunica media* and *tunica adventitia* (**Figure 1.5**) [1].

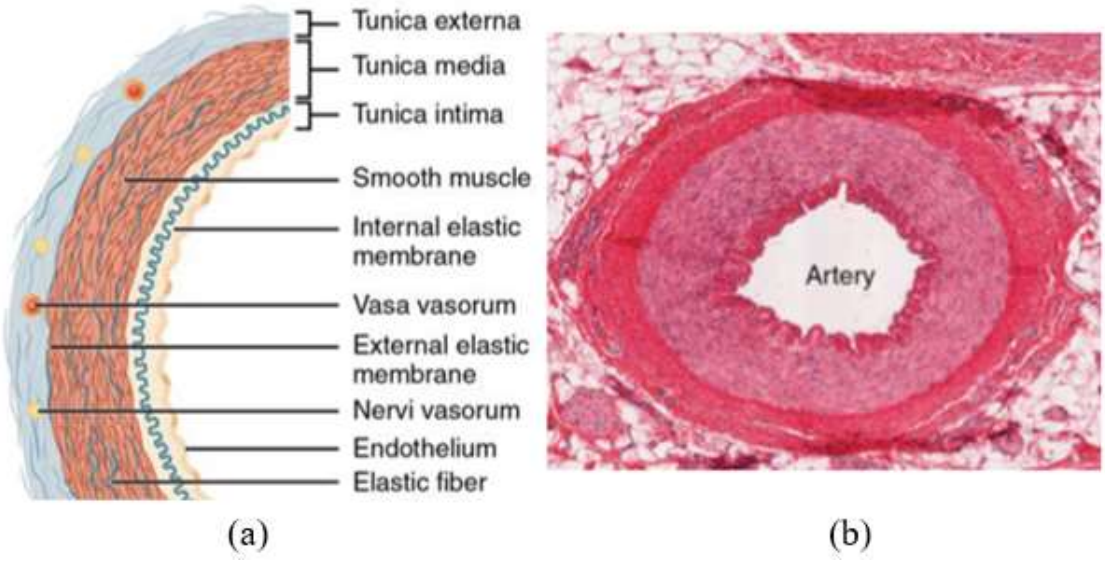

Figure 1.5. Schematic representation of the layer structure of the aortic wall (a) and histology (b) showing the relative difference in thickness in a healthy subject [2].

The intima consists of a monolayer of endothelial cells (ECs) and basal lamina of type IV collagen (as all the arteries) with an additional layer of connective tissue and smooth muscle

cells (SMCs). The tunica intima provides structural support to the arterial wall and is separated from media by an elastic lamina. The media contains SMCs embedded in an extracellular matrix of elastin and collagen (type I, III and V) and proteoglycans. The collagen fiber orientation of the medial constituents is such that they promote vessel contraction. In the aorta, SMCs are organized in 40 to 70 concentric layers, separated by a thin fenestrated sheet of elastin, those form a structural and functional unit called musculo-elastic fascicle. The number of layers increases with the diameter of the aorta, making the arterial wall thicker for larger diameters, a general rule is that the thickness increases of 0.05 mm for every 1 mm increase in the diameter. The adventitia is a dense network of type I collagen fibers, that contains nerves, fibroblasts and vasa vasorum. It comprises only 10% of the arterial wall in elastic arteries and primarily serves as a protective sheath, in many vessels the adventitia is contiguous with perivascular tissue, which provides additional structural support [1].

1.3 Physiology of the aorta

The aorta plays a crucial role in blood circulation, as systemic circulation starts form it. Through vasomotion, that is the spontaneous contraction of the arterial wall, the aorta provides support to the pumping action of the heart and increase blood flow rate towards the body. Being the most proximal artery to the heart, it also acts as a compliance that dampens the pulsatile flow, received from the heart, in nearly steady flow in peripheral vessels. The elasticity of the wall allows the vessel to expand and accommodate a fraction of the stroke volume (SV), working as a reservoir. During systole, the reservoir expands and receive blood, during diastole it discharges blood through the systemic circulation, thanks to the elastic recoil. This mechanic action causes the smoothing of the flow rate waveform that combined to the effect due to progressive stiffening of the arterial wall in peripheral vessels, makes the flow almost steady [7].

In the wall of the aortic arch baroreceptors are located, when the aortic wall is stretched, receptors produce a signal, that is sent through the *vagus nerve* to the nucleus of the solitary tract in the brainstem. This latter can activate and inactivate the sympathetic and parasympathetic system, helping to prevent rapid variations in blood pressure. This mechanism helps to accomplish blood pressure homeostasis [6].

Another role that the aorta accomplishes is monitoring blood composition. Peripheral chemoreceptors control the partial pressure of carbon monoxide and oxygen in blood. When their amount changes, a signal is sent via the *vagus nerve* to the dorsal respiratory group, which responds regulating breathing [6].

1.4 Pathologies of the aorta

Cardiovascular diseases (CVDs) represent the leading cause of death in the Western World, taking approximately 17.1 million lives each year (31% of all deaths worldwide). One third of deaths occur prematurely in people under 70 years of age [8] [9]. CVDs include heart disorders, coronary heart disease, rheumatic fever, blood vessels disorders and other conditions [8].
Main pathologies that involve the aorta are herein described.

1.4.1 Aortic coarctation (CoA)

Aortic coarctation is a congenital disease with an incidence of 4/10000 live births [10] that causes the focal narrowing of the aortic segment (**Figure 1.6**), generally near the *ligamentum arteriosum*. The ligamentum arteriosum is a small ligament that is remnant of the *ductus Botalli*, a vessel that connects the aorta and the pulmonary vein in the fetus and that close at birth. When the ductus fails to close at birth, it results in a condition called *patent ductus arteriosum* (PDA), that increase the risk to develop a CoA. Generally, the stenotic area is focused at the level of the aortic isthmus (the connection point between the arch and the descending aorta), but its extent may involve part of the arch as well. CoA is generally diagnosticated in infancy, when untreated main complications involve hypertension and aortic dissection [11].

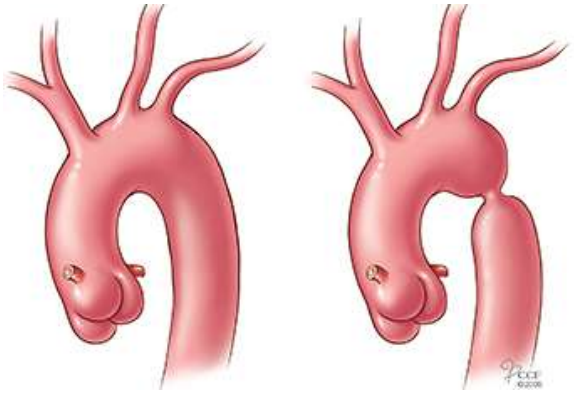

Figure 1.6. Healthy aorta on the left and coarcted aorta on the right. Stenotic area is generally located in the descending tract.

1.4.2 Aortic dissection (AD)

Aortic dissections occur generally after the lesion of the innermost layer of the aorta, the *tunica intima*, that causes its separation from the other two layers. This separation allows blood to flow into the media layer creating a *false lumen* (**Figure 1.7**). The main risk associated to AD is the rupture of the aorta, due to the pressurized *false lumen* compressing the *true lumen* [5]. AD is a relatively rare event, that occurs in 3/100000 patients per year [12].

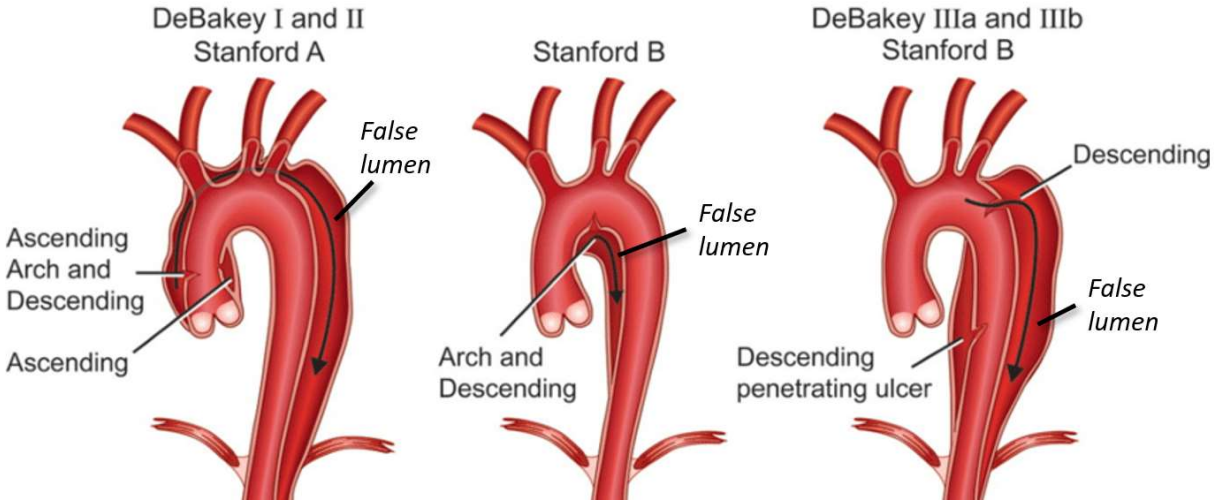

Figure 1.7. Stanford and DeBakey classification of aortic dissection. Aortic dissection is classified based on the anatomy of the problem: type A involves the whole aorta, starting from the ascending tract, type B begins beyond the left subclavian artery.

1.4.3 Atherosclerosis

Atherosclerosis is due to a focal accumulation of lipids, calcium and necrotic debris within the intimal layer. This causes a narrowing of the lumen (i.e. stenosis), that compromise blood flow. The main complications is the rupture of the plaque, which can coagulate, causing the complete occlusion of the vessel and leading to myocardial infarction or stroke [1]. Other disorders associated with aortic atherosclerosis are coronary artery disease, carotid artery disease and aneurysms. Atherosclerosis of the aorta is a relatively common disorder, affecting ~7% of population, but it is most of the time asymptomatic. Only in less than 1% of cases it leads to other complication in the patient [13].

Aortic atherosclerotic is strictly related with thoracic aortic aneurysm: severe aortic plaque (thicker than 5 mm) is found in ~52% of patients with aneurysm.

1.4.4 Thoracic aortic aneurysm (TAA)

Thoracic aortic aneurysm (TAA) is a focal dilatation of the vessel, caused by a local weakening of the arterial wall. The vessel grows silently in most cases and can end up into a rupture of the wall, with catastrophic consequence for the subject [1]. Depending on their location along the aortic lumen, TAAs are classified in aortic root aneurysm, ascending aorta aneurysm (aTAA), aortic arch aneurysm and descending aortic aneurysm (dTAA) as **Figure 1.8** shows. In the United States of America (that is a good world-representative sample) TAAs have an incidence of ~1/10000 persons [9]. Mortality is remarkable, indeed TAA results in approximatively 152000 deaths per year worldwide [14].

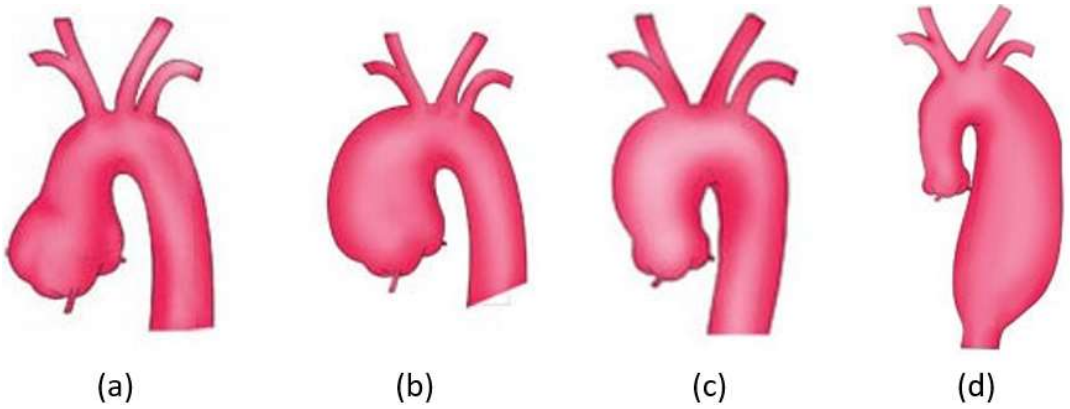

Figure 1.8. Classification of thoracic aortic aneurysm. From left to right: aortic root aneurysm (a), ascending aorta aneurysm (b), aortic arch aneurysm (c) and descending aorta aneurysm (d).

TAA is a lethal disease that in 95% of cases its diameter grows asymptomatically, with a rate of 1 mm per year, until the occurrence of an acute event [9]. According to clinical practice, the size of an aneurysm is the most important parameter to be considered in the follow up of the patient, since it has been showed that the risk of natural complications increases as the TAA gets larger. Hence, patients are chosen for elective surgery, basing on the size of the aneurysm [9].

In most cases the developing of an aTAA is due to cystic medial degeneration (MD), which consist in the loss and disorganization of SMCs and elastic fibers, laminar medial collapse and fibrosis (**Figure 1.9**). MD is naturally due to aging, but it can also be induced by other pathologies such as hypertension, bicuspid aortic valve (BAV) and Marfan syndrome (MFS) [3].

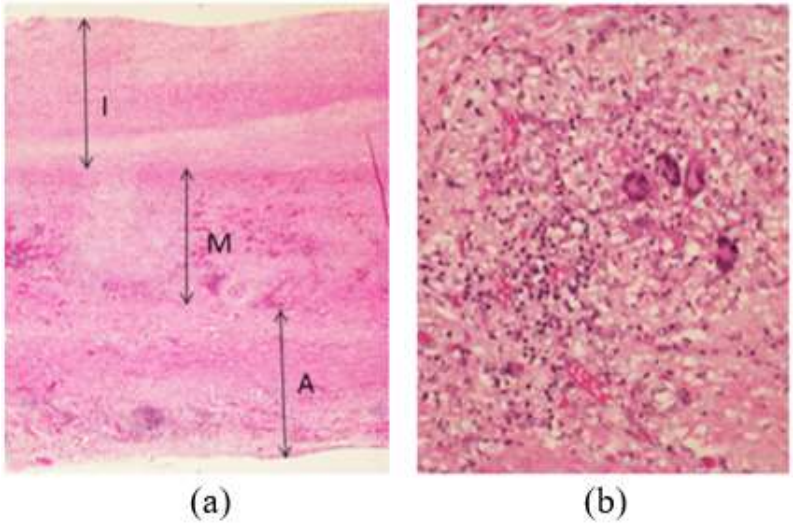

Figure 1.9. (a) Low-power view of the thoracic aorta showing marked thickening of the adventitia (A) and moderate intimal (I) thickening. The media (M) shows focal destruction and inflammation (H&E stain). (b) High-power view demonstrating destruction of the media and marked inflammation consisting of lymphocytes, macrophages, and giant cells (H&E stain) [3].

BAV is a congenital heart disorder in which two of the three leaflets of the aortic valve fuse, resulting in a bicuspid valve [15]. This results in the alteration of the hemodynamics in the ascending aorta, in terms of blood flow velocity and flow angle. Fusion pattern varies in each patient [16]. Although TAAs occur both in tricuspid aortic valves and BAVs, it has been estimated that 50-70% of BAV patients develop aortic dilation and ~40% of BAV patients develop TAAs [17].

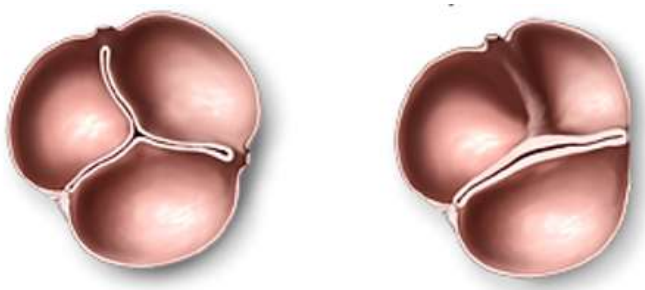

Figure 1.10. A healthy tricuspid aortic valve (left) and a bicuspid aortic valve (right).

MFS is a congenital disorder of the connective tissue, due to a genetic mutation in fibrillin-1 (FBN1), the gene that produce fibrillin. Fibrillin is a glycoprotein that form the extracellular matrix of elastic fiber, the anomaly in its codification results in a weakening of the arterial wall

[3]. This weakening makes the aorta easier to dilate and promotes the formation of TAA especially aortic root aneurysms, that eventually occurs in 60-80% of cases [18].

1.5 Overview of corrective procedures

In this section an overview of the surgical procedures, as well as the criteria used to decided when subjecting a patient to elective surgery and its long-term effects, will be given.

1.5.1 Criteria for elective surgery

The monitoring and managing of TAA is based on clinical experience. There is no absolute indicator to know when an aneurysm would rupture, but it has been observed that a "hinge point" exists for the diameter. When TAAs grow more than the critical size, the risk of acute complications increases significantly from <10% to >40% [9] as shown in **Figure 1.11**. Thus, the diameter of the aneurysm is the main parameter that is considered to decide whether to proceed with elective surgery or not. For aTAA the hinge point is 60 mm, while for dTAA is 70 mm.

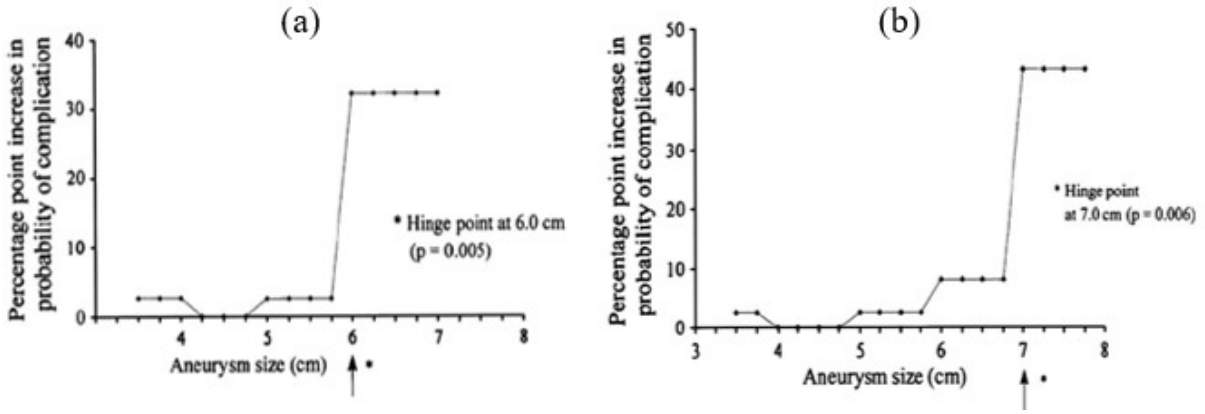

Figure 1.11. Effects of aortic size aneurysm on cumulative, lifetime incidence of complications for (a) ascending aorta and (b) descending aorta [9].

Regardless of the size, all symptomatic aneurysm should be treated. Symptoms include pain in the aneurysm region, unexplained by other causes, and congestive symptoms (especially in aTAA patients) [9].

Elective surgery of TAAs is a very safe and beneficial procedure to the patient, the 5-years survival rate after the treatment is >85%, while emergency surgery (very dangerous) has a 5-

year survival rate of 37%. Recommendations for surgical intervention, based on the aneurysm size are summarized in **Table 1.1** [9].

	Non-MFS	**MFS**	**BAV**
Ascending aorta	5.5 cm	5.0 cm	5.0 cm
Descending aorta	6.5 cm	6.0 cm	N/A*

Table 1.1. Size criteria for elective surgical intervention of TAA. MFS: Marfan Syndrome, BAV: Bicuspid Aortic Valve. *BAV increases the risk of rupture of aTAA but not of descending TAA.

The "dimensional criterion" is the gold standard for deciding if a patient should be subjected to elective surgery but is not the only one: when aneurysmal growth rate exceeds 1 cm/year intervention is recommended [9].

However, the choice to intervene is totally arbitrary and depends on the physician and severe complications may occur in a patient before the reaching of the hinge point statistically determined. 31% and 43% of patients affected by aTAA and dTAA respectively, already suffer from an acute event before reaching the aneurysm critical size [9].

Hence, elective surgical treatment must be performed before the aorta grows to its hinge point but a strong criterion to discriminate patients to be operated and not is still unavailable.

1.5.2 Surgical procedure

In the last decades, the number of surgerical operation due to aTAA has constantly increased, consistently with the growing of cardiovascular diseases incidence in the Western world. Temporal trend is shown in **Figure 1.12** [19].

Surgical procedure for the treatment of aTAA consists in composite graft replacement of the ascending aorta and aortic valve. Generally, an aTAA leads to the progressive dilatation of the aortic sinuses and the consequent dilatation and distortion of the aortic anulus, eventually leading to aortic valve distortion and insufficiency. However, many patients with aTAA requiring surgery, still have normal aortic valve leaflets, so it is possible to preserve the native aortic valve by re-implanting it in a straight tubular polyethylene teraphtelathe (PET) graft or in a PET prosthesis with Valsava neo-sinuses [20] [21].

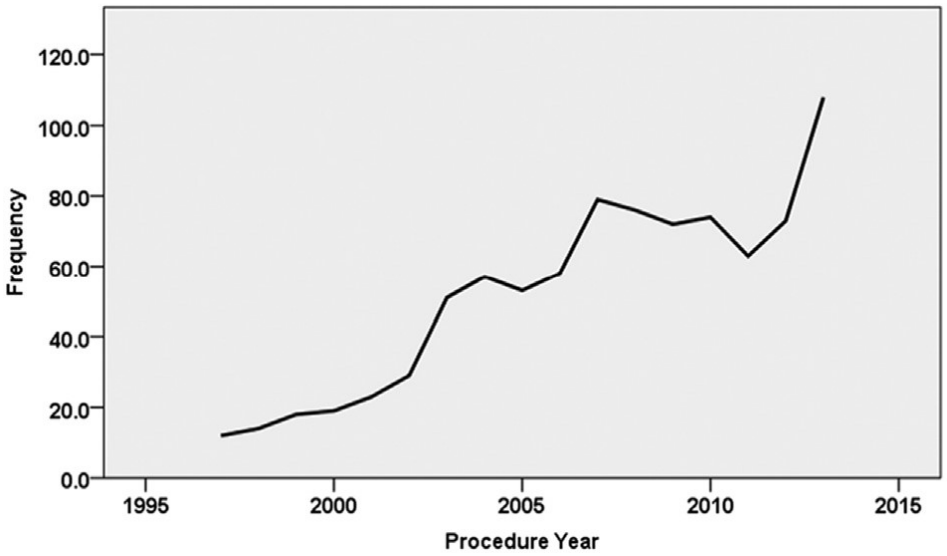

Figure 1.12. Frequency of aortic root procedure by year (1997-2013), basing on a pool of patients treated at New York Presbyterian Hospital.

Surgery is performed using median sternotomy, central aortic cannulation, hypothermic cardiopulmonary bypass, aortic cross-clamping and myocardial protection with cold antegrade blood cardioplegia. Routinely, ε-aminocaproic acid is used as an antifibrinolytic agent [19].
Three different options are available for aortic root replacement:

- *Mechanical composite valved graft (mCVG) replacement*. This type of prosthesis is implanted when the native aortic valve is severely compromised. A mechanical valve is sewn inside a PET vascular prosthesis 3 to 5 mm larger than the valve, using a continuous 3-0 polypropylene suture, then the composite is implanted in the patient with Bentall procedure (**Figure 1.13.b**). The mCVG replacement is performed in 32.5% of cases [19].
- *Biologic composite valved graft (bCVG) replacement*. The procedure is analogue to the mCVG but for the valve, that is biologic. Using a biologic prosthesis allows patients in need of complete root replacement the option of a composite valved graft without the need for anticoagulation. The bCVG replacement is performed in 47.3% of cases [19].
- *Valve-sparing reconstruction (VSR)*. This procedure is performed when the aortic valve is still healthy, with the advantage of retaining the native valve of the patient. VSR is generally performed using David-I method (**Figure 1.13.c**) and it's adopted in 20.2% of cases [19].

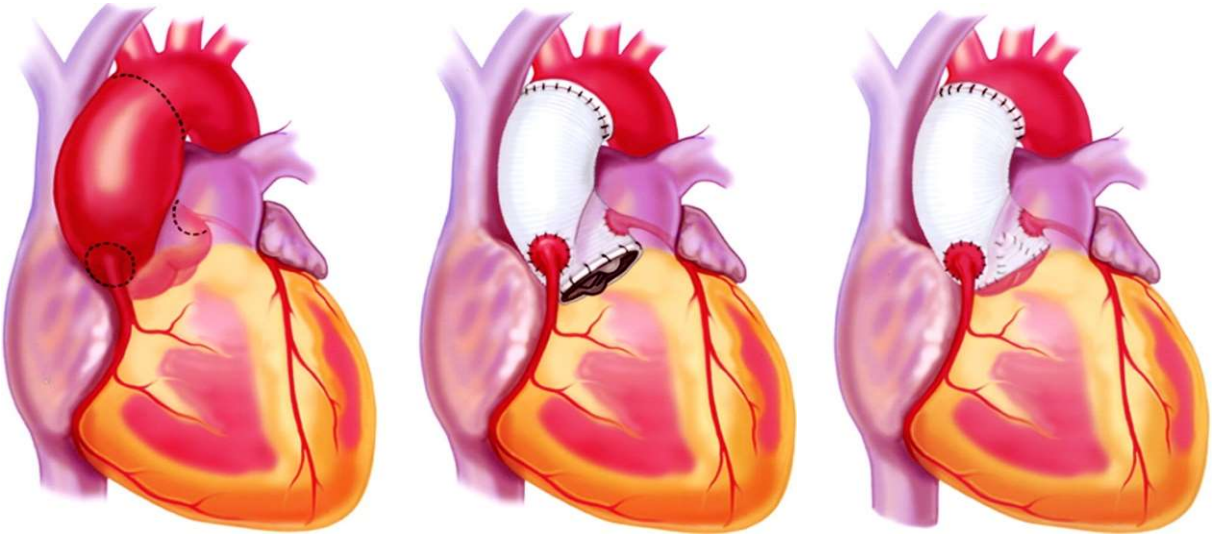

Figure 1.13. (a) aTAA before elective surgery. (b) Bentall technique for mCVG replacement. (c) David-I technique for VSR [21].

In last decades – basing on a pool of 890 patients operated consecutively at New York Presbyterian Hospital from 1997 to 2014 – the number of bCVG and VSRs performed progressively increased, while less and less patients are treated with a mCVG [19]. **Figure 1.14** shows the frequency of procedure type by years.

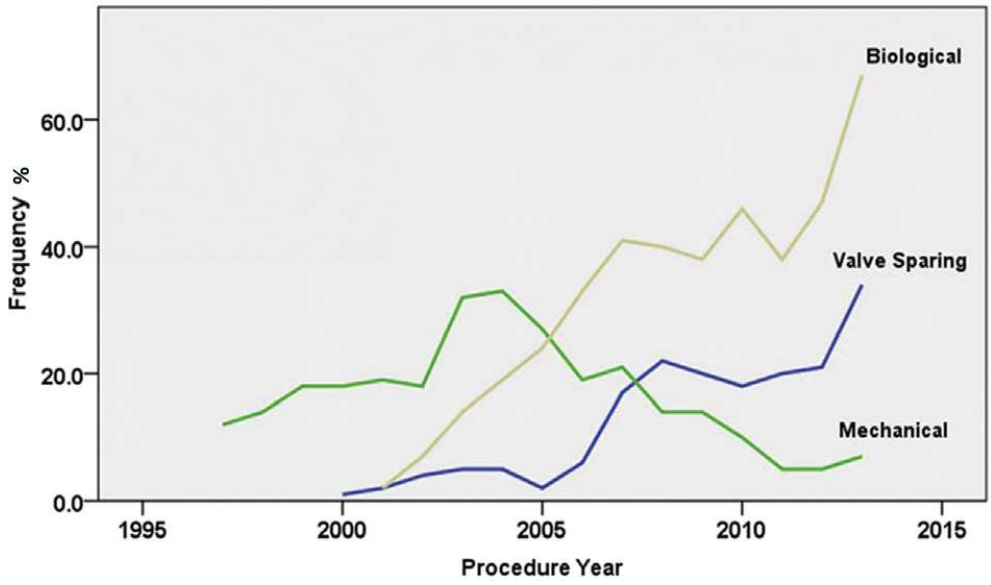

Figure 1.14. Frequency (%) of procedure type by year (1997-2015), based on the same pool as Figure 1.12.

1.5.3 Early outcome

Elective surgery is a consolidated procedure with a low unsuccess rate (0.2%). Operative deaths happen mainly in patients suffering from preexisting other conditions (e.g. respiratory insufficiency, ischemia…). Within the first 90 days from the operation, most patients are in good health, while others may have clinical complications.

These complications include new-onset transient atrial fibrillation (24% of patients), delayed pericardial effusion (12%), bleeding (3.5%), which requires re-exploration, gastrointestinal hemorrhage (1.6%), which may eventually lead to death, and wound infection (0.8%). Incidences of stroke, myocardial infarction and deep sternal wound infection are 0.5%, 0.1% and 0.1% respectively. Also, 11.2% of patients receive at least one blood transfusion [19] [22]. Three-year and 5-year survival rate are 94.8% and up to 89% respectively [19].

1.5.4 Long-term outcome

Success of aortic root reconstruction can be appreciated also in the long-term: the survival rate at 13 years is still >81%. However, sever complications may occur, mainly including aortic valve insufficiency, descending TAA formation and rupture and acute endocarditis that may lead to rheumatic fever [22].

Aortic valve insufficiency is treated by replacing the native unhealthy valve with a prosthetic one, opening the pre-implanted graft at the level of its largest diameter and sewing there the prosthetic valve. Endocarditis are pharmacologically treated with antibiotics, or in worst cases require surgery. TAAs must be treated surgically: possible procedures are endovascular aneurysm repair (EVAR), that consists in the placement of an expandable stent graft within the aorta, and open aortic surgery, more invasive for the patient [22] [23].

Survival rate and incidence of aortic reintervention are not the same for the different type of surgical procedure: during the follow up survival rate at 5 years is comparable for mCVG and bCVG treated patients and significantly better in VSR patients, while aortic reintervention rate at 5 years, is 1.0% for the mCVG patients, 2.4% for the bCVGs and 7.3% for the VSRs [19].

Clinical studies on long-term effects of ascending aorta reconstruction show positive outcomes, with relatively low incidence of complications, however the implantation of a PET graft alters blood fluid dynamics both in proximal and distal thoracic aorta, especially when performed with

a tubular graft. The re-creation of native sinus type anatomy in VSR has shown advantages such the restoration of normal aortic flow; however, straight tubular grafts are still the most used in surgery for the treatment of aTAA [24]. An altered hemodynamics can be the cause of the start of the atherogenic process [25][26][27], so the analysis of parameters such as blood velocity, wall shear stress (WSS), pulse wave velocity (PWV) can be an extremely useful tool in clinical follow up.

The most common tool used to study the postsurgical hemodynamic of patients who underwent m/bCVG replacement or VSR is phase-contrast magnetic resonance imaging (PC-MRI), also called 4D flow analysis [24]. 4D flow is a technique that permits to accomplish *in vivo* measurement of the local blood velocity of the patient. From the velocity field, pathlines can be obtained, WSS and other hemodynamic quantities.

A study conducted [24] among three different groups of patient – straight PET graft, Valsalva neo-sinuses and healthy control group – shows that no discernable alteration or anatomic difference can be appreciated through flow pathlines and no deviated systolic jet in general (**Figure 1.15**). Graft was implanted via VSR technique in both groups.

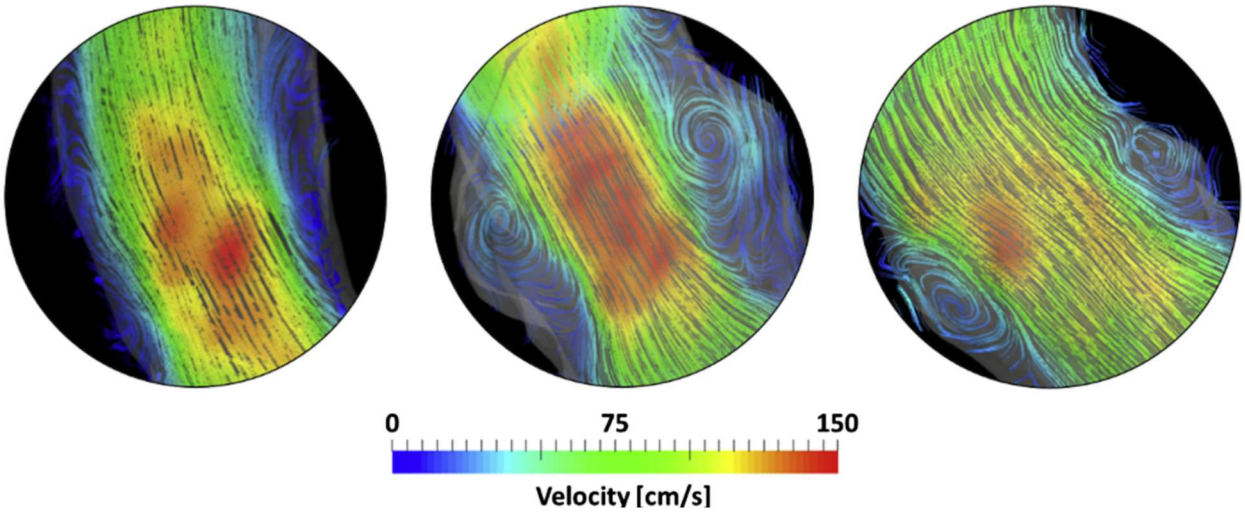

Figure 1.15. Visualization of 3-dimensional streamlines at the timeframe identified as peak systole at the level of sinuses of Valsava. From left to right a straight tubular graft, a neo-sinuses graft and a control patient.

However, differences in blood velocity and WSS volumetric distributions, both in the ascending and descending aorta, can be observed. Despite no statistically significant differences in terms of cardiac output, aortic diameter and heart rate, mean velocity in the ascending aorta results

higher in patients with straight tubular graft than Valsalva neo-sinuses and control patients. This difference is even more emphasized if the maximum velocity is considered. When considering the mid-descending aorta, these alterations are attenuated: maximum velocity is comparable between the 3 patient groups, while a higher mean velocity is found in patients with straight tubular graft.

Consistently with flow velocity alterations, WSS distribution is different in straight tube graft patients, when compared with neo-sinuses prosthesis or control group, with significantly higher values of maximum and mean WSS. This increase in WSS is observed both in ascending and descending aorta.

Variations in the velocity of blood flow is most likely due to the flow acceleration from lack of the physiological reservoir function of the native ascending aorta root. In fact, the PET graft is much stiffer than the native wall and without a compliant element to absorb kinetic energy of systole ejection, flow velocity results higher. In patients with neo-sinuses prosthesis, this latter partially accomplishes to the compliant role of the native aortic root, in facts velocities are comparable to the control group and lower than in patients in which reconstruction was performed with a straight tube Dacron graft.

The alteration of blood flow provokes changes in left ventricular afterload, coronary perfusion, aortic valve biomechanics and other components of cardiovascular system. At present, the long-term effects of these changes are still to be deepen. Intuitively, decreased WSS and more consistent laminar flow, that occur with the Valsalva neo-sinuses reconstruction, might positively influence late aneurysm formation in the descending aorta, especially in patients with connective tissue disorder such as MFS [24].

1.6 4D flow analysis

In recent years, magnetic resonance imaging (MRI) has become a very useful tool for the *in vivo* hemodynamic and functional assessment of different district in the human body. In particular, the time-resolved phase contrast MRI sequence (PC-MRI) with flow encoding in all spatial directions (4D-flow PC-MRI) plays a crucial role [28].

In this section, a brief description of the MRI system and the 4D-flow PC-MRI sequence will be given.

1.6.1 Basic physical principles of MRI

MRI is a medical imaging technique that uses magnetic fields and radio frequencies, to provide images of a specific anatomic district. Typical intensity of the applied magnetic field ranges between 0.2 T (Tesla) to 3 T, but also over 7 T in some cases [29].

MRI exploits the magnetic properties of the hydrogen-1 (protium) atoms, which are present in large quantities in soft tissues. Both characteristics enable utilization of the maximum amount of available magnetization in the body.

Hydrogen-1 proton spins around its axis producing a magnetic moment $\bar{\boldsymbol{\mu}}$, that is randomly oriented when no external magnetic field is applied (**Figure 1.16a-b**) [30].

When the primary magnet of the MRI machine applies a static magnetic field ($\bar{B}_0$), protons spins align either parallel or antiparallel to it (**Figure 1.16c**). Spins aren't static, they describe a precession motion around vector $\bar{B}_0$, so the transversal component of $\bar{\boldsymbol{\mu}}$ is randomly oriented. The precession angular velocity $\bar{\boldsymbol{\omega}}$ is given by Larmor equation:

$$\bar{\boldsymbol{\omega}} = -\gamma \bar{B}_0 \tag{1.1}$$

The proportionality constant γ is the gyromagnetic ratio, which depends on the nucleus of the activated element. For hydrogen-1, $\gamma = 42.57$ MHz/T [28].

Most of the spins assume a parallel configuration (*spin-up*) rather than an antiparallel one (*spin-down*), respectively corresponding to a low and a high energy state (*Zeeman effect*). This arrangement generates a net magnetic vector $\bar{M}_0$ called *longitudinal magnetization*, in the same direction of $\bar{B}_0$ [29].

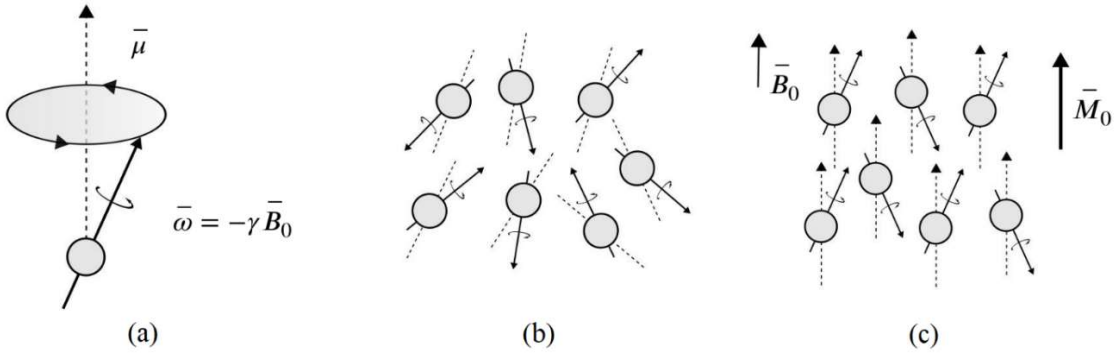

Figure 1.16. Nuclei possess a natural spin moment (a), randomly oriented (b) in space. When an external magnetic field is applied, spins align parallel o antiparallel to it (c).

The gradient magnets then generate a secondary rotating magnetic field orthogonal to the static one, called radiofrequency (RF) pulse. This allows to image directionally along different perpendicular directions, and hence for the 3D spatial encoding. The RF pulse switches *spin-up* protons to *spin-down* configuration and synchronize them making precess in phase. This cause a 90° turn of the net magnetization vector $\bar{M}_0$ to the transverse plane. The resulting vector $\bar{M}_{xy}$ is called *transverse magnetization*.

After the RF pulse, relaxation occurs and the transvers magnetization decay to zero, while the longitudinal magnetization returns to its equilibrium value M_0 (**Figure 1.17**). Relaxation is due to molecular interaction that has two different effects: interaction between spins and the surrounding tissue causes the realignment of $\bar{M}_0$ with $\bar{B}_0$ with time constant T_1, mutual interaction between spins causes the dephase of spins, hence the decay of $\bar{M}_{xy}$, with time constant T_2. This phenomenon induces an electric signal called *free induction decay* (FID), that depends on the protonic density, T_1 and T_2. FID is then converted by a computer in a digital signal, to which Fourier transforms are applied and images are reconstructed. MRI dataset are stored in DICOM format [29].

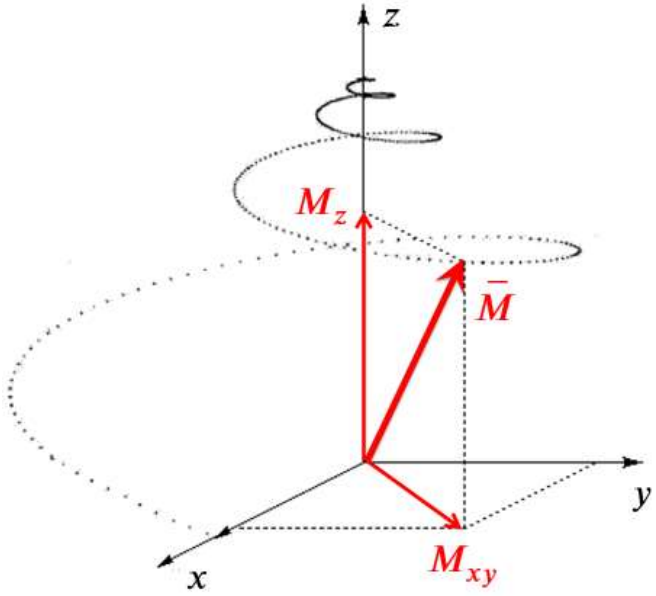

Figure 1.17. The resultant magnetization vector $\bar{M}$ describe a spiral motion over a spherical surface during relaxation, with its component M_{xy} decaying to zero and its component M_z returning to the equilibrium value M_0.

1.6.2 PC-MRI

Phase contrast MRI (PC-MRI) is a particular type of MRI developed in order to obtain functional measurements of moving blood [31]. At first, a magnetic field gradient G_0 is applied, causing protons subject to different magnetic field intensity to precess with different frequency. The phase shift is a function of the gradient and the position of the proton $r(\tau)$ [32]:

$$\phi = \gamma \int_0^t B_0 + G_0(\tau) \cdot r(\tau) d\tau \tag{1.2}$$

Where, B_0 is the static magnetic field and γ the gyromagnetic ratio. Then, a second magnetic field gradient is applied, opposite and equal in amplitude to the first. Protons accumulate a phase shift ($\Delta\phi$) along the direction of the gradient that can be calculated as:

$$\Delta\phi = v(\gamma \Delta M) \tag{1.3}$$

Where v is the spin velocity and ΔM the gradient moment difference. Phase shift is then used to calculate velocity in each voxel, with the following relationship:

$$v = \frac{VENC}{\pi} \Delta\phi \tag{1.4}$$

Where $VENC$ (velocity encoding) is a parameter set by the operator, depending on the amplitudes of the gradients used, that determinate the range of detectable velocities encoded by a PC sequence. It is a fundamental parameter in the acquisition, indeed a too low $VENC$ generates aliasing, while a too high value compromises the sensitivity and the signal-to-noise ratio of the measurement. Also, larger values of $VENC$ conceal smaller flow feature [32].

1.6.3 4D flow measurements

Applying three perpendicular magnetic field encoding gradients throughout a cardiac cycle, volumetric, temporal and 3-directional data are obtained. This technique is called 4D-flow MRI. It exploits the same method of PC-MRI with three different magnetic field gradient combinations, each encoding blood velocities along a direction. The $VENC$ value can be set independently in three acquisitions [33].

Despite its potentialities in providing invaluable *in vivo* measurements of blood fluid dynamic, 4D flow still has some limitations:

- Motion artifacts cannot be avoided, like the motion of lungs and heart. This issue is partially overcome using prospective and retrospective cardiac gating, even if resulting velocities are averaged over multiple cardiac cycles.
- In voxels located at the boundary between stationary and moving tissue the phase shift is an average of both stationary and flowing spins. This causes unreliable velocity measurement and partial volume effects.
- In case of turbulent flow an inadequate spatial and temporal resolution fail in detecting aspects of the flow present at the sub-voxel scale [34].

However, for large arteries 4D-flow has been proven to be a valid approach in the analysis of the hemodynamic [35][36], providing results consistent with *in vivo* measurement available in literature. Several studies show that a correlation exists between patient hemodynamic and its cardiovascular health condition, hence, 4D-flow measurements can provide useful biomarkers that play a significant role in the arising and development of pathologies.

Velocity measurement

Velocity is directly measured (Equation 1.4) from 4D-flow images exploiting the sequence $VENC$. Flow rate measurement can be obtained integrating velocities over the area of interest:

$$Q = \iint_{Area} \overline{v}\, \overline{dA} \tag{1.5}$$

Flow rate can be computed throughout the cardiac cycle, providing useful data such as the cardiac output. Measurements of velocities and flow rate can be used to validate numerical models [37] or to obtain patient-specific boundary conditions (**Figure 1.18**) to be applied [38][39].

Wall shear stress measurement

Wall shear stress (WSS) measures the drag force experienced by endothelial cells due to blood flow. It has been showed that alteration in the WSS distribution play a significant role in the development of some cardiovascular disease [26][40]. In atherosclerotic patients, plaque

formation has been reported to occur in regions of low oscillatory WSS [26]. However, the role played by WSS in aneurysm is controversial, due to the complexity of its pathophysiology.

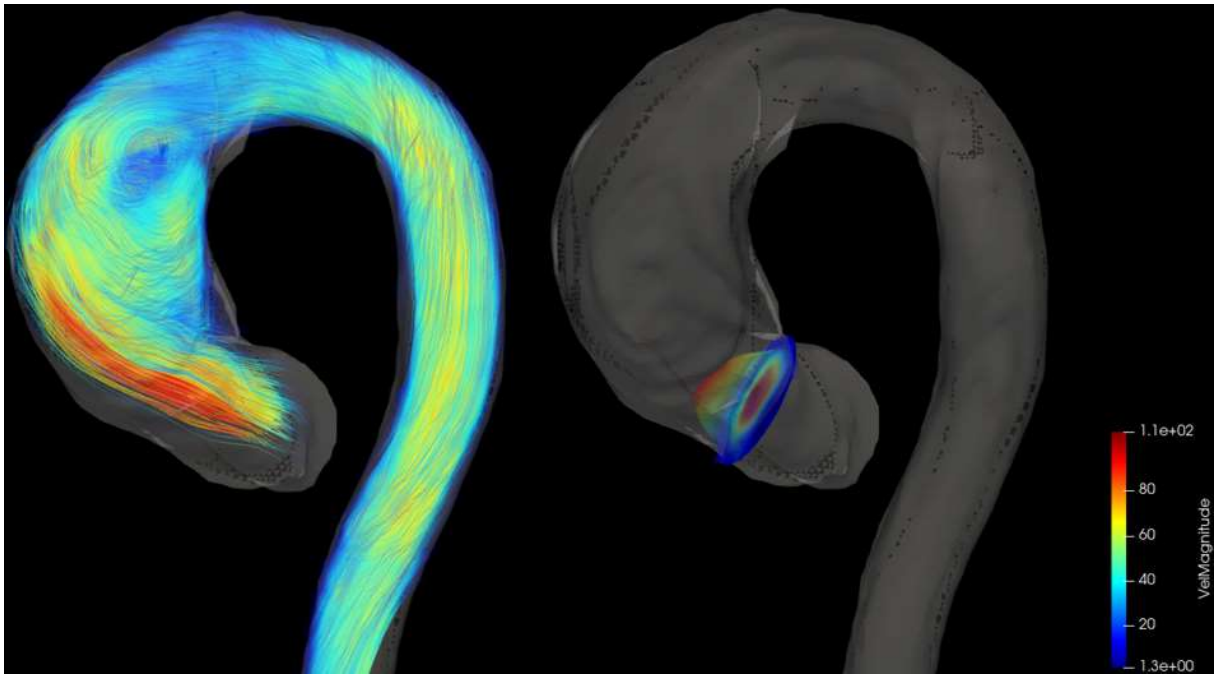

Figure 1.18. Example of velocity visualization from 4d-flow imaging. Velocity map at the aortic inlet can be set as boundary condition for numerical simulations, streamlines can be used to validate results.

Both high and low WSS can drive to initiation, growth and eventually rupture of the aneurysm depending on its phenotype. Low WSS and high oscillatory shear index (OSI) can trigger an inflammatory-cell-mediated pathway, associated to the growth and rupture of large atherosclerosis aneurysm phenotype. High WSS triggers a mural-cell-mediated pathway, causing the growth and rupture of bleb aneurysm phenotype [27]. Therefore, measuring *in vivo* WSS without developing a numerical model (that is time expensive and requires engineering experts), can deepen the understanding of many cardiovascular disease development.
By definition, WSS is given by:

$$\tau := \mu \frac{\partial \bar{\boldsymbol{v}}}{\partial \bar{\boldsymbol{n}}}\bigg|_{wall} \tag{1.6}$$

Where $\bar{\boldsymbol{v}}$ is blood velocity, μ is its dynamic viscosity and $\bar{\boldsymbol{n}}$ is the unit vector normal to the vessel wall. An accurate segmentation of the lumen is fundamental, to have a proper estimation of the velocity gradient along the perpendicular direction.

Although 4D-flow MRI results may not be accurate as CFD ones, due to its limited spatial and temporal resolution, it is able to capture correctly the WSS distribution, which is still a useful information in clinical analysis. However, to obtain more reliable WSS values, numerical models are still the best option [41].

1.7 Conclusions

This introduction provided an overview on the anatomy, the physiology and the main pathologies of the aorta, pointing out the clinical significance of a deeper insight into the development of diseases such as TAA. Complications associated with TAA (e.g. rupture, dissection) and with surgical reconstruction procedure (e.g. aortic valve insufficiency, hypertension, re-formation of a TAA) are life-threatening for patients. Hence, the identification of hemodynamic biomarkers, that play a role in the initiation and growth of TAA is an aspect of great interest in the clinical routine. 4D flow MRI is a strong tool that provides *in vivo* accurate measurements of blood velocity, in terms of streamlines and components magnitude.

However, 4D flow is not so accurate in the measurement of velocity gradients proximal to the vessel wall, and consequently in the computation of WSS, which has been proven to be a possible biomarker for the growth of aneurysm. Moreover, 4D flow cannot predict how blood flow will develop in a patient, it limits to provide an instantaneous measure.

Numerical models can go beyond 4D flow limitations due to its spatial and temporal resolution and provide not only accurate values of WSS but also a deep insight into the interaction between the arterial wall and blood. This work will exploit fluid-structure numerical model potentialities to compare the hemodynamic of a patient before and after graft replacement of the ascending aorta, as well as the role played by the PET graft implanted in the structural behavior of the aortic wall and possible fluid dynamics alteration in blood flow. Compared to 4D flow, numerical models possess a predictive capacity to get hemodynamics quantities, since results depend on how the problem is conditioned. This capability may be of great interest for clinical studies.

Chapter 2
State of Art

Chapter summary

In this chapter different methods for the modeling of structural, fluid dynamics and fluid-structure interaction analysis are presented. In the first part, the governing equations and three different kinematic descriptions, Lagrangian, Eulerian and ALE (Arbitrary Lagrangian Eulerian), are introduced. In the second part of the chapter, three numerical approaches for the modeling of the aorta, to date available in literature, are analyzed. Attention was payed specifically on the choices of the authors for the reconstruction of the geometry, the assignment of material properties and the assignment of the boundary conditions.

2.1 Introduction

It's been recognized that the forces and stresses that SMCs experience in cardiovascular system are peculiar for the development of several cardiovascular diseases. Despite the significant progress in clinical care, these remain an important cause of morbidity and mortality. In the thoracic aorta, due to its complex geometry and high blood pressure (~120/80 mmHg), the prevalence of cardiovascular disease (e.g. atherosclerosis, aneurysm, dissection) is higher.

The development of computational fluid dynamics (CFD) and fluid-structure interaction (FSI) modeling in the last decades has enabled the use of 3D numerical simulations to investigate patient-specific hemodynamics and to understand the origin and development of several diseases. The main advantages of CFD and FSI are the capability of quantifying variables complicated to measure *in vivo* or *in vitro*, their reproducibility and their predictive capability in providing hemodynamic indexes associated with different cardiovascular diseases. With respect to *in vitro* studies, CFD and FSI are more suitable for parametrization of model properties or boundary conditions.

The first step to develop a numerical model of the thoracic aorta is obtaining the morphology of the artery. Most of the studies are now performed on image-based patient-specific models, that permit to obtain more realistic hemodynamics. The most common imaging techniques used to reconstruct arterial geometries are magnetic resonance angiography (MRA) and computer tomography (CT). Then material properties and boundary conditions are assigned [42].

Combining a high-resolution technique and image-based measurements data, CFD and FSI provide a reliable tool for realistic modelling of the arterial blood flow. However, some simplifications are required, for example on the viscosity of blood, on its flow conditions, etc. CFD modeling requires a very strong assumption: the arterial wall is assumed rigid, while of course it deforms under loads (i.e. blood pressure). In the thoracic aorta the deformation is not negligible and thus, it cannot be approximated by a rigid wall; indeed the motion of the arterial wall affects the blood flow dynamics and vice-versa, moreover wave propagation phenomena can be modelled only if deformability is considered. In recent years, significant progress has been made in the area of FSI models, that account for the deformation of solids interacting with the fluid domain.

Compared to a rigid wall model, FSI can provide a more accurate physiological description of the hemodynamics, as well as the arterial wall strain. Of course, it strongly depends on the tissue of the vessel of interest, hence a prerequisite to simulate realistic hemodynamics is the development of a patient-specific constitutive models for the arterial wall. This is very challenging, since wall properties are difficult to obtain experimentally or often unknown [42]. No gold-standard has been defined for hemodynamic simulation of aTAA, although it has been suggested that, it may be possible that the stiffening of the aneurysm wall makes the rigid wall hypothesis reasonable, since CFD and FSI give similar results [43].
With this thesis work, we want to exploit FSI modeling potentialities for a deep insight analysis of the effects of the reconstruction of the ascending aorta with a PET graft. Also, we want to compare the result that can be obtained with a less expensive but simpler CFD model.

2.2 Fluid-Structure Interaction

FSI models combine structural mechanical analysis and fluid dynamics simulations. This allows to obtain more realistic models, but at the same time very complex models and for these no analytical solution is available. Therefore, they require numerical codes to be solved.
There are two main approaches for the solution of an FSI problem:

- *Monolithic approach*. The governing equations, both for the structural and fluid dynamics part, are solve at once and all the variables (e.g. displacement, pressure, velocity) are updated at the same time.
- *Partitioned approach*. Structural and fluid governing equations are solved separately with two different solvers coupled with staggered iteration process. The solution of one solver is used as a boundary condition for the other at the fluid-solid interface at each coupling iteration.

The physics that describes the interaction between blood and the aortic wall is very complex, thus, some approximations are required, firstly, the choice of the coupling algorithm between the fluid and solid domain. The choice a crucial for the develop of a realistic model, in fact the usage of the wrong algorithm for the problem may result in unreliable solutions.
Depending on the problem to solve, two coupling algorithms are available:

- *Weak coupling (1-way FSI) algorithm*. The basic idea of this method is that the deformation of the solid domain slightly affects the fluid dynamics of the whole system. Thus, a convergent solution is obtained for the fluid model, used as a boundary condition or external load for the solid model that is solved in turn. Coupling occurs between fluid and solid but not vice versa. More precisely fluid pressure at the interface of the domains is computed from a CFD simulation and applied in the structural analysis as external load.
- *Strong coupling (2-way FSI) algorithm*. The method is based on the idea that the fluid dynamics causes deformations in the solid domain that alter the fluid dynamics itself. The two fields remain very tightly coupled, to obtain a correct continuity between their dynamics. Forces and displacements are updated at each time increment.

Furthermore, 2-way FSI, can be differentiated based on the numerical approximation method for partial differential equations (PDEs) that describe the fluid and solid mode.

- *Implicit method*. This method is based on the *backward Euler scheme* for differential approximation. The solution is re-computed through many iterations at each time step, until the balance of external loads and internal forces is reached. This method is absolutely stable, but more computationally expensive and the solver may not be able to find a solution for the problem. Derivatives are approximated with the following formula:

$$\frac{df}{dt}(t+\Delta t) = \frac{f(t+\Delta t) - f(t)}{\Delta t} \tag{2.1}$$

- *Explicit method*. This method is based on the *forward Euler scheme* for differential approximation. The solution is computed from the previous time step and it's constant during it. Stability is not ensured, hence convergence criteria are generally defined. Derivatives are approximated with the following formula:

$$\frac{df}{dt}(t) = \frac{f(t+\Delta t) - f(t)}{\Delta t} \tag{2.2}$$

Even if the implicit method provides more accurate results, it may require very high computational costs; for this reason, choosing an explicit method and a smaller time step is a good compromise to obtain good accuracy levels and lower computational costs.

FSI modelling provides results that should be more comprehensive and accurate – with respect to CFD – however, it is affected by some limitations and issues. First, this method requires very high computational costs, higher than structural analysis or computational fluid-dynamics (CFD), hence, to achieve reasonable simulation times introducing some simplifications is fundamental.

2.3 Background equations

The kinematics of the solid and fluid domain (schematized in **Figure 2.1**) can be described with two approaches: the *Lagrangian description* and the *Eulerian description*. Both present advantages and disadvantages, that will be deepen in this section. A general description of the governing equations of both domains will be given too.

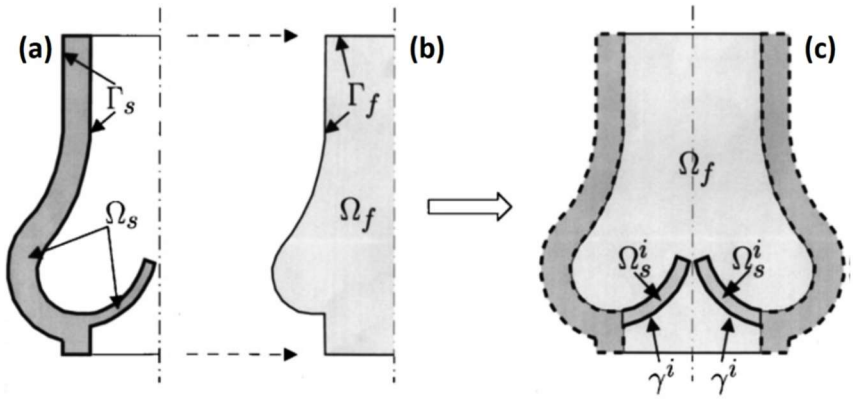

Figure 2.1. Schematic sample of a solid domain (a) in contact with a fluid (b). Description of their interaction (c).

2.3.1 Kinematic description

Numerical simulations of multidimensional problems in fluid dynamics and solid mechanics often involve large distortion of the continuum, therefore the choice of a proper kinematic description is fundamental. Such choice determines the relationship between the deforming continuum and the finite grid of the mesh zone, and the ability of the numerical code to deal with large distortion and provide an accurate solution, especially for material interface and mobile boundaries.

Algorithms for continuum mechanics generally use two classical approaches for the description of motion: the *Lagrangian description* and the *Eulerian description*.

- The *Lagrangian approach* is tipically exploited for structural simulations. It consists in tracing the motion of each particle of the continuum (**Figure 2.2a**): the individual node of the computational mesh follows the associated material particle (**Figure 2.2b**). This allows a comprehensive tracking of the nodes in the interfaces between different materials and in free surfaces. Since every element of the mesh is permanently connected to the same material point, this description makes easier to deal with material with history-dependent constitutive relations.

  The Lagrangian method may lose accuracy when dealing with large distortions of the computational domain. A frequent remeshing is mandatory in that case, which in some cases may lead to the inability to conclude the numerical simulation, due to excessive distortion of the mesh.

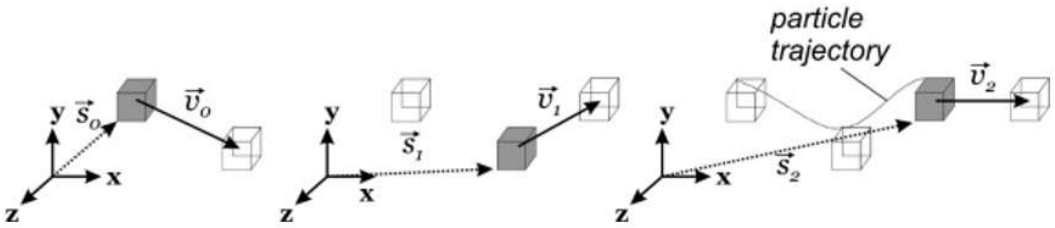

(a)

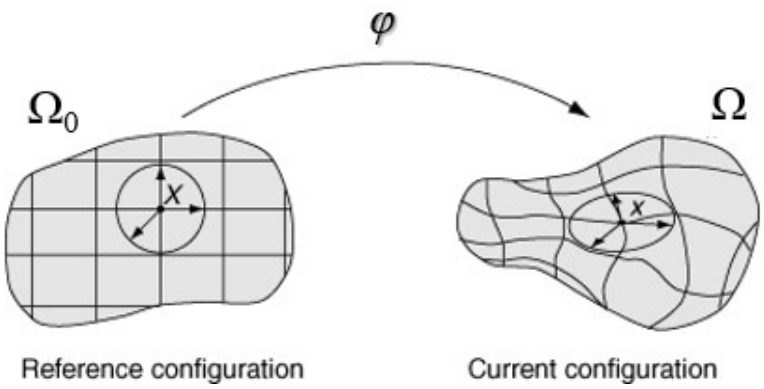

(b)

Figure 2.2 Lagrangian kinematic description of motion. The position $\bar{s}_i$ of the same particle is traced at different time instants in the reference configuration system Ω_0 (a). The deformation of the continuum (b) from the reference (Ω_0) to the current configuration (Ω) is described by the application φ.

The motion of the material point $\bar{\mathbf{x}}_0$, from the reference configuration to the current one in $\bar{\mathbf{x}}$ is defined by the following application φ:

$$\varphi: \Omega_0 \times [t_0, t_{final}[\longrightarrow \Omega \times [t_0, t_{final}[\tag{2.3}$$

$$\left(\bar{\mathbf{x}}_0, t\right) \longrightarrow \varphi\left(\bar{\mathbf{x}}_0, t\right) = \left(\bar{\mathbf{x}}, t\right) \tag{2.4}$$

This allows to link $\bar{\mathbf{x}}_0$ and $\bar{\mathbf{x}}$ in time by a law of motion.

$$\bar{\mathbf{x}} = \bar{\mathbf{x}}\left(\bar{\mathbf{x}}_0, t\right), \qquad t = t \tag{2.5}$$

Ω_0 and Ω represent the material domain in the initial and current configuration respectively. The spatial coordinate $\bar{\mathbf{x}}$ depends on the material point $\bar{\mathbf{x}}_0$ and time, which is measured by the same variable in both the domains.

The deformation of the continuum is described through the deformation gradient tensor $\bar{\mathbf{F}}$, defined as:

$$\bar{\mathbf{F}} = \frac{\partial \bar{\mathbf{x}}}{\partial \bar{\mathbf{x}}_0} \tag{2.6}$$

For incompressible materials, the determinant of $\bar{\mathbf{F}}$ (i.e. the Jacobian) is equal to 1:

$$\mathrm{J} = \det \bar{\mathbf{F}} = 1 \text{ (for incompressible materials)} \tag{2.7}$$

- The *Eulerian approach* is widely used in fluid dynamics simulations: the physical quantities associated with a particle of fluid passing through a fixed region of space are examined (**Figure 2.3**).

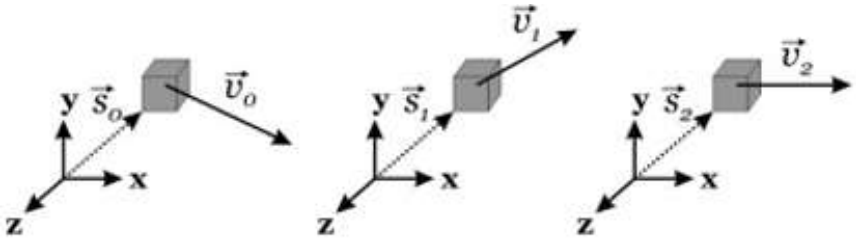

Figure 2.3. Different particles pass through the same control volume at position $\bar{s}_i$ at different time.

The mesh is fixed, and the continuum moves with respect to the grid. The conservation equations are written in terms of the spatial coordinate and time. The quantities and functions involved in this description have an instantaneous significance: the material velocity, in a given control volume, corresponds to the velocity of the material point crossing it at the considered time, with no dependence on its initial position in the reference configuration. Hence, velocity can be expressed as a function of the fixed-element mesh and time only:

$$\phi: \bar{\mathbf{v}} = \bar{\mathbf{v}}\left(\bar{\mathbf{x}}, t\right) \tag{2.8}$$

Large distortions in the continuum motion can be handled relatively easily, but at the expense of precise interface definition and resolution of flow details. This approach permits an easy treatment of complex material motion, but it presents some numerical difficulties: since the mesh is dissociated from the material particles, convective effects due to the relative motion of the grid and the material appear and these are not trivial to handle [44].

2.3.2 Solid domain

The solid domain Ω_s (**Figure 2.1a**) can be described by the elastodynamic equation of motion, which account for the solid deformation due to the forces applied by the fluid, under the hypothesis of incompressible material (J = 1).

$$\rho_s \frac{\partial^2 \bar{\boldsymbol{u}}_s}{\partial t^2} = \nabla \cdot \bar{\boldsymbol{\sigma}}_s - \rho_s \bar{\mathbf{f}}_s \tag{2.9}$$

Where ρ_s is the solid density, $\bar{\boldsymbol{u}}_s$ is the displacement vector, $\bar{\boldsymbol{\sigma}}_s$ is the Cauchy stress tensor and $\bar{\mathbf{f}}_s$ is a vector representing surface forces applied to the structure.

The **Equation 2.9** must be completed with a proper set of boundary conditions on the surfaces Γ_s, especially those shared with the fluid [44]. Continuity (i.e. conservation of mass) is ensured by the condition of incompressible material.

2.3.3 Fluid domain

If it's possible to assume a Newtonian incompressible behavior for the fluid, its flow within the domain Ω_f (**Figure 2.1b**), bounded by the surfaces Γ_f can be described by the following continuity equation and Navier-Stokes equation (momentum equation):

$$\begin{cases} \nabla \cdot \bar{\mathbf{v}}_f = 0 & (2.10) \\ \rho_f \left(\dfrac{\partial \bar{\mathbf{v}}_f}{\partial t} + (\bar{\mathbf{v}}_f \cdot \nabla) \bar{\mathbf{v}}_f \right) = -\nabla p + \nabla \bar{\boldsymbol{\tau}}_f + \rho_f \bar{\mathbf{f}}_f & (2.11) \end{cases}$$

Where $\bar{\mathbf{v}}_f$ is the fluid velocity, ρ_f its density, p is the pressure, $\bar{\boldsymbol{\tau}}_f$ is the viscous stress tensor and $\bar{\mathbf{f}}_f$ is the body forces vector. In the Navier-Stokes equation, first member represents the transient and convective forces, while the second member represents pressure, viscous and volumetric forces.

For an isotropic, incompressible and Newtonian fluid, the viscous stress tensor $\bar{\boldsymbol{\tau}}_f$ is defined as:

$$\bar{\boldsymbol{\tau}}_f = 2\mu \bar{\mathbf{S}} \tag{2.12}$$

Where μ is the dynamic viscosity of the fluid and $\bar{\mathbf{S}}$ is the strain rate tensor, defined as:

$$\bar{\mathbf{S}} = \frac{1}{2} \left(\nabla \bar{\mathbf{v}}_f + \left(\nabla \bar{\mathbf{v}}_f \right)^T \right) \tag{2.13}$$

Equations 2.10 and **2.11** must be coupled with proper Dirichlet or Neumann boundary conditions [44].

2.3.4 ALE kinematic description

It is possible to combine the Lagrangian and Eulerian approaches to obtain a generalized kinematic description of motion. This method is called *Arbitrary Lagrangian-Eulerian* (ALE) *description*. In the ALE approach, the nodes of the mesh can be moved with the continuum, as in the Lagrangian manner, or be held fixed, as in the Eulerian one, or can be moved in some arbitrary specified way to give a continuous rezoning capability. **Figure 2.4** shows a comparison between the Lagrangian, Eulerian and ALE description.

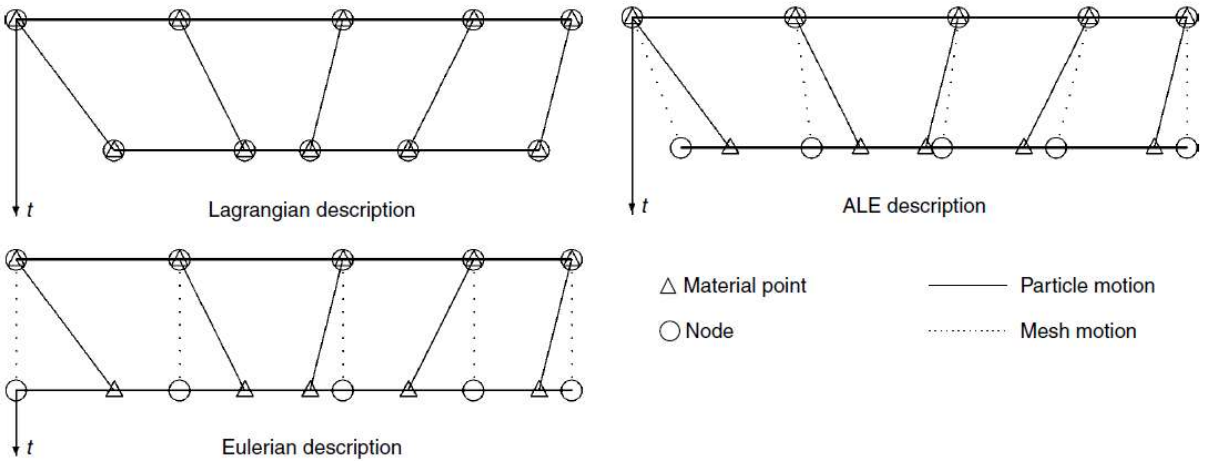

Figure 2.4. One dimensional example of Lagrangian, Eulerian and ALE mesh and particle motion.

In the ALE description of motion, the reference configuration isn't identified with the initial one Ω_0, either the current one Ω. A third domain is needed, the auxiliary configuration Ω_χ where the auxiliary coordinates $\bar{\chi}$ are introduced to identify the grid points. **Figure 2.5** shows the relationship between these domains, and the one-to-one mappings that relate them, highlighting that the motion of the ALE computational mesh is independent of the material motion.

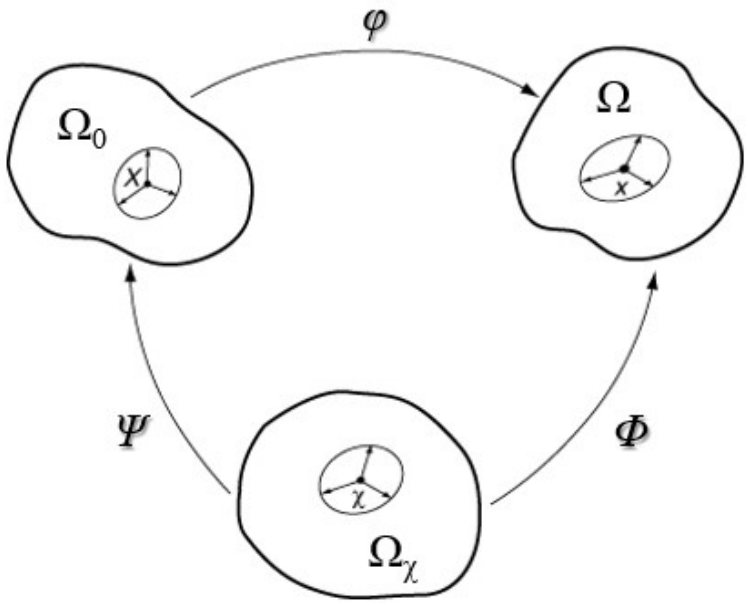

Figure 2.5. Schematic representation of the correlation between Ω_0, Ω and Ω_χ. The referential configuration is mapped into the initial and current one by the applications Ψ and Φ respectively. The particle motion is expressed by the composition of these two: $\varphi = \Phi \circ \Psi^{-1}$.

In order to express the conservation equations in the ALE kinematic description, it is necessary to relate the total time derivative, which appears in conservation laws, and the time derivative in the referential configuration. For a generic scalar physical quantity $f\left(\bar{\mathbf{x}},t\right)$, the fundamental ALE relation between total and referential time derivatives and spatial gradient is the following:

$$\left.\frac{\partial f}{\partial t}\right|_{\Omega_0} = \left.\frac{\partial f}{\partial t}\right|_{\Omega_\chi} + \frac{\partial f}{\partial \bar{\mathbf{x}}} \cdot \bar{\boldsymbol{c}} \tag{2.14}$$

Equation 2.14 shows that time derivative of physical quantity in the initial configuration (i.e. the total time derivative) is given by the local time derivative, with the referential coordinate $\bar{\boldsymbol{\chi}}$ fixed, plus a convective term that accounts for the relative velocity $\bar{\boldsymbol{c}} = \bar{\mathbf{v}} - \hat{\mathbf{v}}$, between the material and the reference system. $\hat{\mathbf{v}}$ is the velocity of the mesh.

The ALE differential form of conservation equation can be obtained by replacing the material velocity $\bar{\mathbf{v}}$, with the convective velocity $\bar{\boldsymbol{c}}$, in the Eulerian form of the equations. The result is the following:

$$\left.\frac{\partial \rho}{\partial t}\right|_{\Omega_\chi} + \bar{\boldsymbol{c}} \cdot \nabla \rho = -\rho \nabla \cdot \bar{\mathbf{v}} \tag{2.15}$$

$$\rho\left(\left.\frac{\partial \bar{\mathbf{v}}}{\partial t}\right|_{\Omega_\chi} + \left(\bar{\boldsymbol{c}} \cdot \nabla\right)\bar{\mathbf{v}}\right) = \nabla \cdot \bar{\boldsymbol{\sigma}} + \rho \bar{\mathbf{b}} \tag{2.16}$$

$$\rho\left(\left.\frac{\partial W}{\partial t}\right|_{\Omega_\chi} + \bar{\boldsymbol{c}} \cdot \nabla W\right) = \nabla \cdot \left(\bar{\boldsymbol{\sigma}} \cdot \bar{\mathbf{v}}\right) + \bar{\mathbf{v}} \cdot \rho \bar{\mathbf{b}} \tag{2.17}$$

Equations 2.15, **2.16** and **2.17** express the conservation of mass, linear momentum and total energy respectively; ρ is the material density, $\bar{\mathbf{v}}$ its velocity, $\bar{\boldsymbol{\sigma}}$ is the Cauchy stress tensor, $\bar{\mathbf{b}}$ is the body force vector and W is the material specific total energy.

The arbitrary motion of the computational grid is reflected only in the left-hand side terms, while the right-hand side is written in the classical Eulerian form. For this reason, the ALE approach is also known as *quasi-Eulerian description*.

2.4 Aortic numerical models

Many studies on the modeling of the aorta can be found in literature. While patient specific CFD is a well-established method to study the hemodynamics of a subject, the interest in more complete FSI models, capable of providing a deeper insight in the biomechanics of the vessel, is increasingly growing. Physical quantities of clinical interest, like the distensibility of the aortic wall, the intramural stress, pulse wave velocity (PWV), which depend on the mechanics of the wall, cannot be predicted by a simple CFD model, while FSI successfully achieves to provide them [43][45][46][47].

In literature, both models on idealized geometry [48][49][50] of human vessels and patient specific models [43][51][52] can be found. Ideal geometries are generally used in studies that adopt a hyperelastic constitutive model for the arterial wall, while in patient specific FSI models, it's common to use a linear elastic model.

Various works [43][50][51] focused on the comparison between CFD and FSI modeling, to understand whether or not, the same solution obtained from an FSI simulation, can be obtained with a simpler CFD simulation. However, no common agreement was found.

Herein, a description of three representative patient specific FSI modeling approach (**Table 2.1**) will be provided, focusing on three main aspects:

- The geometry of the fluid and solid domain (i.e. blood and arterial wall), and their physical properties.
- The boundary conditions applied to the fluid and the solid.
- The fluid dynamic and structural characterization accomplished.

Authors	Savabi *et al.* [52]	Mendez *et al.* [43]	Campobasso *et al.* [38]
Geometry	Patient specific aorta	Patient specific aorta	Patient specific aorta
Software	Mechanical APDL + Fluent v.19.1	ABAQUS v.6.12 + Fluent v.14.0	Mechanical APDL + Fluent v.17.2
Solid mesh	Prisms	Shells (quadrilateral)	Tetrahedrons
Fluid mesh	Tetrahedrons	Tetrahedrons	Tetrahedrons

Table 2.1. Main characteristic of the literature works that were analyzed.

Sabavi *et al*. implemented an FSI model to evaluate hemodynamic forces acting on specific position in the aortic arch, where baroceptors are located. The circumferential stretch of the wall was assumed as criterion to quantify the functioning of baroceptors. Velocity field, wall shear stress and pressure in the fluid domain and stress, strain and displacement of the arterial wall were also discussed.

Campobasso *et al.* focused their analysis, a 2-way FSI, on the effect of the aortic stiffness and peripheral resistance on the peak wall stress in the aTAA. They suggested that intramural stress may be a criterion to quantify the risk of rupture of an aTAA, accounting for the combined effects of hypertension and aortic stiffness increase [38].

Mendez *et al*. performed a sensitivity analysis of the solver. They compared the results obtained from a finite element analysis (FEA), a CFD and a 2-way FSI simulation of aTAA, performed on 5 patients. Since there is no gold-standard for the assessment of the hemodynamics and structural mechanics of aTAAs, the aim of their work was to determine whether simply FEA or CFD modelling would give similar predictions of structural and hemodynamic parameters as compared to 2-way FSI analysis. Thus, their work is focused on the ability of computational modelling to replicate the aneurysm pathophysiology in a less complex fashion as possible. Furthermore, they discussed the relevance of the aneurysmal wall stiffening in determining parameters of clinical importance (e.g. the wall shear stress) [43].

2.4.1 Fluid and solid domain

Savabi *et al.* reconstructed the patient specific geometry of the aorta from 1.5 T MRI of a 42 years old patient, with no specific cardiovascular disease. Images were acquired with the following parameters: field of view (FOV) = 299 mm, voxel size = 0.510 × 0.510 × 2 mm. The 3D model of the geometry was obtained in Mimics (Materialise NV, Leuven, Belgium) and adjusted in SolidWorks (Dassault System, Velizy-Villacoulblay, France). The geometry was extruded in normal direction by 1 mm to create the solid domain (i.e. the arterial wall). The fluid and solid geometries are shown in **Figure 2.5**.

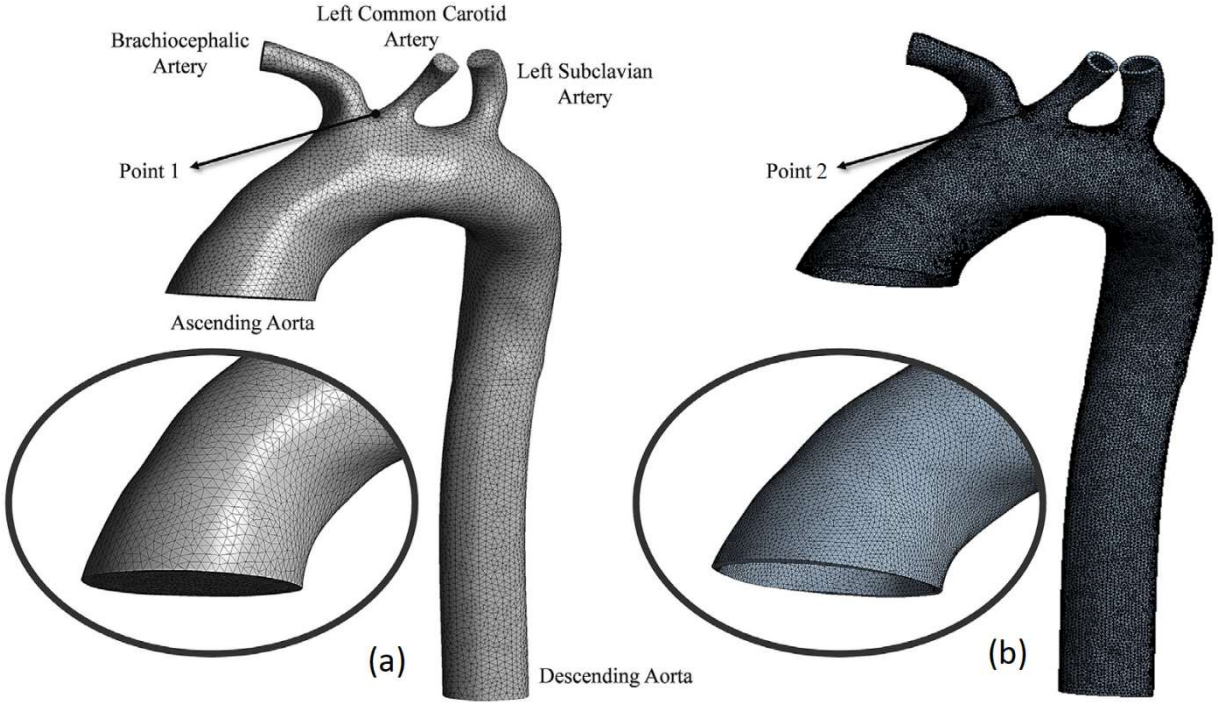

Figure 2.5. The fluid (a) and solid (b) meshed domains used in Savabi *et al*. work. The model included the aortic arch, the three supra-aortic branches and the whole descending aorta.

The fluid domain was discretized to ~230k tetrahedral elements, while the solid domain was discretized to 26.5k elements. ANSYS Meshing (ANSYS Inc., Canonsburg, PA, USA) embedded tool was used to generate both meshes. Flow was assumed to be laminar (typical Reynolds number ($\mathscr{R}e$) in the aorta is equal to 867 and flow is laminar for value of $\mathscr{R}e < 2000$) and blood was modelled as a Newtonian fluid with a density of 1050 kg/m^3 and a viscosity of 0.035 Pa · s.

Campobasso *et al.* reconstructed the geometry of the aorta of a consent patient scanned on a 3T MRI scanner without contrast, using a 4D flow phase contrast protocol and sequence. Acquisition was performed with a true spatial resolution of 1.9 × 1.9 × 2.2 mm and a VENC equal to 350 cm/s. The 4D flow MRI data were visualized using cvi^{42}® 4D flow module. CRIMSON software was used for the reconstruction of the fluid domain (**Figure 2.6**), including the ascending aorta, the supra-aortic branches and the proximal descending aorta. The solid domain was extruded from the fluid one, in outer normal direction and by a constant thickness value of 1.5 mm [38].

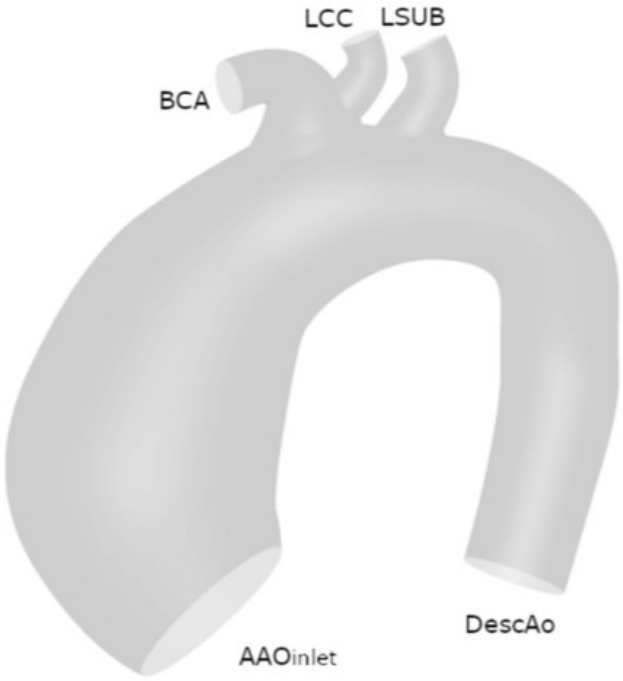

Figure 2.6. 3D geometric model used in Campobasso *et al.* study.

The structural and fluid mesh were both generated in ANSYS Icem v.17.2. A 6.1 million tetrahedral elements (average size 1 mm) was chosen for the fluid domain and a tetrahedral mesh (average size 3.5 mm) was used for the structural domain.

The aortic wall was assumed to be isotropic linear elastic, with a Young modulus equal to 2 and 10 MPa. Blood flow was assumed to be laminar, incompressible and non-Newtonian, with a density of 1060 kg/m^3. For the non-Newtonian behavior of blood, Carreau model was adopted:

$$\mu = \frac{\mu(\dot{\gamma}) - \mu_\infty}{\mu_0 - \mu_\infty}, \qquad \mu_0 = 0.056 \text{ Pa} \cdot \text{s}, \qquad \mu_\infty = 0.0345 \text{ Pa} \cdot \text{s} \tag{2.20}$$

$$\mu(\dot{\gamma}) = \left(1 + (\lambda\dot{\gamma})^2\right)^{(n-2)/2}, \qquad \lambda = 3.313 \text{ s}, \qquad n = 0.3568 \tag{2.21}$$

Where μ is the dynamic viscosity which depends on the shear rate $\dot{\gamma}$ [53].

Mendez *et al*. used electrocardiogram-gated computed tomography angiographic data (ECG-gated CTA) to reconstruct the geometry of the model. Reconstruction of the whole aorta, inclusive of the aortic valve and the supra-aortic branches, was performed using Mimics v.17. Specifically, a semi-automatic threshold-based segmentation of the aortic lumen was performed, to obtain a point cloud of the aTAA geometry. Once obtained the geometry, it was exported to

ANSYS Icem v.14.0, to generate the mesh of the fluid and the solid domain. A mesh (**Figure 2.7**) of ~1.1 million of unstructured tetrahedral elements for the fluid domain and a mesh of ~0.3 million of quadrilateral shell elements for the solid domain were obtained [43].

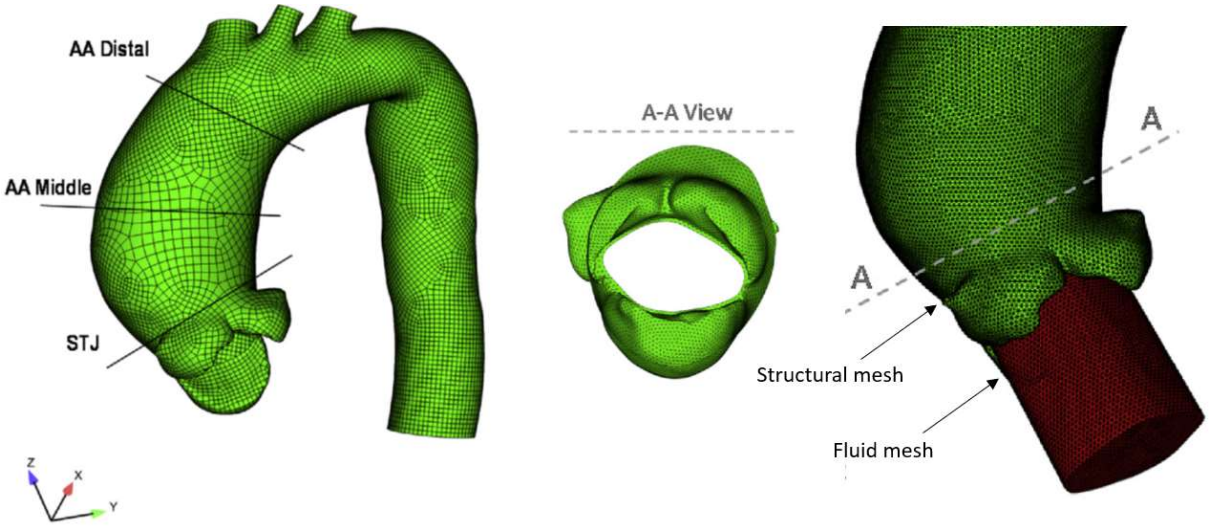

Figure 2.7. Representative FEA mesh (left) and CFD mesh (right) of a BAV patient from Mendez *et al.* work; labels on the FEA mesh (left) show 3 sections where computational variables were extrapolated.

The arterial wall was modelled as a fiber-reinforced soft tissue, using anisotropic and hyperelastic Holzaplef-Gasser-Ogden constitutive law [54]. Density was set equal to 1120 kg/m^3. The same mechanical characteristics and assumptions were used both for the 2-way FSI and the FEA.

Blood flow was assumed laminar, incompressible and Newtonian, with a density of 1060 kg/m^3 and a viscosity of 0.00371 Pa · s. The Pressure-Implicit with Splitting of Operators (PISO) and skewness correction scheme was adopted, since it is more robust for transient simulation of fluid flow. The same mechanical characteristics and assumptions were adopted both for the 2-way FSI and the CFD simulation.

2.4.2 Boundary conditions

Savabi *et al.* set as boundary condition for the fluid domain physiological flow rate waveform at the inlet surface according to literature, and physiological pressure waveform at the outlet surfaces, according to literature. **Figure 2.8** illustrates the boundary condition applied. Furthermore, the fluid obeys the no-slip boundary condition at the walls.

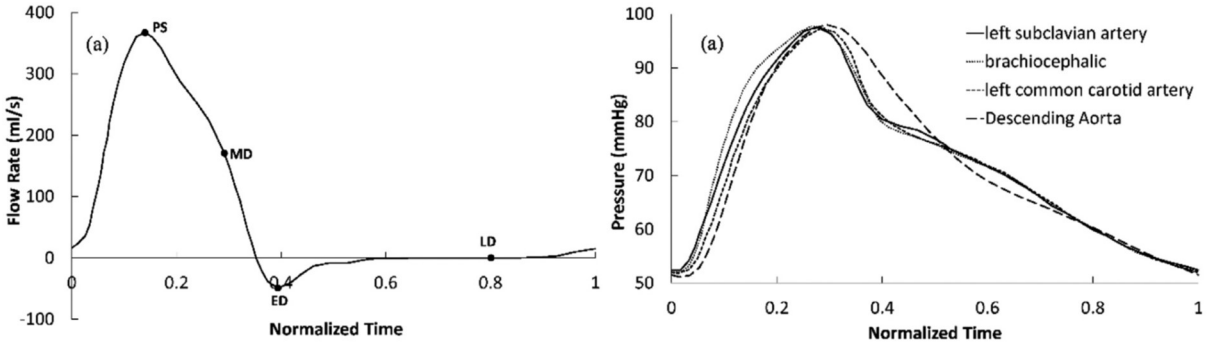

Figure 2.8. Physiological flow rate waveform applied at the inlet of the aortic arch (a) and pressure waveforms applied at each outlet.

Campobasso *et al.* simulations were performed coupling ANSYS Fluent v.17.2 and ANSYS Mechanical, using the System Coupling component available in the ANSYS package. Interaction between the two domains took place at the interface between blood and aortic wall: loads on the wall surface were transferred from Fluent to Mechanical, which in turn transferred back the mesh deformation to Fluent.

At the outlets of the structural domain, motion was impeded in all direction, while at the inlet radial deformation was allowed. The patient-specific time varying distribution of velocity magnitude on the inlet plane was obtained from the 4D flow from MRI and used as boundary condition. At the supra-aortic branches *in vivo* hemodynamic flow rate was prescribed and finally, at the descending aorta a three element Windkessel lumped parameter model was set to mimic the downstream impedance [38].

Mendez *et al.* used, as loading boundary condition in the FEA, the displacement field determined by the temporal tracking of the aortic luminal surface. The point cloud of the aortic luminal surface was reconstructed at diastolic and systolic phase. The relative displacement was evaluated as the Euclidean distance between the two configurations. FEA was solved in ABAQUS v.6.12 (Dassault System, Velizy-Villacoulblay, France).

In the CFD analysis, they used as inlet boundary condition a representative flow waveform, previously estimated by phase contrast magnetic resonance data. For each patient modeled in their study, the reference inlet waveform was scaled to match the transthoracic jet velocity measurement at systolic peak. Furthermore, the flow waveform was scaled in time, according to patient heart rate. Flow rate was applied at the inlet of an auxiliary conduct extruded from the

fluid domain with cross-section shaped as the orifice area of a BAV and a TAV patient (the auxiliary conduct is visible in the fluid mesh reported in **Figure 2.7**). At the outlets, resistance boundary conditions were set, using values from literature and adjusting them in order to match the flow distribution as expected in the aortic branches and in the descending aorta. Flow was solved in ANSYS Fluent v.14.0.

2-way FSI analysis was carried coupling ABAQUS v.6.12 and ANSYS Fluent v.14.0, using MpCCI v.4.2. In the coupling, Fluent sent fluid-induced wall forces to ABAQUS, that used them as loading condition to compute the deformation of the wall and then sent back to Fluent the deformed nodal coordinates. Aortic wall surface was used as boundary surface for the data exchange, which occurred every 0.0068 s. All the inlet and outlets boundaries were fixed in all direction in the structural domain. Boundary conditions for the fluid domain were set as in the CFD simulation [43].

2.4.3 Results

Savabi *et al*. observed the formation of regular streamlines along the aorta, that collapsed into vortical disturbed flow during diastole. Velocity contour reveled higher velocities at the inner line of the aortic arch, that moved to the other side in the descending aorta, due to the vessel curvature (**Figure 2.9**).

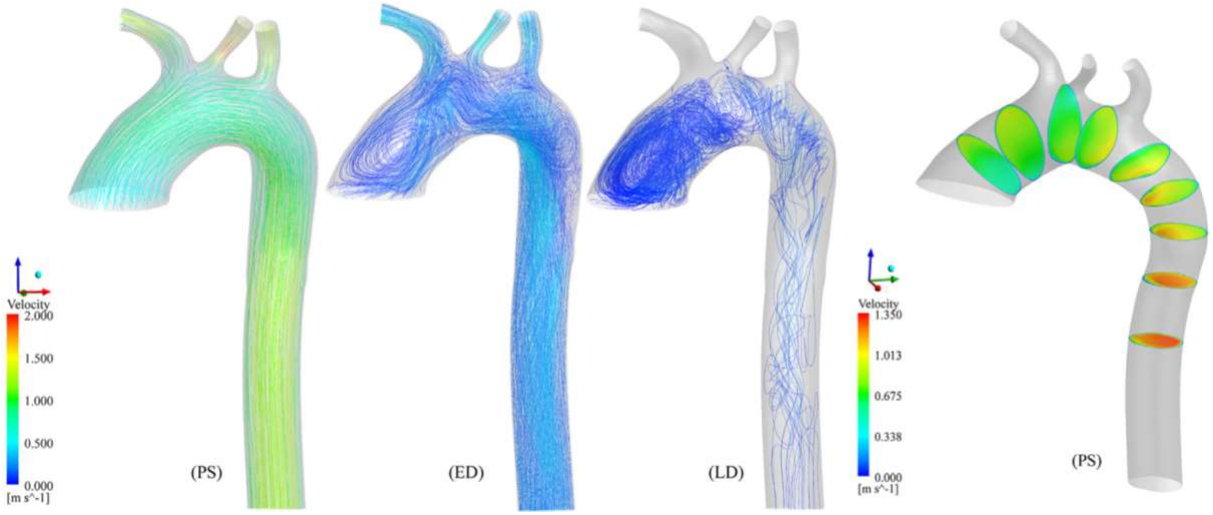

Figure 2.9. Streamlines at systolic peak (PS), early diastole (ED) and late diastole (LD). On the right, velocity contours on different cross-sectional plane along the aorta.

Higher WSS magnitude was obtained in the left common carotid (WSS > 30 Pa), due to the high-speed flow and velocity gradient entering the smallest supra-aortic branch. In the arch, an average value of 6-8 Pa was observed, while in descending aorta WSS reached values of 15 Pa. Von Mises stress varies from about 170 kPa at the inlet, to 100 kPa in the descending tract, consistently with pressure distribution. Higher displacements (2.5 mm) occurred in the regions that experienced high stresses. An intensification of stress (~200 kPa) was observed between the supra-aortic branches, where baroceptors are located. **Figure 2.10** shows the distribution of WSS and intramural stress.

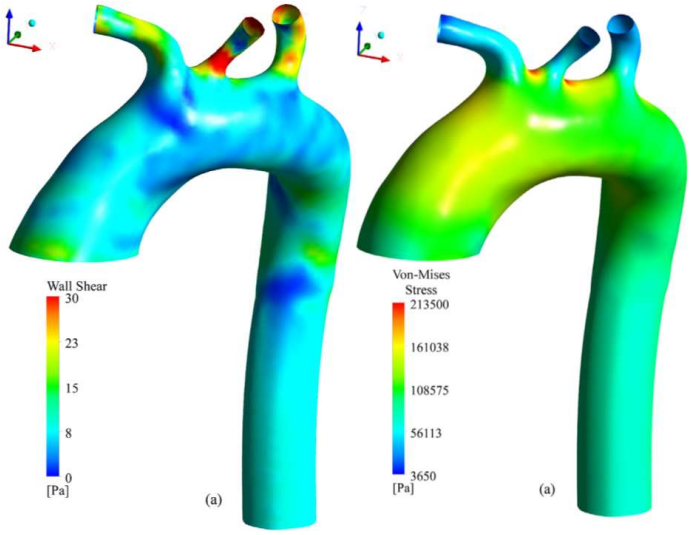

Figure 2.10. Wall shear stress distribution (on the left) and Von Mises intramural stress (on the right).

Temporal variation of blood pressure (**Figure 2.11**) and stretch in the position of baroceptor was also extracted to define normal operating condition and thus, a criterion to evaluate the functioning of baroceptors.

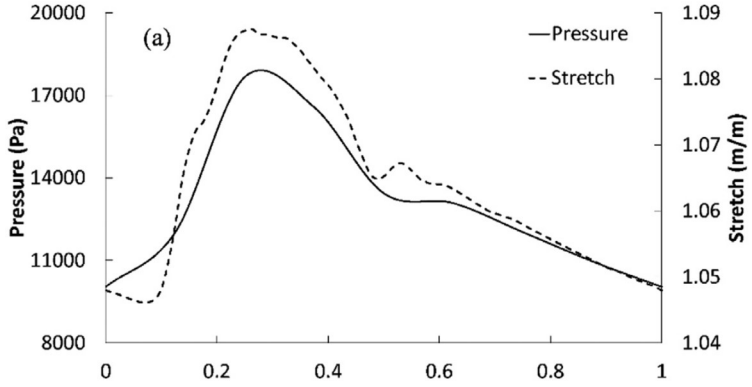

Figure 2.11. Pressure and stretch variation sensed by baroceptors in the aortic arch.

Campobasso *et al.* found similar pressure and WSS distributions when varying the downstream resistance, with the area of high pressure being in region of greater curvature of the aneurysm and high WSS area located in the anterior and posterior side of the aneurysm. The increasing of wall stiffness had a major impact: pressure was found to approximately 3 times higher, while WSS almost 7 times (**Figure 2.12**).

Their results suggest that patients with stiffer aTAA may reach very high peak wall stress in case of acute rise of peripheral resistance, whereas patients with a more compliant aTAA keep moderate stresses for similar rise of peripheral resistance. Therefore, the risk of rupture of an aTAA is significantly increased by the aTAA stiffening [38].

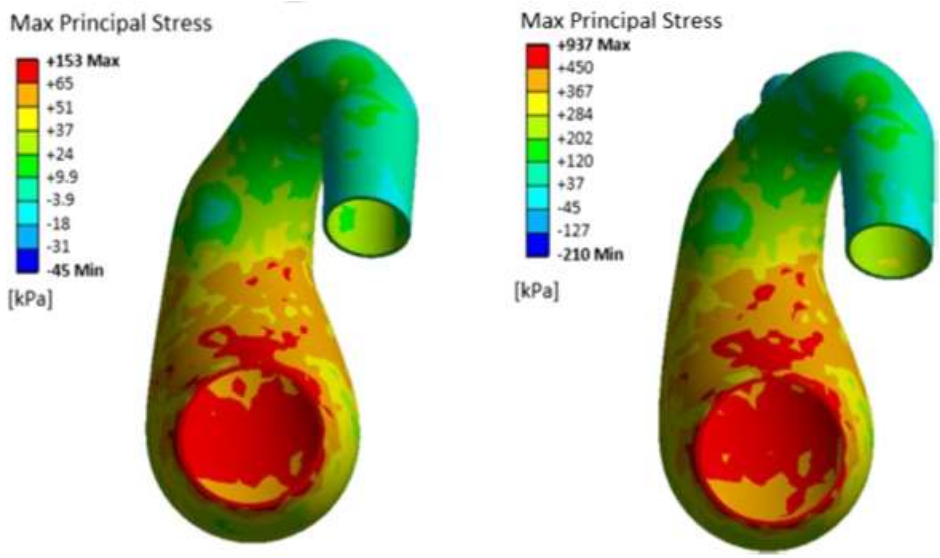

Figure 2.12. Wall stress distribution for two models using a Young modulus equal to 2 MPa (left) and 10 MPa (right). Maximum wall stress is equal to 153 kPa and 937 MPa respectively.

In Mendez *et al.* work the following hemodynamic and structural variables for each simulation were extrapolated at systolic peak and compared between FEA, CFD and 2-way FSI. Specifically, the intramural stress (IMS) in term of Von Mises stress was computed from FEA and FSI, the pressure index (PI), defined as 95% higher value of pressure normalize by the peak, the helical flow index (HFI), as a description of the complexity of the three dimensional flow field, and the WSS were computed in CFD and FSI analysis. All variables were measured at 3 different regions (shown in **Figure 2.7**) of the aorta: the sino-tubular junction, the mid-ascending aorta and the distal ascending aorta. Flow streamlines were found to be parallel, with minimal

deviance, to the initial direction of the aortic valve flow in tricuspid aortic valve patients and helical in the ascending aorta in bicuspid patients (**Figure 2.13**). The same patterns were found both in CFD and FSI analysis.

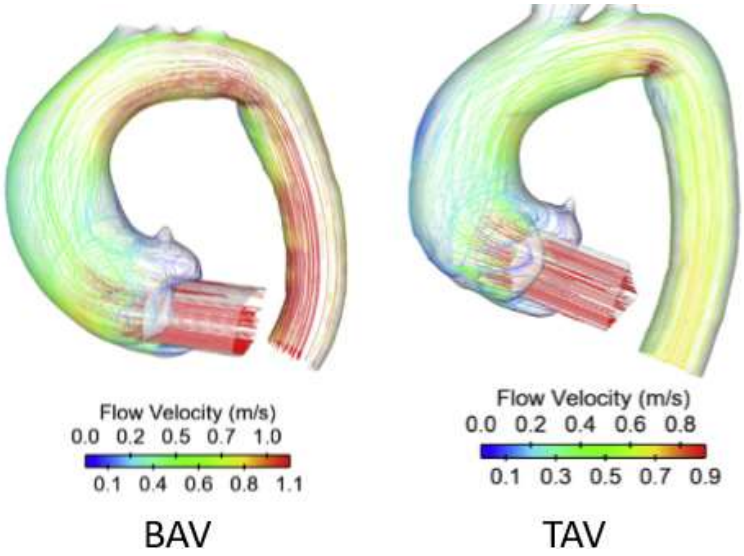

Figure 2.13. Flow patters at systolic peak in the aorta of a bicuspid aortic valve patient (left) and tricuspid aortic valve patient (right).

In CFD the region of higher WSS occurred in the greater curvature of the aTAA, increasing from the aortic valve to the mid-ascending aorta. Higher WSS regions were found in BAV patients. A comparison is shown in **Figure 2.14**. WSS computed with 2-way FSI resulted higher in the ascending aorta and similar in the descending tract. Abnormal helical flow patterns were found to be similar in CFD and FSI, in fact, values of the HFI are the same. Values of PI were statistically significant lower in the CFD than in 2-way FSI.

Therefore, Mendez *et al*. findings demonstrate that the stiff aneurysmal wall of patients with aTAA reduces the difference in WSS prediction between a less complex CFD and a deformable 2-way FSI [43].

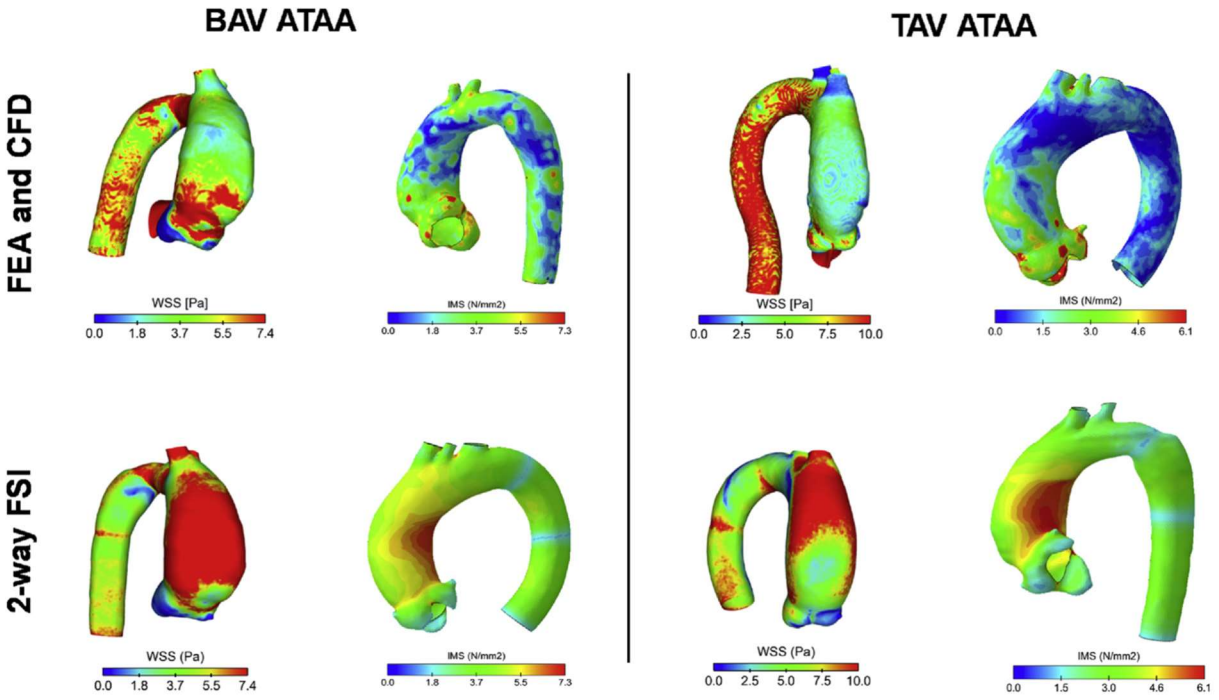

Figure 2.14. Comparison of wall shear stress and intramural stress distribution for a bicuspid aortic valve patient (left) and tricuspid aortic valve patient (right).

2.4.4 Conclusions

Some final consideration will be given on the three described studies. **Table 2.2** summarize some of their main features, while **Table 2.3** recaps the results accomplished.

Authors	Savabi *et al.* [52]	Mendez *et al.* [43]	Campobasso *et al.* [38]
Patient specific geometry	Arch-descending aorta	Aorta	Proximal aorta
Blood model	Newtonian	Newtonian	Carreau
Arterial wall model	Linear elastic	Hyperelastic	Linear elastic
Inlet BC	Physiological flow rate waveform	Patient specific-scaled flow rate waveform	Local velocity profile
Outlet BC	Physiological pressure waveform	3-elements Windkessel	Patient specific flow and 3-elements Windkessel

Table 2.2. Some features that summarize the three works analysis.

Authors	Savabi *et al.* [52]	Mendez *et al.* [43]	Campobasso *et al.* [38]
Output quantities (Fluid solver)	Velocity (streamlines and contours), pressure, WSS	Velocity (streamlines), pressure, WSS	Velocity (streamlines, and contours), pressure, WSS
Output quantities (Structural solver)	Von-Mises stress, displacement	Intramural stress, strain	Von-Mises stress
Postprocessing	Displacement → stretch at baroceptors location	Velocity → HFI, pressure → PI	Velocity → Validation against PC-MRI
Novelty aspect	Stretch as baroceptor functioning index	Comparison BAV v. TAV and FEA v. CFD v. FSI	Peak wall stress as aneurysm rupture risk

Table 2.3. Main results achieved from the three studies.

Savabi *et al.* model doesn't include the ascending aorta and aortic root tract. In that region, the hemodynamics may be complex, especially in patient with dilated aorta, and thus excluding that part form the geometry may lead to neglect some important fluid dynamics aspects. Campobasso *et al.* model presented instead a short descending aorta. This may cause altered results, especially in the descending tract, that may be influenced by the applied boundary condition (e.g. no displacement).

It is well known that arterial tissue has hyperelastic properties, however many studies in literature exploit for FSI simulation linear elastic models, that are less computational expensive and provide consistent results with FEA works that use hyperelastic models.

Using a flow rate waveform as inlet boundary condition – as in Savabi *et al.* and Mendez *et al.* works – is a simplified assumption, indeed the skewness of the inlet profile is not captured. Local velocity extracted from 4D flow on the inlet plane, as it was done in Campobasso *et al.* work is the best solution to reproduce the hemodynamic of a specific patient.

On the choice of outlet boundary condition, a study from Pirola *et al.* [39] proved that only the three element Windkessel boundary condition permits to reproduce a physiological like hemodynamics in the whole aorta, in terms of operating pressures, flow streamlines, blood velocity, formation of secondary flux etc.

The works reported from literature in the **Section 2.4.1-2.4.3** provided a deep insight into the FSI analysis and the interest that these models may have in clinical procedures. In particular, Medez *et al.* and Campobasso *et al.* focused their work on ascending thoracic aorta aneurysm patients, and the evaluation of parameters that may be predictive indexes of an acute event (e.g. aortic anseurysm rupture). Nevertheless, these studies focused only on the pre-operation: no aspect of the post-operation is investigated, such as the impact of the graft implantation on the hemodynamic, of these patients. To the best of author's knowledge, no 2-way FSI analysis has been conducted to compare the hemodynamics before and after elective surgery for aTAA patients. This set the basis for the current thesis work.

2.5 Aim of the thesis

The overview on the available FSI modeling approaches shows the potentialities of this numerical method. Several aspects of the aortic hemodynamics can be investigated exploiting FSI, accounting for the interaction between blood and the arterial wall, thus it can be used to study the alterations of flow after the reconstruction of the ascending aorta with a PET graft.
4D flow analysis, presented in **Section 1.6**, is a consolidated procedure used in clinical follow-up, but it just provides a measure of the hemodynamic quantities in the patient at the moment of the scanning. There is no predictive capability in this analysis method. Moreover, 4D flow has limited spatial resolution.
FSI models offer a useful tool with both good temporal and spatial resolution, that can be used to investigate and predict the hemodynamics in the aorta in different operating conditions (i.e. native vessel and reconstructed vessel). Results may offer a wide pool of cases to help physicians in clinical procedures, for example in the choice of the most suitable graft that causes less alteration in patient's hemodynamics after aortic reconstruction.
Previous studies [19][24], conducted using 4D flow analysis, highlighted alterations in velocity and WSS patterns, especially in the descending aorta. These alterations are suggested to be the possible cause of the starting of the atherogenic process, that leads to the reformation of TAA. Hence, particular attention will be paid to the descending aorta tract.
To the best of author's knowledge, a systematic comparison between the hemodynamics before and after aortic reconstruction has never been achieved with an FSI analysis. The aim of this

thesis work is to achieve a deep insight in the effects that the PET graft implantation causes in the patient's hemodynamics exploiting a patient specific FSI model. To consider alterations caused by the graft only, a patient who underwent elective surgery performed with VSR procedure will be considered.

Chapter 3
Materials and Methods

Chapter summary

In this chapter a description of the workflow adopted to develop the FSI models will be provided. In the first part, the geometry reconstruction and meshing are described, starting from MRI acquisition. In the second part, boundary conditions and material properties assignment are discussed. Finally, in the last part, the set-up adopted for the FSI simulations and for CFD is described.

3.1 Introduction

As described in **Section 1.5**, elective surgery for the treatment of aTAA is a safe procedure with positive outcomes (survival rate at 5 years >84%). The implantation of the PET graft is undoubtedly a life-saving procedure, but it carries some issues that may be dealt with using numerical models. One of this issue is the risk of formation of a TAA in descending tract of the aorta. To the best of author's knowledge, in literature there's no publication that exploits numerical models as a predictive tool to study fluid dynamic alterations induced by the graft. This set the basis for the current work.

FSI modeling allows to deep the fluid dynamics analysis of patient's aorta, taking into account the effect produced by the PET graft implanted after VSR surgical procedure. Focus was on a VSR treated patient, because alterations in hemodynamics are caused by the graft only, while in mCVG and bCVG reconstruction, a prosthetic valve is present too. If well-conditioned, this type of modeling may become a useful predictive tool to identify regions in the patient's vessel, where hemodynamics is significantly altered (e.g. in terms of WSS, blood velocities etc.), and consequently, the risk of the triggering of the atherogenic process for the development of TAA. The FSI model developed consist in two simulations of 2 cardiac cycle, one reproducing the pre-intervention conditions and the other reproducing the post-intervention. The workflow that was adopted is schematized in **Figure 3.1** and will be described step by step in this chapter. In parallel to the FSI model, a CFD model (2 cardiac cycle) was developed. CFD results will be compared with FSI results, to determine whether is possible or not to obtain similar results with a less expensive model.

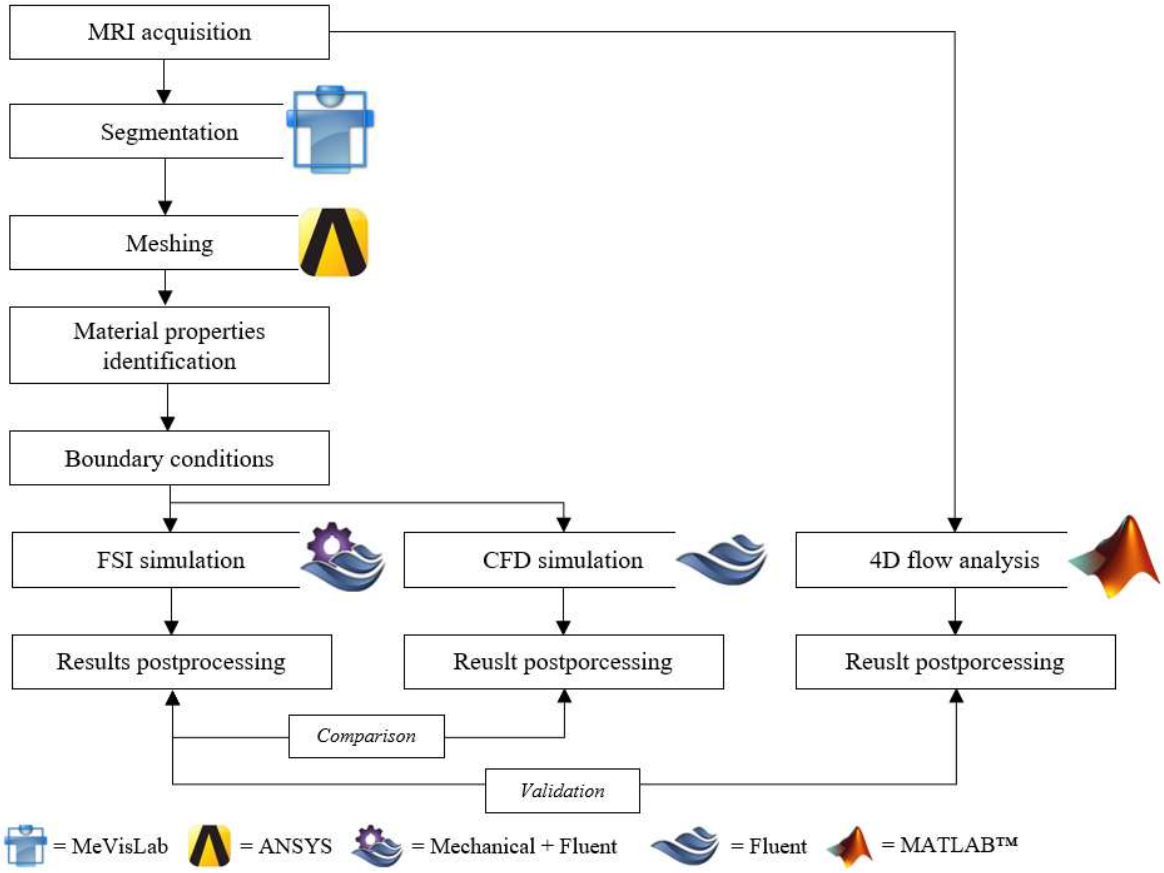

Figure 3.1. Workflow adopted for the realization of the model. Each step is described in the sections of this chapter.

3.2 Patient acquisition

One subject was chosen among a group of patients with aTAA, who underwent elective surgery for ascending aorta reconstruction at New York-Presbyterian Hospital (New York, NY). For those patients a pre-intervention MRI and a 6-months follow-up MRI were available. Aortic aneurysm, in the considered pool, had three different etiologies: medial degeneration (MD), bicuspid aortic valve (BAV) and Marfan syndrome (MFS). The chosen subject was a 48-years-old male patient, presenting a 50.5 mm diameter aTAA, developed due to medial degeneration who underwent valve sparing reconstruction elective surgery.

The reconstruction of the patient-specific geometry was based on MRI acquired images. Cardiac magnetic resonance was prospectively performed pre and post-operatively on a 3T GE SIGNA™ scanner (General Electric Co., Boston, MA, USA) using the same protocol in both the acquisitions. A contrast enhanced MR angiography was acquired to better analyze the

anatomy of the vessel with typical parameters of voxel size = 0.752 × 0.752 × 2 mm, field of view (FOV) = 380 mm, flip angle = 30°, repetition time (T_R) = 4 ms, echo time (T_E) = 1.56 ms. A respiratory compensated 4D flow phase contrast acquisition was then performed using a sagittal-oblique orientation. Spatial resolution was set to an isotropic value of 1.8 × 1.8 × 1.8 mm with a FOV = 360 mm, flip angle = 15°, $VENC$ = 150 cm/s, T_R = 4 ms, T_E = 2 ms. 4D flow images were post-processed with an in-house MATLAB™ (MathWorks Inc., Natick, MA, USA) code, developed by our research group.

A non-invasive central blood pressure (CBP) measurement was performed ~30 minutes prior to each MRI using a SphygmoCor CP system (AtCor Medical, Sydney, Australia). The system is based on radial applanation tonometry and is the most commonly used device for non-invasive estimation of CBP. The pressure values (systolic and diastolic) found with this measurement were used for the tuning of the outlet boundary conditions.

3.3 Patient specific anatomy reconstruction

The segmentation of the aorta and the three supra-aortic branches, before and after surgery, was performed on MR angiography (MRA), for a better resolution. Images were segmented in MeVisLab 2.7.1 (MeVis Medical Solutions AG, Fraunhofer MEVIS) visualization tool (**Figure 3.1**).

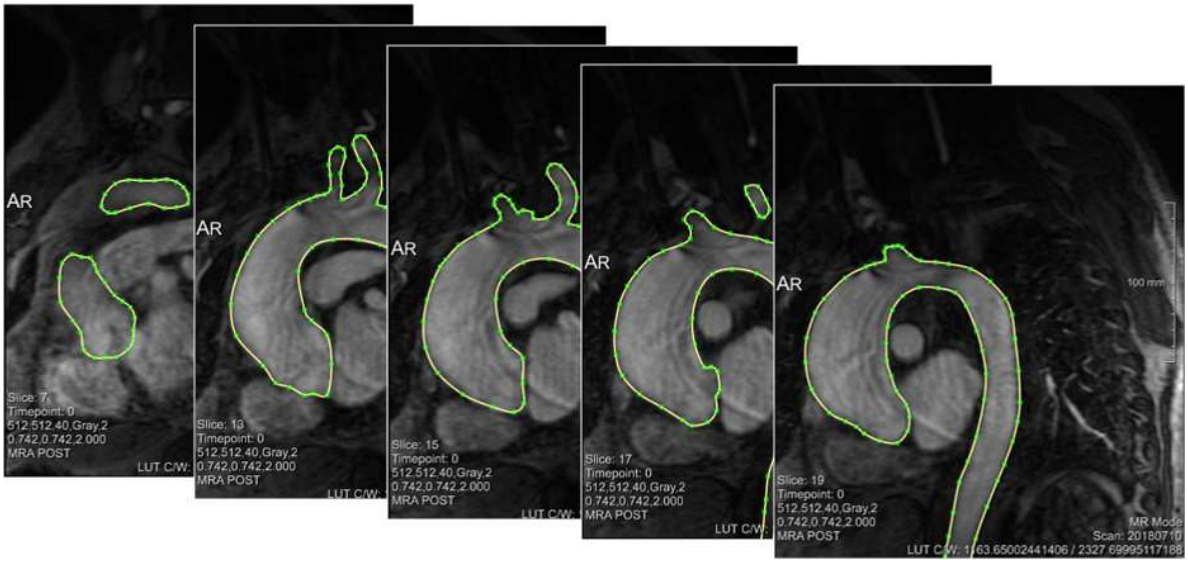

Figure 3.2. Segmentation of the aorta before graft replacement. The region of interest (ROI) was defined at systolic peak, performing segmentation on each slice.

Pathological geometry

The reconstructed geometry (**Figure 3.2a**) was saved as an STL file and exported to Meshmixer (Autodesk Inc., San Rafael, CA, USA). A shape preserving smoothing filter was applied to obtain a more regular outer surface, with the following parameters (proper of the Meshmixer algorithm): smoothing = 1, smoothing scale = 5, constraint rings = 3; then the diameter of the aneurysm in the reconstructed smoothed geometry was ensured to be the same as in clinal measurements from imaging (50.5 mm). The inlet and outlet surfaces for blood flow were created with a plane cut. The geometry was cut at the level of the sinotubular junction to obtain the inlet of the fluid domain, at the level of the abdominal aorta and at the root of the three supra-aortic branches to generate the outlets. The BCA, LCCA and LSA were then extruded in normal direction by 40 mm (~5 diameters). This was done to reduce the effect of outlet boundary conditions on the fluid dynamics in the aorta. Finally, the geometry (**Figure 3.2b**) was remeshed, to remove and adjust faces with very high skewness and aspect ratio.

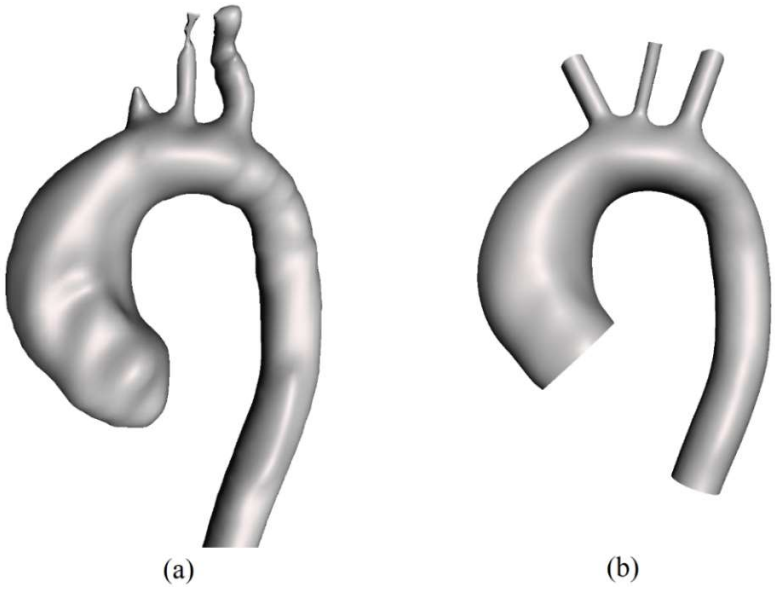

Figure 3.3. The pre-intervention 3D geometry of the fluid domain reconstructed from MeVisLab (a) and then smoothed and cut in Meshmixer (b).

An in-house MATLAB™ code was used to generate a fictious MRA acquisition (PC-MRA), from the PC-MRI dataset. The STL was then manually co-registered (**Figure 3.3**) to the PC-MRA data in ParaView 5.7.0 (Sandia National Laboratories, Kitware Inc., Los Alamos National

Laboratory). Co-registration was performed both for post-processing purpose, to compare 4D-flow data with FSI and CFD results, and to obtain patient specific inlet boundary conditions.

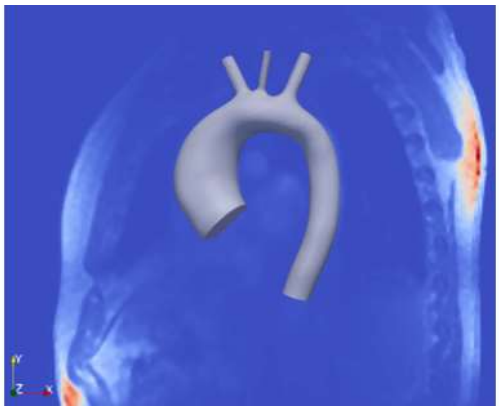

Figure 3.4. Co-registration performed in Paraview on PC-MRA data of the pre-intervention STL model.

Once co-registered, the STL file was imported back to Meshmixer. The solid domain (i.e. the aortic wall) was created by extruding the outer surface of the fluid domain in normal direction by a constant value of 2 mm. The thickness of the human aortic wall is not constant, especially in aTAAs, where it can vary by 0.7 mm from the anterior to the posterior side. The chosen value, 2 mm, is an average value between the thickness of an healthy aorta and the typical thickness of thoracic aneurysms [55][56]. Finally, the 3D geometry (**Figure 3.4**) of the aortic wall was locally remeshed to remove very sharp angles generated by the extrusion (e.g. between the roots of the supra-aortic branches).

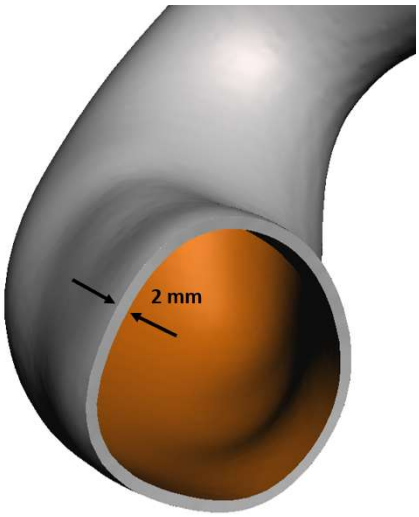

Figure 3.5. Pre-intervention aortic wall model (zoomed in of the aortic inlet). Highlighted in orange it's showed the inner surface, that is the interface where the fluid-solid interaction takes place.

Post-intervention geometry

The reconstruction of the post-intervention model followed the same process designed for the pre-intervention geometry. The STL was reconstructed from MRA images that were segmented in MeVisLab, then smoothed and adjusted in Meshmixer to create the inlet and the outlets surfaces. Co-registration in Paraview on PC-MRA data was performed and finally the preliminary solid domain was obtained extruding the fluid domain outer surface by a constant value of 2 mm.

For the post-intervention geometry, a further step was necessary to have a solid domain composed by the PET graft and the native aortic wall as two distinct parts. Hence, the geometry obtained (previously co-registered) by extrusion was imported in Paraview together with the DICOM images from MRA. From angiography images, the suture site of the graft is clearly visible (**Figure 3.5a**), so the ascending aorta was sliced with a plane (**Figure 3.5c**) that was manually aligned to the suture site.

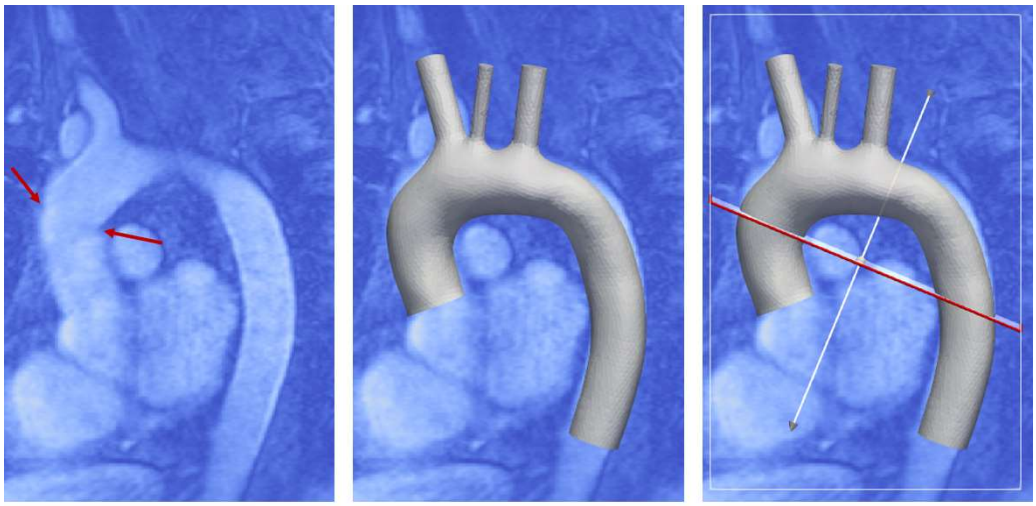

Figure 3.6. Figure shows MRA images where suture site is highlighted by the red arrows (a) and the STL geometry co-registered (b). The slicing plane is showed in (c).

3.4 Meshing

Once the geometry was reconstructed, adjusted and co-registered with the PC-MRA, it was imported in ANSYS Meshing (ANSYS Inc., Canonsburg, PA, USA) embedded tool, to generate the computational grid. In this section, the generation of the mesh of the fluid domain of the pre-

intervention model will be described. The same procedure was adopted to generate the mesh of the post-intervention model.

3.4.1 Sensitivity analysis

The fluid domain model was imported and meshed in ANSYS Meshing embedded tool. Three meshes, consisting of ~1.45 (coarse), ~2.7 (medium), ~5.8 (fine) millions of tetrahedral elements, were generated to perform a sensitivity analysis. A transient flow simulation was run for each mesh, imposing the average velocity at the inlet and zero pressure at the four outlets. Maximum velocity on a transverse plane in the descending aorta tract was chosen as parameter of grid convergence (f_i). The grid convergence index (GCI) was calculated for the fine-to-medium and medium-to-coarse mesh [57][58]. GCI is a measure of the difference between the variable of interest (i.e. maximum velocity in descending aorta) and its asymptotical value, it provides an estimation of how much that variable would change with a finer mesh.
Let's indicate the fine, medium and coarse mesh with the subscript 1, 2 and 3 respectively. The numbers of elements N_1, N_2 and N_3 satisfy the following relationship:

$$r \approx \left(\frac{N_1}{N_2}\right)^{\frac{1}{3}} \approx \left(\frac{N_2}{N_3}\right)^{\frac{1}{3}} \tag{3.1}$$

The GCIs fine-to-medium and medium-to-coarse were calculated as:

$$p = \frac{\ln\left(\frac{f_3 - f_2}{f_2 - f_1}\right)}{\ln(r)} \tag{3.2}$$

$$E_1 = \frac{f_2 - f_1}{f_1(r^p - 1)}, \qquad E_2 = \frac{f_3 - f_2}{f_2(r^p - 1)} \tag{3.3}$$

$$GCI_{1,2} = F_s \cdot |E_1|, \qquad GCI_{2,3} = F_s \cdot |E_2| \tag{3.4}$$

Where F_s is a safety factor, chosen equal to 1.25 [57]. To ensure that the meshes are in the asymptotic range of convergence, the ratio k defined in **Equation 3.5** must be close to 1 [58].

$$k = \frac{1}{r^p} \cdot \frac{GCI_{2,3}}{GCI_{1,2}} \tag{3.5}$$

3.4.2 Mesh quality metrics

A good quality of the mesh is fundamental for the stability of the simulation. To evaluate mesh quality, aspect ratio, skewness and orthogonal quality of the elements were considered as mesh metric parameters. *Aspect ratio* is the ratio between the longest and the shortest side of the element and should be ideally equal to 1, but values lower than 18-20 still ensure reliable results [59]. The element *skewness* measures the deviation from the optimal element size, computation was based on equilateral volume (**Figure 3.7a**). Skewness is optimal when lower than 0.2 and unacceptable when greater than 0.85. *Orthogonal quality* relates to how close angles between adjacent element faces are to some optimal angle that depends on the topology. It is unacceptable if lower than 0.1 and optimal when greater than 0.7. Orthogonal quality is measured as:

$$\min\left(\frac{\vec{A}_i \cdot \vec{f}_i}{|\vec{A}_i||\vec{f}_i|}, \frac{\vec{A}_i \cdot \vec{c}_i}{|\vec{A}_i||\vec{c}_i|}\right) \tag{3.6}$$

Where $\vec{A}$ is the face normal vector, $\vec{f}$ is a vector that connect cell center and face center and $\vec{c}$ is a vector connecting the centers of two adjacent cells (**Figure 3.7b**) [59].

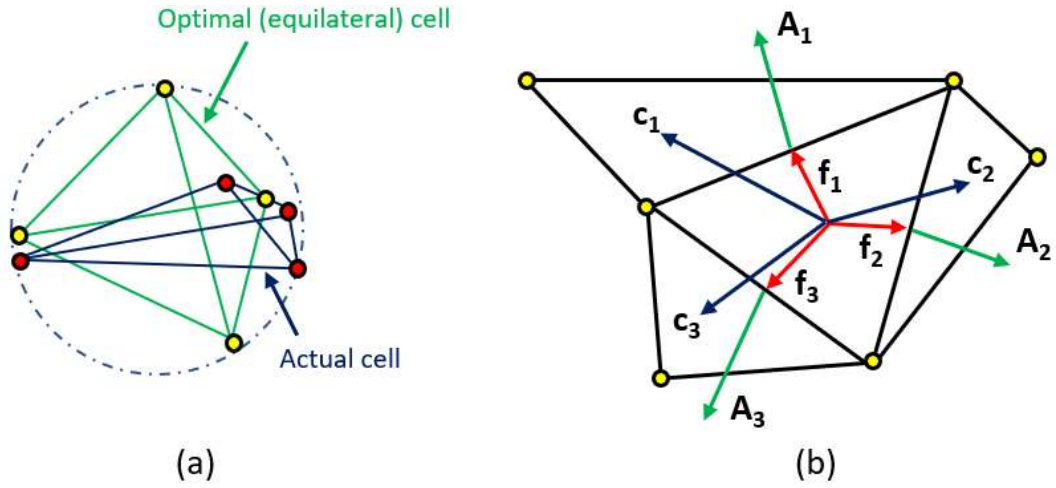

Figure 3.7. Comparison of an optimal (skewness = 0) and the actual cell of the mesh (a), and parameters used to compute orthogonal quality (b).

3.4.3 Dynamic meshing

In FSI simulations, since the aortic wall moves due to the pressure applied by blood, a dynamic meshing is required for the fluid model. The software exploited to solve the fluid domain, ANSYS Fluent (ANSYS Inc., Canonsburg, PA, USA), offers three different dynamic mesh schemes: smoothing, layering and remeshing method, that can be used both individually and at the same time. Combining these schemes, it is possible to tackle more complex dynamic mesh problems.

A combination of the smoothing and remeshing scheme was adopted for the fluid model. The smoothing-based remeshing scheme is commonly used for triangle or tetrahedral elements. It is combined with the remeshing-based method when the expected displacement of the boundary is larger than the element size [59].

Mesh smoothing can be done with different methods in ANSYS Fluent, the spring-based one was adopted. The sides of each element, connecting to generic nodes i and j, are treated as ideal spring (**Figure 3.8**). The force applied on the i-th element is given by:

$$\bar{\boldsymbol{F}}_i = \sum_j^{n_i} k_{ij}\left(\Delta\bar{\mathbf{x}}_j - \Delta\bar{\mathbf{x}}_i\right) \tag{3.7}$$

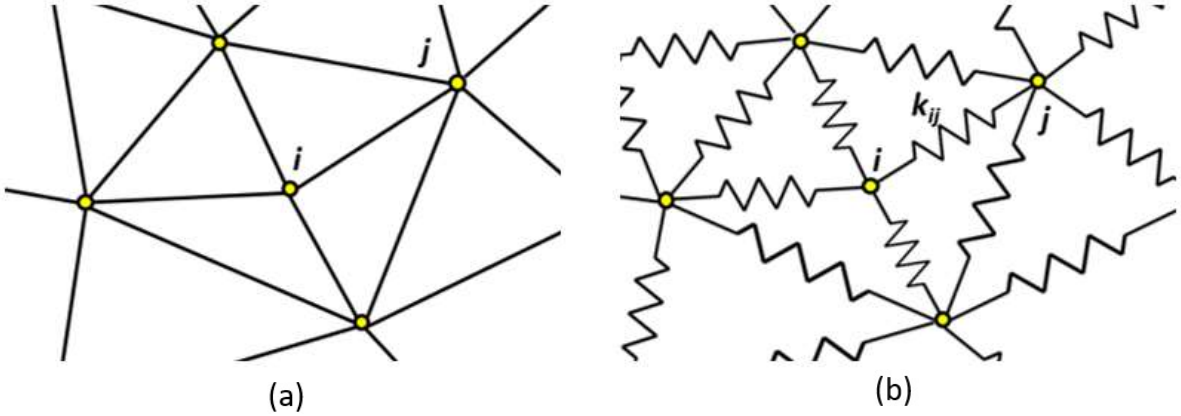

Figure 3.8. Example discretization of a domain with a static mesh (a) and a dynamic mesh (b), exploiting spring-based smoothing method.

Where n_i is the number of neighboring nodes j, k_{ij} is the stiffness of the spring (that can be set in the simulation) and $\Delta\bar{\mathbf{x}}_i$ and $\Delta\bar{\mathbf{x}}_j$ are the nodal displacements. At equilibrium, the force on each node must be null, so the i-th displacement at next time step is given by:

$$\Delta\bar{\mathbf{x}}_i^{n+1} = \frac{\sum_j^{n_i} k_{ij}\Delta\bar{\mathbf{x}}_i^n}{\sum_j^{n_i} k_{ij}} \tag{3.8}$$

Displacements are known at the boundaries, so **Equation 3.8** can be solved with the Jacobi sweep method [60] for interior node. At convergence, the position of the i-th node is updated such that:

$$\bar{\mathbf{x}}_i^{n+1} = \bar{\mathbf{x}}_i^n + \Delta\bar{\mathbf{x}}_i^{n,(converged)} \tag{3.9}$$

As for the smoothing scheme, ANSYS Fluent includes several remeshing methods: local remeshing, face region remeshing and local face region remeshing were used in the FSI simulations. Cells with skewness greater than the maximum specified are marked for remeshing. **Figure 3.9** shows the effect of smoothing and remeshing scheme [59].

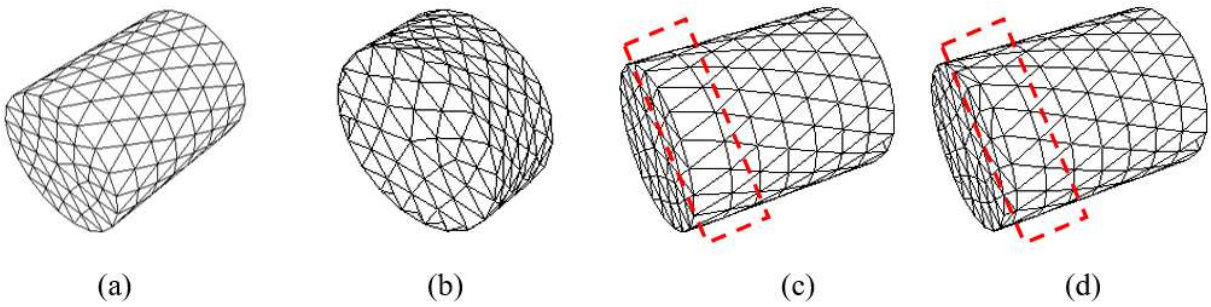

Figure 3.9. Effects of the remeshing schemes on an example mesh (a). In this example after a compression (b) the smoothing scheme is applied, after a stretching (c) excessively deformed cells are marked for remeshing (c) and a new mesh is generated (d) with the remeshing scheme.

A spring stiffness $k_{ij} = 0.1$ was set for the smoothing scheme. Remeshing scheme was set with the following parameters as criteria to mark cell and faces for remeshing: maximum length scale = 1.5 mm, minimum length scale = 0.5 mm, maximum cell skewness = 0.85 and maximum face skewness = 0.8.

3.5 Material properties

In this FSI analysis, three materials interact: the fluid (i.e. blood), the arterial wall and the PET graft. Their mechanical characteristics are herein provided and summarized in **Table 3.2**.

Blood

At 37° C, blood density ϱ is defined as the weighted average between the density of plasma and the corpuscular part of blood. The average value for human is $\varrho = 1060$ kg/m^3 [61].
In the aorta high shear rate occurs (above 100 s^{-1}), so blood can be considered a Newtonian fluid with constant dynamic viscosity [1]. Values for human blood dynamic viscosity range between $\mu = 3.5$ and $\mu = 5$ cP, hence a value of $\mu = 4$ cP was adopted [62]. The flow was assumed to be incompressible and laminar (in the aorta, typical Reynolds number is $\mathscr{R}e = 867$ and flow is laminar below $\mathscr{R}e = 2000$) [52].

Arterial wall

The wall of the vessels was modeled as isotropic linear elastic, basing on the assumption small-deformation regime throughout a cardiac cycle, with a Young's modulus $E = 1.5$ MPa, a Poisson ratio $\nu = 0.4$, a density $\varrho = 1120$ kg/m^3 [63] and a constant thickness equal to 2 mm. Many works from literature shows that aortic tissue has an hyperelastic behavior [64][65][66], however, most of the FSI work in literature exploit a linear elastic model (**Section 2.4**).

Polyethylene-terephthalete (PET) graft

PET was modeled as an isotropic linear elastic material, with a Young's modulus $E = 11.84$ MPa and a Poisson ratio $\nu = 0.3$. These values were obtained fitting experimental stress-strain curves from equi-biaxial tests on PET samples. Only data for the circumferential direction beyond the toe region of the stress-strain curve were considered. The PET density was set equal to 600 kg/m^3 [67].

	Blood	**Ascending aorta tract**	**Aortic arch, branches and descending tract**
Pre-intervention	$\varrho = 1060$ kg/m^3 $\mu = 0.004$ Pa · s	$\varrho = 1120$ kg/m^3 $E = 1.5$ MPa $\nu = 0.4$	
Post-intervention	$\varrho = 1060$ kg/m^3 $\mu = 0.004$ Pa · s	$\varrho = 600$ kg/m^3 $E = 11.84$ MPa $\nu = 0.3$	$\varrho = 1120$ kg/m^3 $E = 1.5$ MPa $\nu = 0.4$

Table 3.2. Mechanical properties of the interacting entities of the model. ϱ = density, μ = dynamic viscosity, E = Young's modulus, ν = Poisson's ratio.

3.6 Boundary conditions

Boundary conditions applied to the structural and to the fluid domain are herein discussed.

3.5.1 Structural domain

At the inner surface of the solid domain a fluid-solid interface applied was set as load condition. The fluid pressure distribution over the boundary, derived by the solution of the fluid domain is applied to the solid domain as a loading condition.

Boundary conditions were assigned at every inlet and outlet such that $\bar{\boldsymbol{u}} = 0$ (no displacement allowed). Boundary conditions are summarized in **Figure 3.10**.

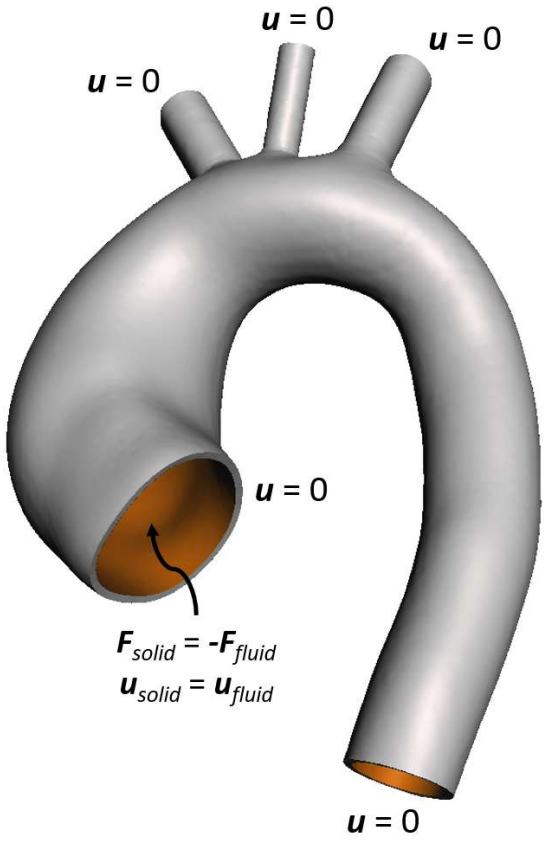

Figure 3.10. Solid domain of the pre-intervention model and applied kinematic and loading boundary conditions. Fixed boundaries were set at the inlet and the outlets of the model, fluid-solid interaction loading boundary condition was set at the inner surface of the aortic wall.

3.5.2 Fluid domain

Inlet boundary condition

Aortic hemodynamics can be very complex in the ascending tract, especially for aTAA patients, for which blood flow generally presents vortical structures. Thus, flat velocity inlet profile and idealized parabolic profile result to be oversimplified, since tangential components of velocity are neglected.

A patient-specific velocity inlet boundary condition, obtained with an already implemented in-house MATLAB™ code, was set for the two models. The inlet plane was extracted from the STL model, previously co-registered to PC-MRA, and imported in MATLAB™. Velocity data from 4D flow were interpolated on the inlet nodes (through Gaussian interpolation) for each time frame (20 time-frames overall) and up-sampled with a Fourier interpolation setting a $\Delta t = 0.001$ s, the same used for time discretization in the simulations. Velocity components were converted from the patient reference frame (anterior-posterior, left-right and foot-head velocity) to the global reference system of the STL model (v_x, v_y, v_z) and saved in a .csv (comma separated values) file.

A MATLAB™ code was implemented to convert the .csv file to a set of .prof (profile) files, each one containing the coordinates of the inlet nodes and the corresponding values of v_x, v_y, v_z at a time step. The .prof files were read in ANSYS Fluent and set as inlet boundary condition. The code workflow is schematized in **Figure 3.11**.

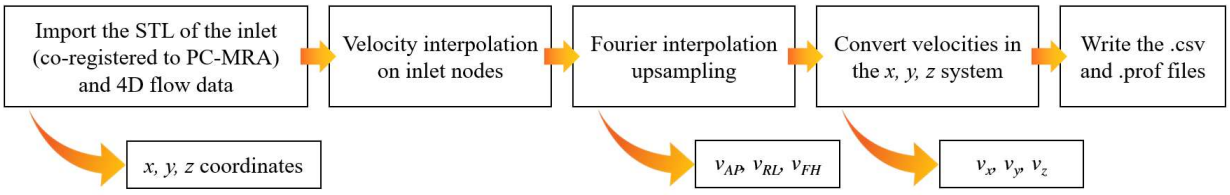

Figure 3.11. MATLAB™ code workflow schematized on the left, and corresponding output variables of interest at each step on the right.

Figure 3.12 illustrates the resulting inlet velocity profile (for the pre-intervention model) at different time instant of the cardiac cycle. The resulting flow rate is showed in **Figure 3.13** for the pre-intervention and post-intervention case.

To make the simulations reach a converged cyclic solution two cardiac cycle were required and results from the last one only were considered.

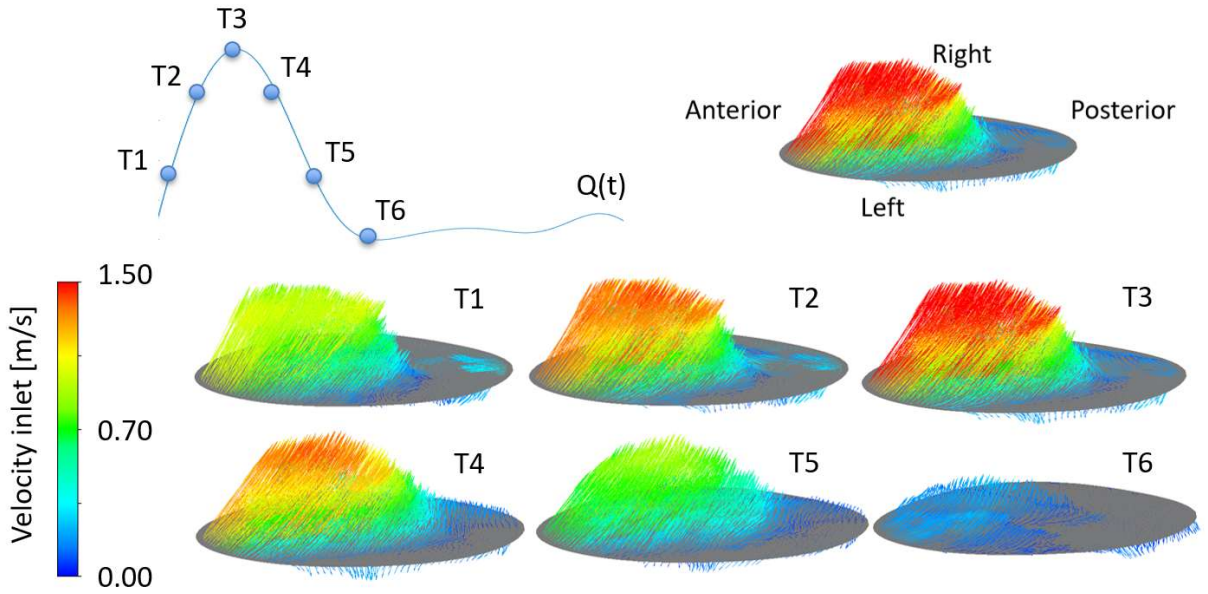

Figure 3.12. Inlet velocity profile at different time instant during the cardiac cycle. Figure highlight the skewness of the profile; higher velocities are located at the extrados of the ascending aorta, on the anterior side.

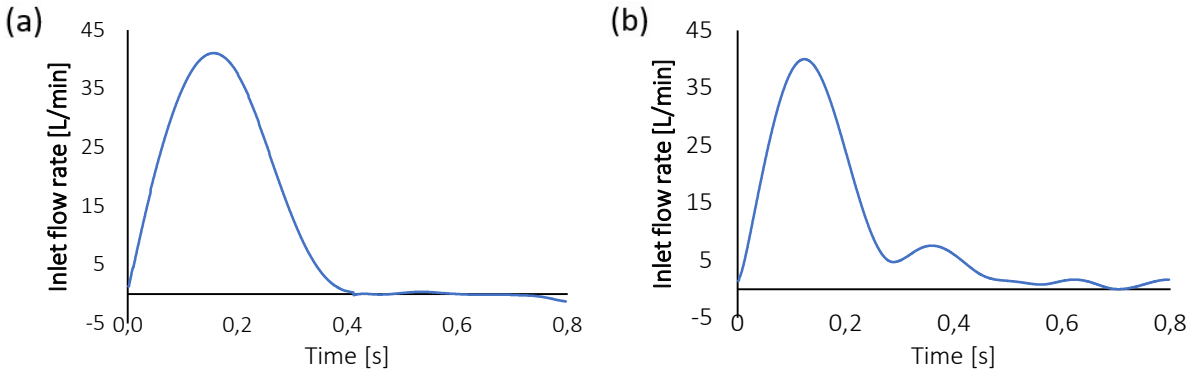

Figure 3.13. Inlet flow rate resulting from the velocity profiles applied. Pre-intervention (left) and post (right).

Outlet boundary conditions

To reproduce the systemic impedance, downstream the aortic branches and the descending aorta, 3-elements Windkessel (WK3) models were adopted. Windkessel boundary conditions were set through an available extension in the ANSYS Customization Toolkit (ACT).

The WK3 is a lumped parameter model, that consists in a proximal (or characteristic) resistance Z, a capacitor C and a distal resistance R (**Figure 3.14**). It is a zero-dimensional network in

which, instead of assigning the geometrical and physical features of a branch, its resistance, capacitance and inductance are set. The WK3 model achieves the dynamic description of the downstream vascular system physics, neglecting the spatial variation of the variables that describe it. The model is described by a set of ordinary differential equations, that assume uniform distribution of the variables (e.g. pressure, blood flow rate) within any compartment of the cardiovascular system at any instant in time.

According to [39], Windkessel boundary conditions are the best option to correctly reproduce the hemodynamics of a patient.

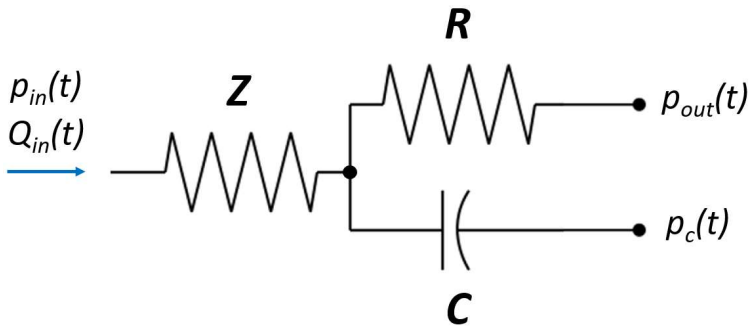

Figure 3.14. Schematic representation of a WK3 model. The LPM is coupled with the 3D fluid domain in correspondence of the proximal resistance Z. The average flow rate q_{in} is computed from the 3D model, then the corresponding inlet pressure (i.e. the outlet pressure of the 3D domain) is computed solving an ordinary differential equation and transmitted back to the fluid domain.

Conservation of mass in the WK3 model is expressed by the following equation:

$$Q_{in} = C\frac{\partial}{\partial t}(p_{in} - Q_{in}Z - p_c) + \frac{p_{in} - Q_{in}Z - p_{out}}{R} \tag{3.10}$$

For each branch, the ZCR parameters were computed with the following equations from literature [68][69][49][70]:

$$R_{tot} = Z + R = \bar{P}/\bar{Q} \tag{3.11}$$

$$Z = \rho\frac{PWV}{A} \tag{3.12}$$

$$PWV = a_2/(2r)^{b_2} \tag{3.13}$$

$$C = \tau / R_{tot} \tag{3.14}$$

Where $\bar{P}$ and $\bar{Q}$ are the mean pressure and flow rate respectively, ρ is blood density, PWV the pulse wave velocity, A the area of the vessel cross-section, a_2 and b_2 are two constant equal to 13.3 and 0.3 respectively, r is the vessel radius and τ is the time constant of the exponential fall in diastole.

The mean pressure $\bar{P}$ used was the same for all the outlets: the average value of the systolic (SP) and diastolic pressure (DP) measured before the scanning. Prospective measures performed prior and after the surgery of the inlet average flow rate (at the level of the aortic valve) were available, corresponding to 7.09 and 7.68 l/min pre and post operation respectively. The average flow rate through each outlet was obtained multiplying the previous values by different fractions, based on measurements of the splitting of the flow available in literature [39]. For the descending aorta (DAO), aortic average flow rate was multiplied by 0.7, for the BCA by 0.15, for the LCCA by 0.07 and for the LSA by 0.08. To compute the pulse wave velocity PWV, the vessel radius is required. Since the outlets of the model weren't circular, a fictious radius was computed:

$$r^* = \sqrt{A/\pi} \tag{3.15}$$

The value of the area A was computed from ANSYS geometry editor for each outlet surface. A value of $\tau = 1.79$ s was set, according to [49].

Equation 3.10 was discretized with second-order upwind scheme and solved for 3 cardiac cycle in Microsoft Excel (Microsoft Corporation, Redmond, WA, USA). ZCR values from **Equation 3.11-14** were set.

Outlet	***Z***	***C***	***R***
BCA	5.39×10^{7}	2.14×10^{-9}	7.62×10^{8}
LCCA	1.35×10^{8}	1.00×10^{-9}	1.61×10^{9}
LSA	5.68×10^{7}	1.14×10^{-9}	1.47×10^{9}
DAO	1.08×10^{7}	1.00×10^{-8}	1.64×10^{8}

Outlet	***Z***	***C***	***R***
BCA	3.33×10^{7}	3.23×10^{-9}	5.08×10^{8}
LCCA	1.14×10^{8}	1.51×10^{-9}	1.05×10^{9}
LSA	5.29×10^{7}	1.72×10^{-9}	9.63×10^{8}
DAO	1.04×10^{7}	1.51×10^{-8}	1.06×10^{8}

Table 3.3. Used values of the ***RCR*** Windkessel model for the pre (left) and post-operation (right) model. ***Z*** = proximal resistance, ***C*** = compliance, ***R*** = peripheral resistance. Values are given in S.I. units, Pa·s/m^3 for resistances and m^3/Pa for compliances.

Excel Solver was then used to minimize the difference between the DP-SP values measured in the patient and the corresponding pressures obtained by the solution of **Equation 3.10**, varying the ZCR parameters. The final values are reported in **Table 3.3**.

The boundary condition applied to the fluid domain are summarized by the scheme shown in **Figure 3.15**.

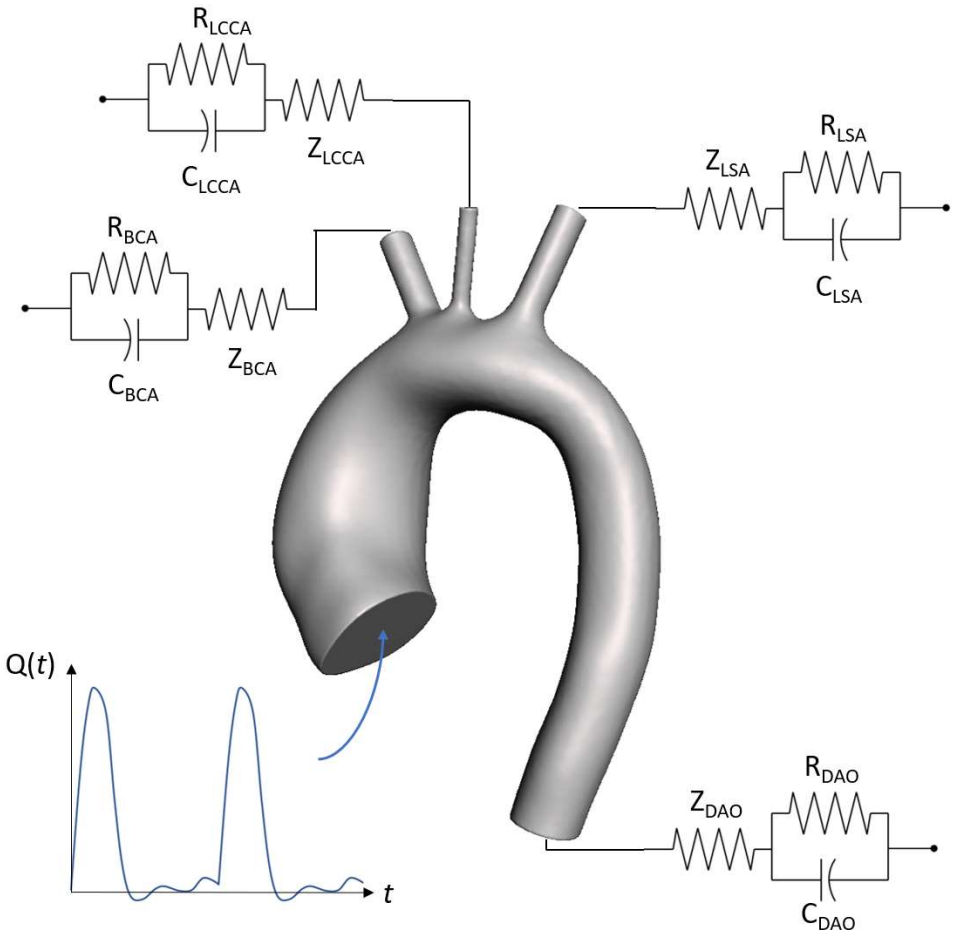

Figure 3.15. Fluid domain of the pre-intervention model and applied boundary condition. Velocity profiles were applied to the inlet (resulting in patient-specific aortic flow rate) and Windkessel boundary conditions (RCR model) at the outlet.

Wall boundary condition

On the wall of the fluid domain, the no-slip boundary condition was applied, therefore the velocity of the fluid is null there.

3.7 FSI numerical solution

FSI analysis was run in ANSYS v.17.2 (ANSYS Inc., Canonsburg, PA, USA), coupling the structural solver – ANSYS Mechanical v.17.2 – and the fluid solver – ANSYS Fluent v.17.2 – using the System Coupling module provided in ANSYS workbench. Simulations of two cardiac cycle took an average of 10 days running on 24 cores on a cluster server with Intel® Xeon® CPU X5670 at 2.93 GHz processor for a total of 192 Gb RAM. Only solution from the last cycle was considered.

3.7.1 Solvers coupling

The System Coupling module was used to control the execution of the fluid and solid simulations. Each time step resulted sub-divided into coupling interactions and for each coupling iteration the data transfer between the two solvers took place. At the interface between the two domains, blood pressure was transferred to the solid domain, then the wall displacement, consequently computed, was transferred back to fluid domain to perform the remeshing (basing on the criteria defined in **Section 3.4.3**). The coupling iterations were repeated until convergence was reached, or a new time step was run. A maximum root-mean-square (RMS) residual of 0.01 was set as convergence criteria, both for the fluid and solid solver. The RMS is a measure of the change in the data transfer between two successive iterations within or across a given coupled step and it is defined as:

$$\mathrm{RMS} = \sqrt{\left(\widehat{\Delta X}\right)^2} \tag{3.16}$$

$$\widehat{\Delta X} = \frac{2\Delta X}{\left[(\max|\varphi| - \min|\varphi|) + \left|\bar{\varphi}\right|\right]} \tag{3.17}$$

Where ΔX is the change in data transfer of a generic quantity X, while φ and $\bar{\varphi}$ are the absolute and mean value of the transferred physical quantity [71]. A maximum number of 10 coupling iterations per time step was used for both simulations.

To enhance the solution stability and convergence, an under-relaxation factor (URF) equal to 0.3 was set for the transfer of the pressure load from ANSYS Fluent to ANSYS Mechanical.

A scheme of the fluid-structure coupling interaction is provided in **Figure 3.16**.

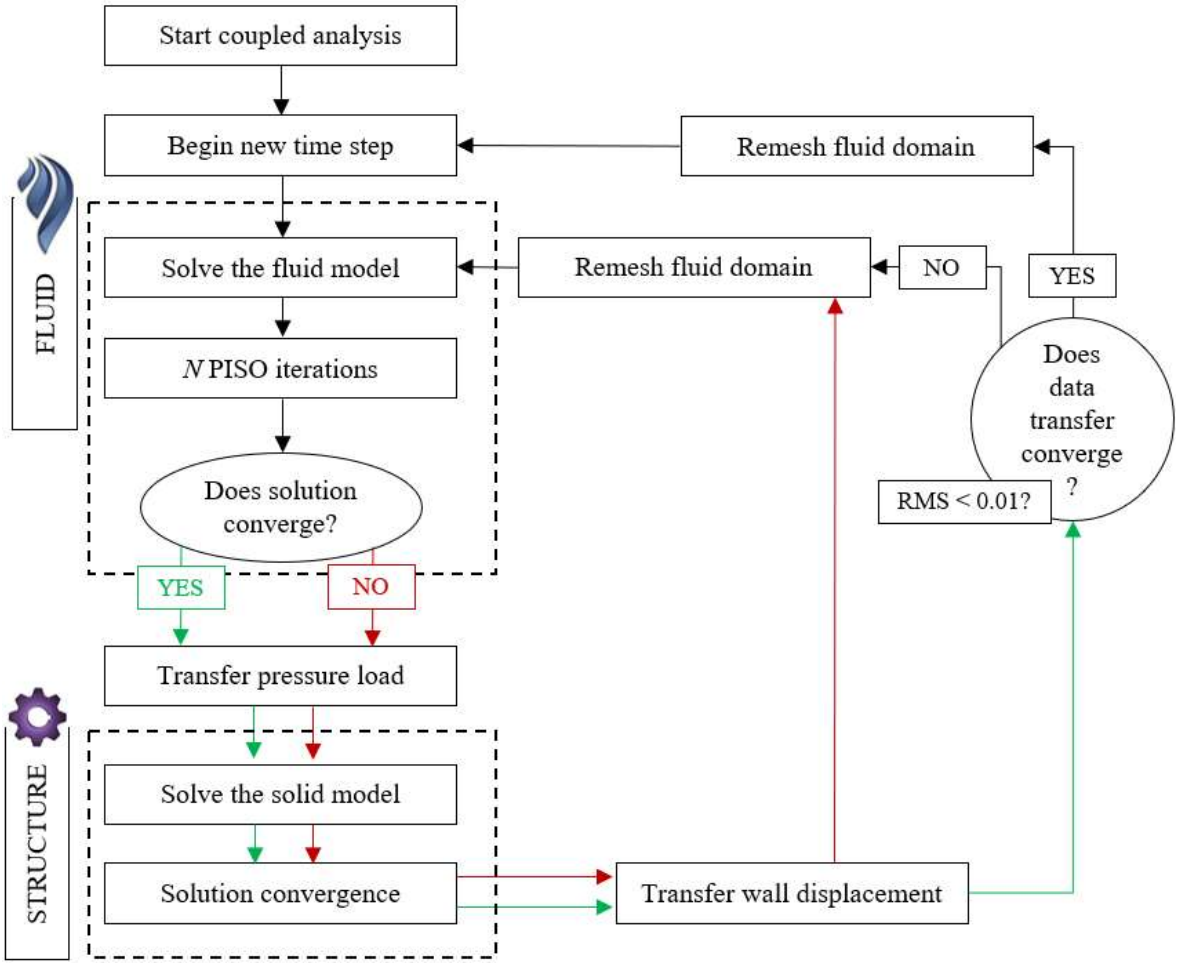

Figure 3.16. Schematization of a coupled simulation solving process. At the beginning of each time step, the coupling iteration begin until reaching the convergence of the data transfer. A coupling step starts with the solving of the fluid model and ends with the transfer of wall displacement.

3.7.2 Structural solver

The structural mesh generated in **Section 3.4** was imported in ANSYS Mechanical to set boundary conditions and solver parameters.

The FSI time step, controlled by the System Coupling, was set $\Delta t = 0.001$ s. For the structural analysis this was split in two sub-steps, each with $\delta t = 0.0005$ s.

Solver type and settings are program controlled in ANSYS Mechanical and exploit the Newton-Raphson scheme for the solution of the governing equation of the structural finite element problem in the displacement-based approach:

$$\mathbf{M}\,\bar{\ddot{\boldsymbol{u}}} + \mathbf{K}\,\bar{\boldsymbol{u}} = \bar{\mathbf{f}} \tag{3.18}$$

Where **M** and **K** are respectively the mass and stiffness matrix, $\bar{\mathbf{f}}$ is the load vector and $\bar{\ddot{\boldsymbol{u}}}$ and $\bar{\boldsymbol{u}}$ are the nodal acceleration and displacement respectively.

The viscoelasticity of the arterial wall can be modeled introducing a numerical damping in the mechanical solver. A Rayleigh damping was adopted with the following parameters: $\alpha = 5650$ and $\beta = 0.1$ [72]. These define the viscous matrix $\mathscr{C}$ as a linear combination of the mass and stiffness matrix:

$$\mathscr{C} = \alpha\mathbf{M} + \beta\mathbf{K} \tag{3.19}$$

Thus, the equation that is solved by ANSYS Mechanical becomes:

$$\mathbf{M}\,\bar{\ddot{\boldsymbol{u}}} + \mathscr{C}\,\bar{\dot{\boldsymbol{u}}} + \mathbf{K}\,\bar{\boldsymbol{u}} = \bar{\mathbf{f}} \tag{3.20}$$

Where $\bar{\dot{\boldsymbol{u}}}$ is nodal velocity.

3.7.3 Fluid solver

A pressure-based solver, using absolute velocity formulation and transient in time was adopted. Pressure-based implemented in ANSYS Fluent is based on the linear discretization of the continuity and momentum equations (**Equations 2.10-11**).

Pressure-velocity coupling was achieved using *Pressure-Implicit with Splitting of Operators* (PISO) algorithm. Starting from the pressure field p^* obtained from the solution of the momentum equation, the mass flux $\rho\boldsymbol{v}^* = \boldsymbol{J}_f^*$ through a cell face f is computed as:

$$\boldsymbol{J}_f^* = \hat{\boldsymbol{J}}_f^* + d_f(p_1^* - p_2^*) \tag{3.21}$$

Where $\hat{\boldsymbol{J}}_f^*$ is the convective mass flux, d_f an interpolation parameter and p_i the pressure in the *i*-th cell. This result generally doesn't satisfy continuity equation, consequently a correction factor of the flux was used to obtain the corrected face mass flux $\boldsymbol{J}_f$:

$$\boldsymbol{J}_f = \boldsymbol{J}_f^* + \boldsymbol{J}_f' \tag{3.22}$$

$$\boldsymbol{J}'_f = d_f(p'_1 - p'_2) \tag{3.23}$$

Where p' is the cell pressure correction. The correct pressure is finally obtained as:

$$p = p^* + URF_p \cdot p' \tag{3.24}$$

Where URF_p is the under-relaxation factor of pressure. After **Equation 3.24** is solved, the new velocities and corresponding fluxes generally do not satisfy the momentum balance. Hence, to achieve, *skewness correction* scheme was applied and one further iteration in the solution and coupling of **Equation 3.23** and **3.24** was performed.

Spatial gradients were discretized with a least square cell-based scheme, a second order interpolation scheme was used for calculating cell-face pressure and first order upwind interpolation scheme was adopted to discretize the convective terms in momentum equation. A second order implicit scheme was adopted for transient-time discretization. A 0.001 s time step gave a convergent solution and smaller time steps did not modify the result. A maximum of 150 iterations was set; after the initial time steps solution converged in ~20 iterations.

Under-relaxation factors for pressure and momentum were set equal to 0.3 and 0.7 respectively. The convergence of the solution was assessed for residual errors below 10^{-4}, according to [38].

3.8 CFD simulations

In parallel with the FSI analysis, CFD simulations with the same boundary conditions were run for comparison purpose. Simulations of 2 cardiac cycles took an average of 2 days running on 24 cores on a cluster server with Intel® Xeon® CPU X5670 at 2.93 GHz processor for a total of 192 Gb RAM.

Furthermore, a sensitivity analysis of the inlet boundary conditions was performed for the pre-intervention model. Three inlet boundary conditions were tested: a flat velocity profile, a parabolic velocity profile and the patient specific velocity profile (**Figure 3.17**). Profiles were defined so that the resulting inlet flow rate was the same. Results were then compared with 4D flow analysis.

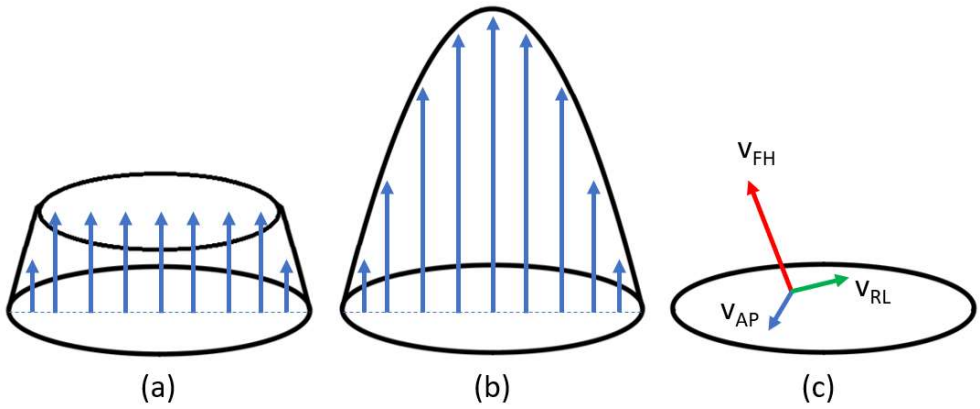

Figure 3.17. Schematic representation of the three boundary conditions tested: flat velocity profile (a), parabolic profile (b) and patient specific profile (c). For (c), velocity components are shown in an example point.

3.9 Postprocessing

Herein, the results that were exported from FSI and CFD solutions, for postprocessing purpose are reported.

- Fluid solver: WSS (OSI, TAWSS), velocity field (contours, streamlines), pressure.
- Structural solver: wall stress, strain and displacement.

WSS were compared between the pre and post-intention model at systolic peak, when they reach their maximum. WSS is a fluid dynamic quantity that plays a fundamental role in the triggering of the atherogenic mechanism, in particular, the vascular wall is sensible to time variations of the direction and modulus of WSS [73][25]. The oscillatory shear index (OSI) is a measure of the influence of the oscillatory component of WSS. It is defined as:

$$\mathrm{OSI} = \frac{1}{2}\left(1 - \frac{\left|\int_0^T \overrightarrow{WSS}\,dt\right|}{\int_0^T \left|\overrightarrow{WSS}\right|dt}\right) \tag{3.25}$$

This definition implies that $0 \leq \mathrm{OSI} \leq 0.5$; values of OSI close to 0 indicate that there is no flow inversion, while values close to 0.5 enhance the atherogenic process [26].

The average shear stress experienced by the wall tissue is expressed by the time average wall shear stress (TAWSS), defined as:

$$\text{TAWSS} = \frac{1}{T}\int_0^T \overrightarrow{WSS}\,dt \tag{3.26}$$

Nodal values of WSS were exported at 40 equally spaced time points throughout the cardiac cycle. A MATLAB™ code was then implemented to compute OSI and TAWSS.

Velocities were visualized as streamlines and contours on section planes, to compare results from numerical simulations and 4D flow analysis. Both a qualitative and a quantitative comparison were achieved.

Pressure was exported at the inlet and compared with clinically measured systolic and diastolic pressures.

The maximum principal stress (σ_1), the maximum principal strain (ε_1) and displacement ($\boldsymbol{u}$) distribution of the wall were qualitatively compared with contour plots. The position and magnitude of σ_1, ε_1 and $\boldsymbol{u}$ were also compared.

Chapter 4
Results

Chapter summary

In this chapter the results obtained from numerical simulations will be presented. The first part covers the sensitivity of the results to the mesh and to the inlet boundary condition. In the second part, results of FSI (and CFD) analysis are compared to 4D flow to verify the reliability. Finally, a comparison between the presurgical and the postsurgical model is reported, with a focus on the WSS (and related hemodynamic indexes) distribution in the descending aorta.

4.1 Introduction

In this chapter, the following results obtained though the workflow described in **Chapter 3** will be presented:

- Mesh sensitivity analysis
- Sensitivity analysis to inlet boundary condition
- Sensitivity to the numerical solution method
    - FSI simulation pre-intervention (compared to a CFD simulation)
    - FSI simulation post-intervention (compared to a CFD simulation)

Particular attention will be paid to the descending aorta tract, as different studies suggested the risk of TAA reformation in that region, due to the alteration of hemodynamics [19][24]. Results were validated against 4D flow analysis and, when possible, were compared with available clinical parameters.

4.2 Mesh sensitivity

Sensitivity analysis of the mesh was performed as described in **Section 3.3.1**. For the three meshes tested (fine = 1, medium = 2, coarse = 3) the maximum velocities (i.e. the chosen grid convergence parameter) on the chosen transverse plane in the descending aorta were found to be $f_1 = 73.9$ cm/s, $f_2 = 72.6$ cm/s and $f_3 = 71.1$ cm/s. **Figure 4.1** shows the velocity contours on the plane considered in the descending aorta tract. Similar velocity patterns were captured, with small variations (~2%) of the maximum value. Grid convergence indexes computed with **Equation 3.1-3.4** result $GCI_{1,2} = 1.34\%$ and $GCI_{1,2} = 1.39\%$ respectively. Their ratio defined through **Equation 3.5** was found to be $k = 1.0191$. Values of k close to 1 ensure that the meshes are in the asymptotic range of convergence.

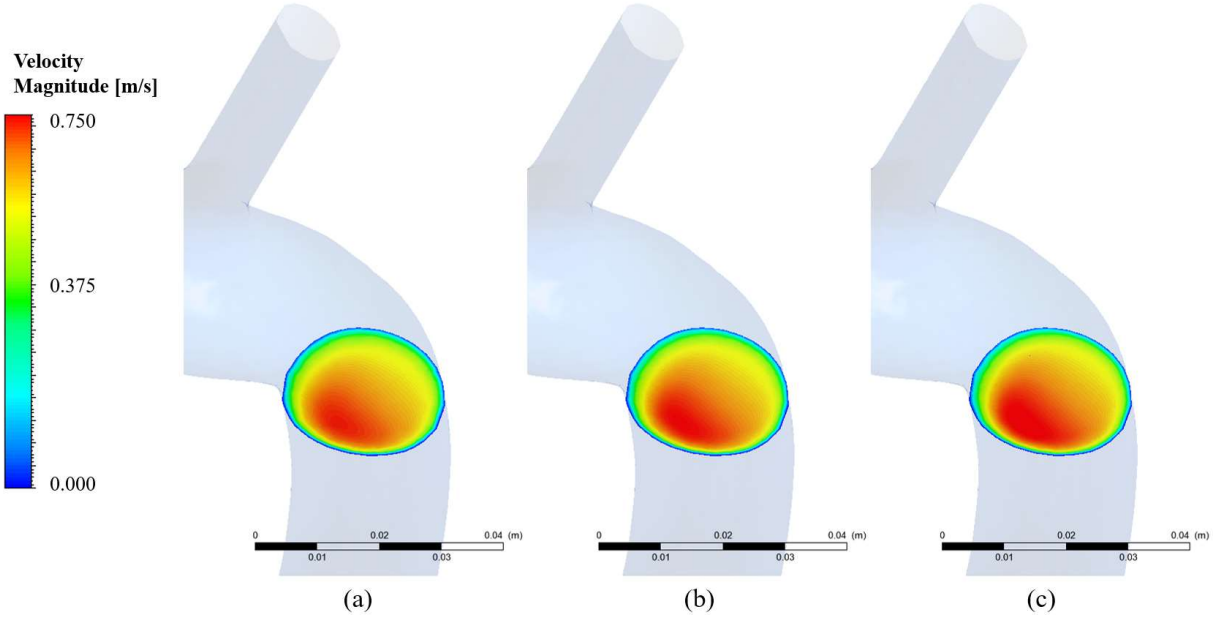

Figure 4.1. Velocity contours on a cross section plane in the descending aorta, obtained with a coarse (a), medium (b) and fine (c) mesh. Similar velocity patterns are detected in all the three cases, higher (~2%) velocities are obtained with a fine mesh.

The chosen mesh for the fluid domain (**Figure 4.2**) consisted of 2.7 million of tetrahedral elements. Maximum element size was set equal to 1 mm. Average values mesh quality metric parameters were the following:

- Aspect ratio: 1.797 ± 0.4502
- Skewness: 0.20562 ± 0.15104

- Orthogonal quality: 0.87125 ± 0.3147

Further information about mesh quality are provided in **Figure 4.3**.

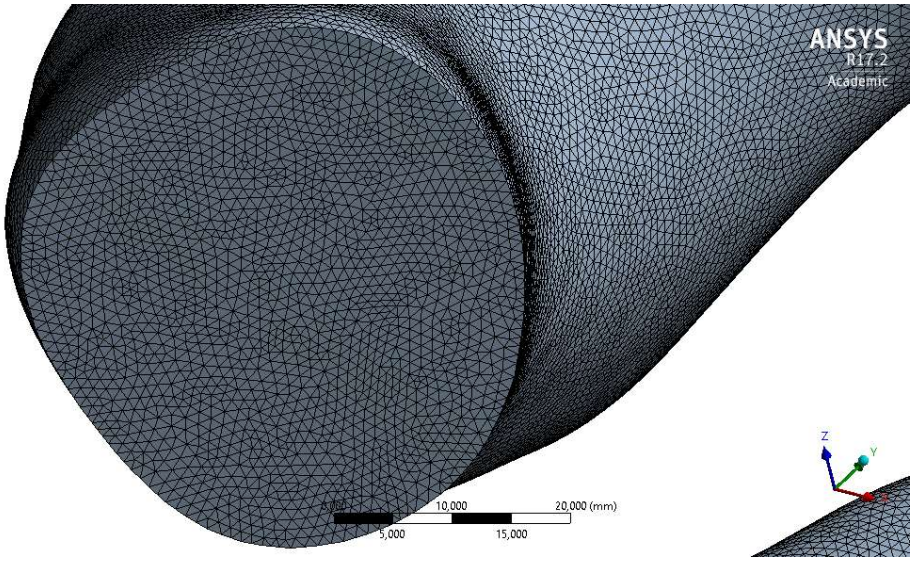

Figure 4.2. Visualization of the computational mesh of the fluid domain (zoomed-in of the aortic inlet).

The solid domain was meshed with tetrahedral elements of the same size used for the fluid domain. A 500k elements mesh was generated in ANSYS Meshing embedded tool (**Figure 4.4**). Elements aspect ratio, skewness and orthogonal quality were used for mesh quality evaluation purpose, their distributions are provided in **Figure 4.3**.

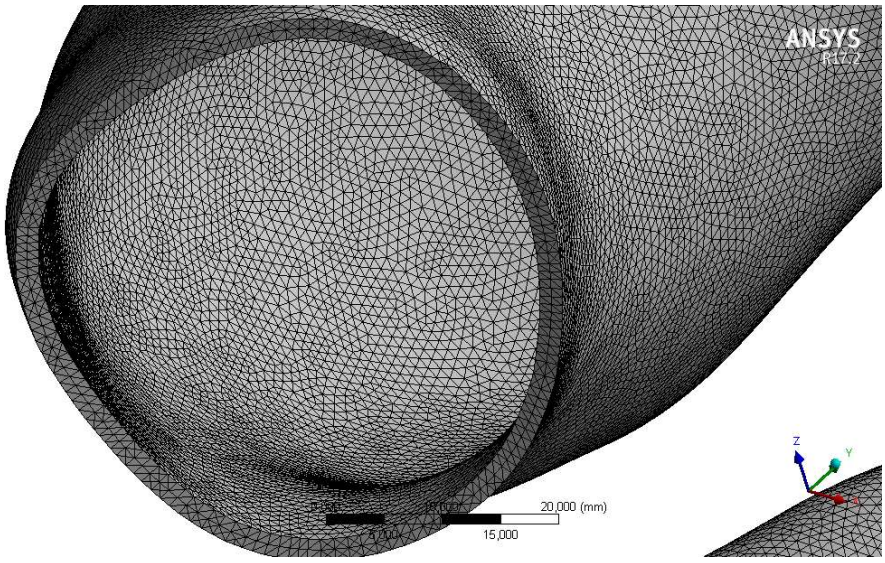

Figure 4.4. Visualization of the computational mesh of the solid domain (zoomed-in of the aortic inlet).

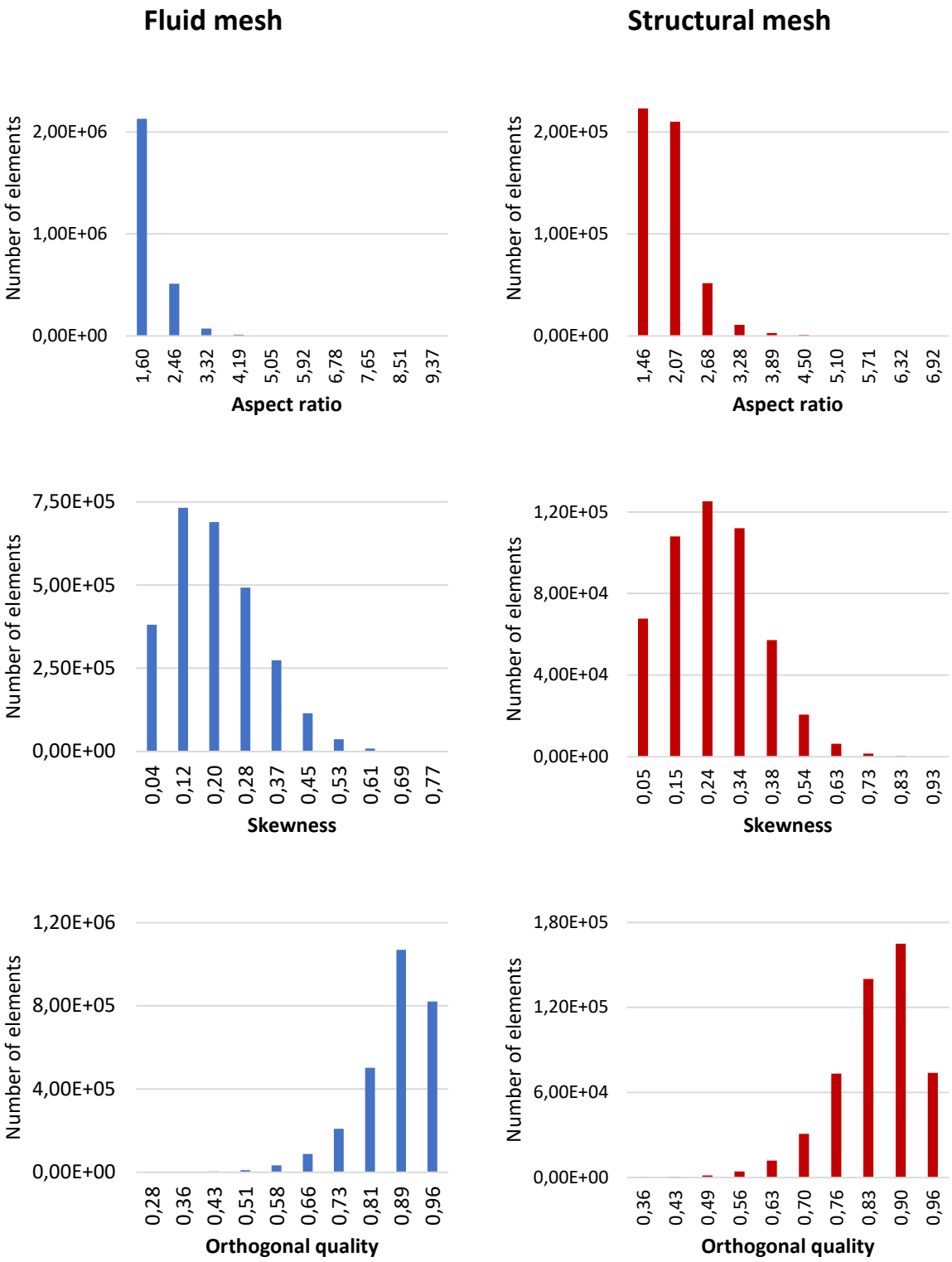

Figure 4.3. From top to bottom, the aspect ratio, element skewness and orthogonal quality distribution in the computational grid of the pre-intervention model. Values of skewness close to 0, values of orthogonal quality and aspect ratio close to 1, indicate a good mesh quality. Graphics on the left refer to fluid mesh, on the right to solid mesh.

The characteristics of the used meshes – the number of nodes and elements, the average size and the type of the elements, the aspect ratio, skewness and orthogonal quality – for the pre and post-intervention models are summarized in **Table 4.1**.

Mesh	No. of nodes	No. of elements	Size	Type	Aspect ratio	Skewness	Orthogonal quality
Pre (fluid)	478×10^3	2.73×10^6	1.00	Tet	1.79 ± 0.45	0.20 ± 0.11	0.86 ± 0.08
Pre (solid)	828×10^3	500×10^3	1.25		1.90 ± 0.47	0.25 ± 0.13	0.84 ± 0.08
Post (fluid)	286×10^3	1.59×10^6	1.00	Tet	1.80 ± 0.45	0.21 ± 0.11	0.86 ± 0.08
Post (solid)	905×10^3	562×10^3	1.25		1.94 ± 0.56	0.26 ± 0.14	0.83 ± 0.09

Table 4.1. Mesh characteristics for the two models. Mesh metrics information are reported as mean value ± standard deviation. Tet = tetrahedron.

4.3 Sensitivity to inlet boundary conditions

Sensitivity of the results to the applied boundary conditions at the inlet of the fluid domain was tested for the pre-intervention model with three CFD simulations. For the three tested boundary conditions – plug velocity profile, parabolic profile and local velocity components – streamlines in the ascending aorta were compared with 4D flow at systolic peak (**Figure 4.6**). Small recirculation was observed in the plug profile and parabolic profile simulations, at the intrados and proximal to the inlet respectively. However, the streamline pattern and velocity magnitude are strongly different, compared to 4D flow. The best agreement was observed for the simulation in which local velocity components were used as boundary condition. This was the only boundary condition that permitted to reproduce the skewness of the profile, the formation of the vortex in the ascending aorta and that matched the velocity field and thus was adopted for the FSI simulations.

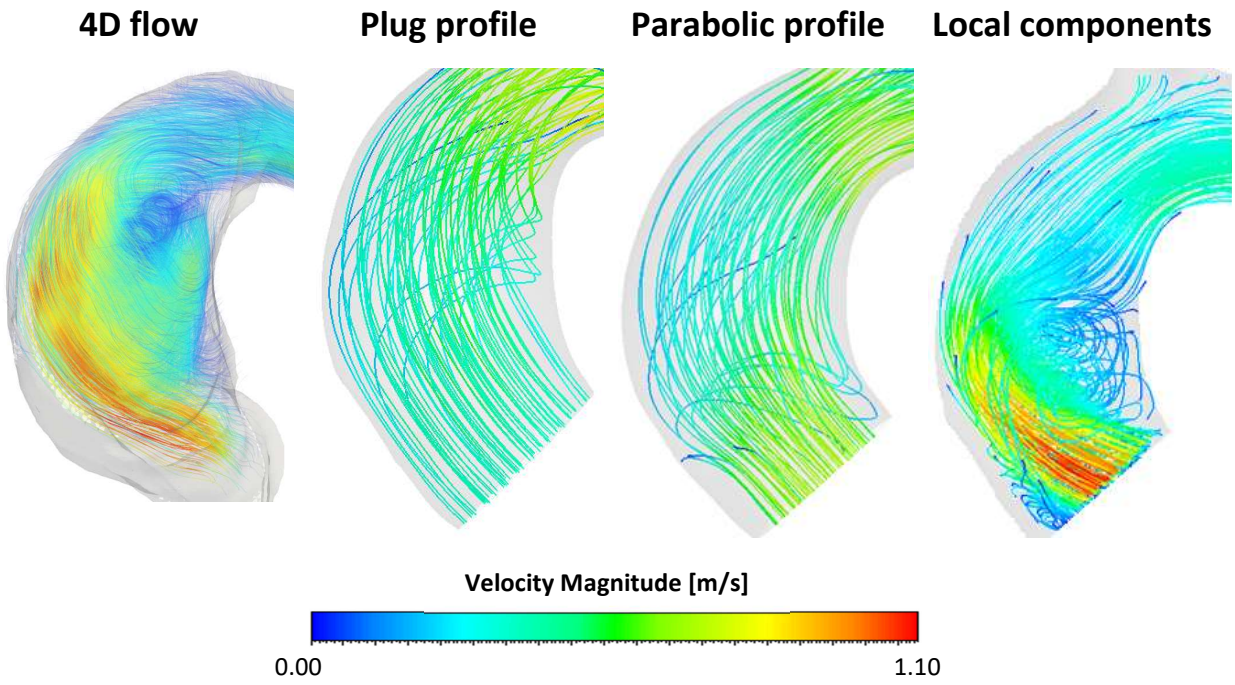

Figure 4.6. Streamlines at systolic peak obtained with 4D flow and 3 simulations with different boundary condition. Only the local velocity components profile was able to properly capture the hemodynamic in the ascending aorta.

4.4 Comparison with 4D flow and clinical data

Central blood pressure (CBP) was clinically measured non-invasively prior both MR scanning (pre and post-operation). A systolic pressure (SP) equal to 132 mmHg and a diastolic pressure (DP) equal to 85 mmHg were found (pulse pressure = 47 mmHg) in the scanning pre-intervention, while a SP = 127 mmHg and a DP = 82 mmHg (pulse pressure = 45 mmHg) were acquired in the post-intervention scanning. Pressure computed at the aortic inlet in the FSI model was compared with these values. A SP = 124 mmHg and a DP = 83 mmHg (pulse pressure = 41 mmHg) were obtained with the FSI pre-intervention model, while a SP = 114 mmHg and a DP = 76 mmHg (pulse pressure = 38 mmHg) were found in the post-intervention model (values are summarized **Table 4.2**).

	Pre-intervention		**Post-intervention**	
	Systolic pressure	Diastolic pressure	Systolic pressure	Diastolic pressure
Clinical data	132	85	127	82
FSI solution	124	83	114	76

Table 4.2. Values of central blood pressure (in mmHg) measured clinically and obtained from numerical simulations.

Thus, a physiological pressure range was reproduced, slightly lower than the operative range of the patient's aorta. SPs were underestimated by ~7% and ~8% (pre and post-intervention respectively), while DPs by ~2% and ~10% (pre and post-intervention respectively). This difference in pressures may be due to an improper arterial wall characterization (too low Young modulus) and to a possible error in the non-invasive measure of CBP (the algorithm that is used to derive CBP may induce some error in the measurement).

4.4.1 Pre-intervention FSI v. 4D flow

The results obtained from each numerical simulation described in **Chapter 3** (FSI and CFD) were compared to 4D flow MRI data. A non-parametric ANOVA was performed comparing percentiles populations of velocity on each plane. Furthermore, a qualitative validation against 4D flow was performed by comparing streamlines and velocity contours on specific planes in the domain, at systolic peak. Three cross-sectional planes in the ascending aorta and three cross-sectional planes in the descending aorta were considered (**Figure 4.7**).

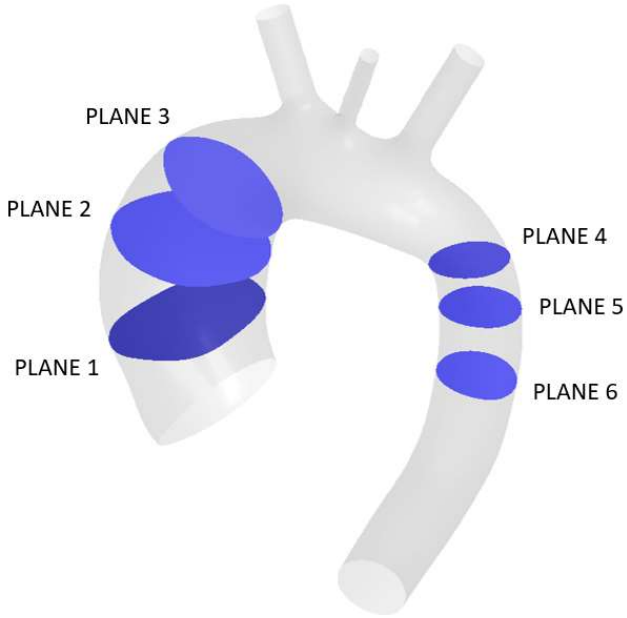

Figure 4.7. Cross-sectional planes along ascending and descending aorta where velocity contours were visualized.

The ANOVA results never showed a statistically significant difference between 4D flow and FSI simulation, while the difference was strongly marked between 4D flow and CFD, especially in descending aorta (**Figure 4.9**). Comparison between CFD and 4D flow returned p-values <0.01, <0.0001, <0.001 and <0.001 on PLANE 3-6 respectively. Comparison between CFD and FSI returned p-values <0.05, <0.01, <0.05 and <0.05 on PLANE 3-6 respectively.

Comparing the streamlines at systolic peak, similar vortical structures pattern was observed in the ascending aorta (**Figure 4.8**). Both in the 4D flow and FSI simulation vortexes generated at the intrados of the aortic sector interested by the aneurysm. In 4D flow vortexes developed along the whole intrados, while in FSI vortexes were observed until mid-ascending aorta. CFD simulation showed a pattern similar to FSI.

On PLANE 1 (**Figure 4.10**) the velocity profile peak was located in the same area (at the extrados) as in the 4D flow analysis in FSI result, however, higher velocities were observed in rest of the cross-section. On PLANE 2 the peak was more pronounced in the FSI simulation, but it was located in the same area as 4D flow. Velocities in rest of the section resulted lower. On plane PLANE 3 the two contours showed the largest mismatch, except for the position of the peak. A good agreement between 4D flow and FSI simulation in terms of velocity profile shape and peak location was observed on the three planes in descending aorta (PLANE 4-6).

Contours obtained from CFD analysis (**Figure 4.10**) showed pattern similar to FSI in the ascending aorta (PLANE 1-3), while higher velocities were obtained in descending aorta.

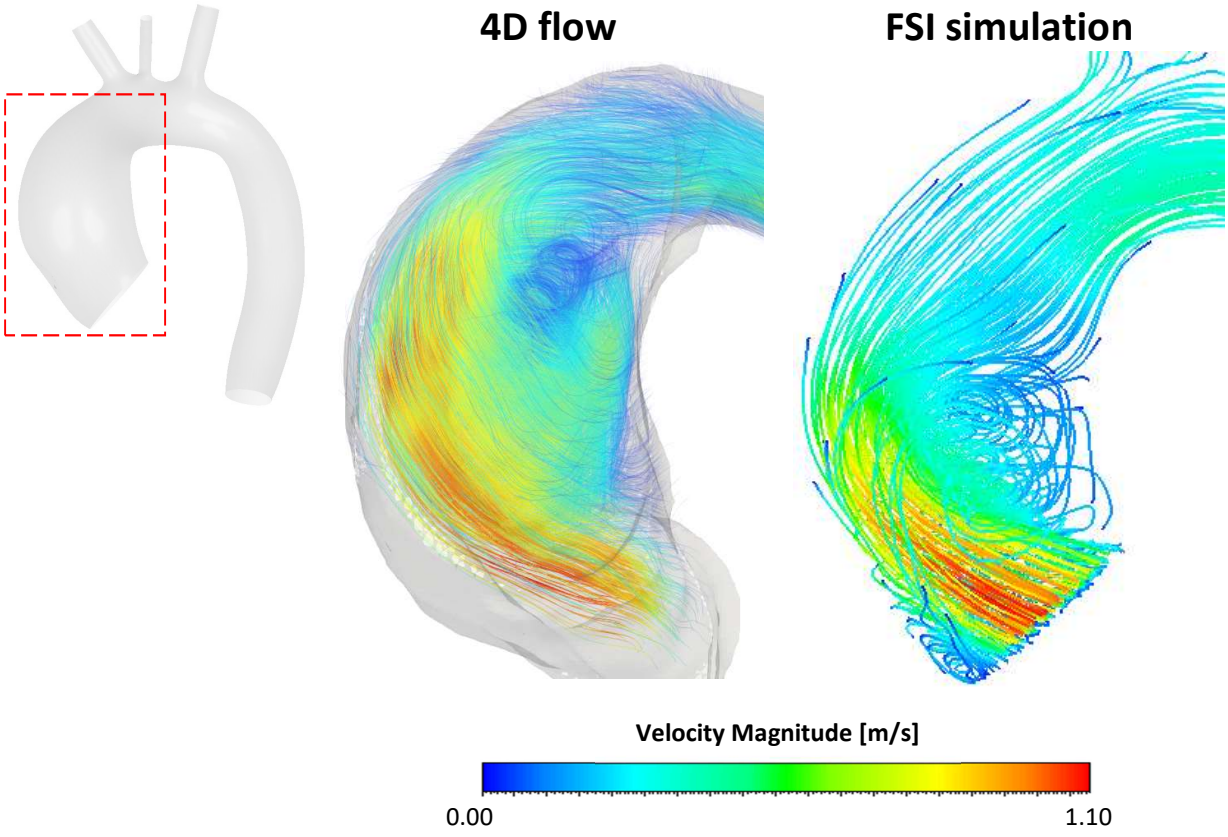

Figure 4.8. Comparison of streamlines in the ascending aorta (4D flow v. FSI simulation) at systolic peak.

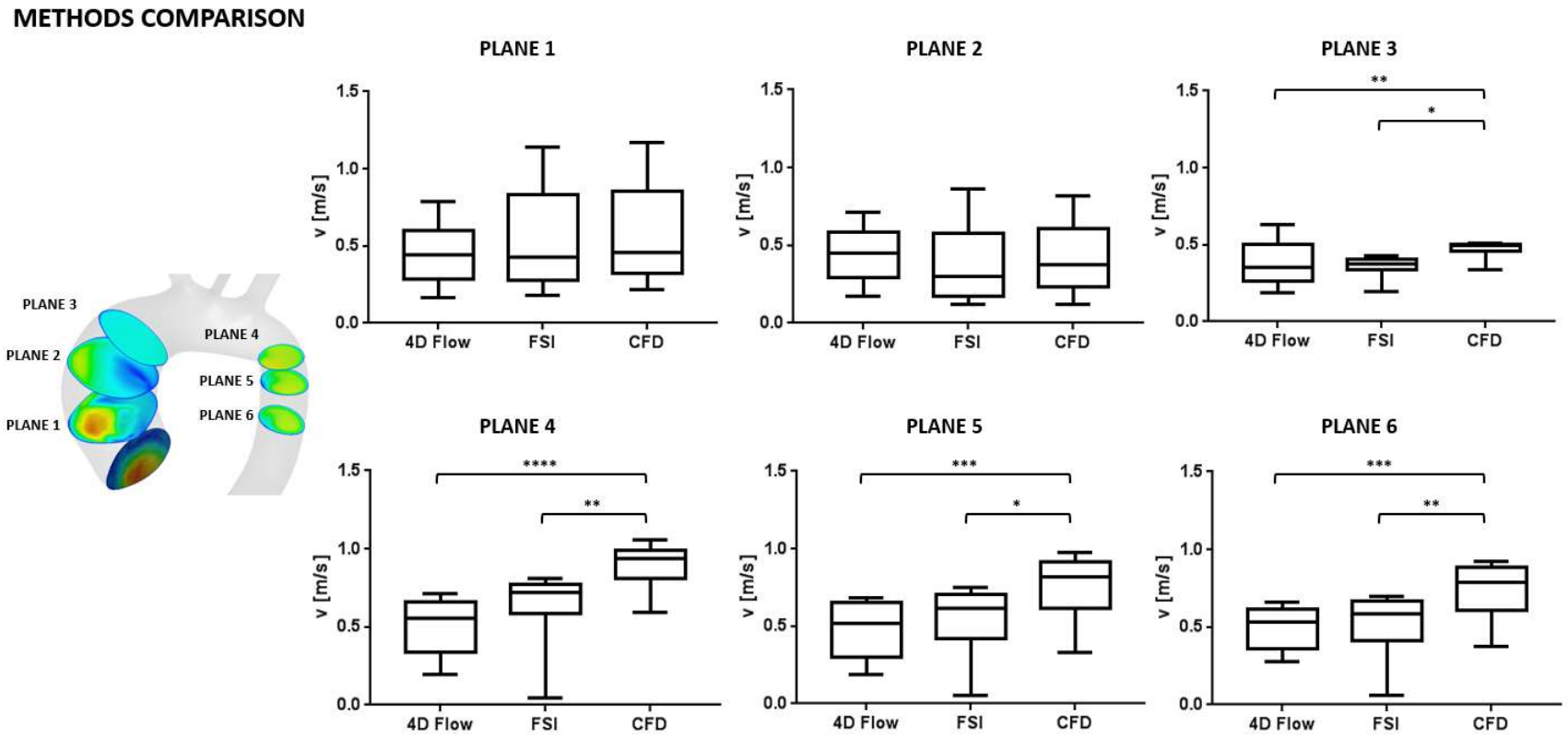

Figure 4.9. Comparison between percentiles population (10^{th} to 90^{th}) of velocities obtained with 4D flow analysis, FSI simulation and CFD simulation. On each plane, no statistical difference was observed between 4D flow and FSI population. A marked difference is observed (especially on PLANE 4-6) between 4D flow and CFD population. Asterisks indicate the *p*-value: * = $p<0.05$, ** = $p<0.01$, *** = $p<0.001$ and **** = $p<0.0001$.
Dataset of ANOVA results is reported in **Appendix**.

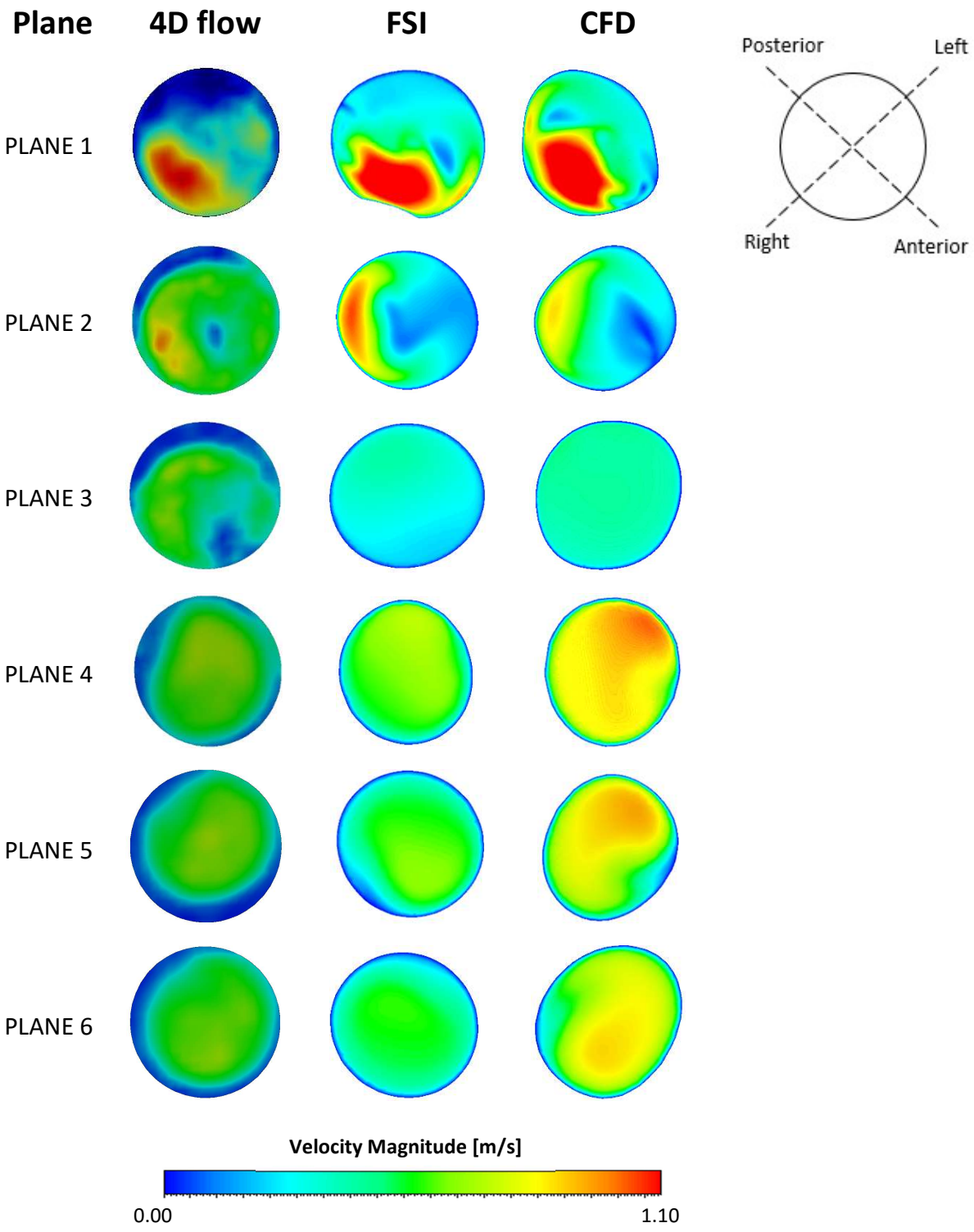

Figure 4.10. Velocity magnitude comparison (4D flow v. FSI v. CFD simulation) at systolic peak on the six cross-section planes considered (pre-intervention).

4.4.2 Post-intervention FSI v. 4D flow

In the post-intervention model, the considered cross-sectional planes in the ascending aorta and in the descending aorta are shown in **Figure 4.11**.

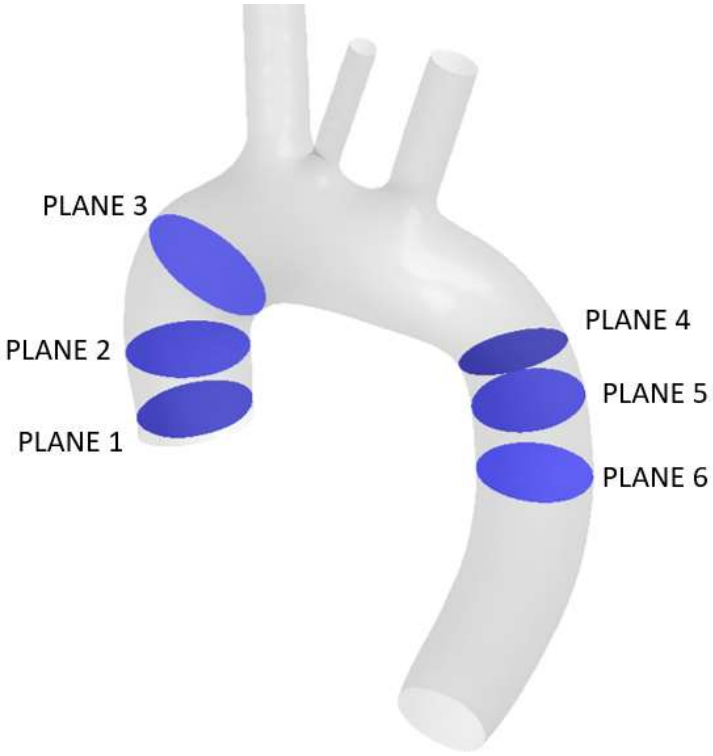

Figure 4.11. Cross-sectional planes along ascending and descending aorta where velocity contours were visualized.

The ANOVA results (**Figure 4.13**) showed no statistically relevant difference between the velocity populations on PLANE 1-3. Statistically relevant difference was obtained from the comparison between 4D flow and CFD population on PLANE 4-6 (p-value <0.05, <0.01 and <0.01) and between FSI and CFD population on PLANE 4-6 (p-value <0.05, <0.01 and <0.01).

Streamlines comparison at systolic peak showed both in the 4D flow analysis and FSI simulation, a similar physiological pattern. Blood flow in the ascending aorta was sustained, with no vortical structure formation (**Figure 4.12**), suggesting that VSR surgery successfully restore physiological hemodynamics in the ascending aorta.

The comparison between velocity contours from 4D flow and numerical simulation for the post-intervention model is shown in **Figure 4.14** for the FSI and CFD model respectively. In general, a better agreement (with respect to the pre-intervention model) can be observed. On PLANE 1 and 2, both FSI and CFD were able to capture with a good matching the velocity distribution. On plane

PLANE 3 both numerical simulation overestimated velocities, however a slightly more accurate result is obtained with the FSI. A good agreement between 4D flow and FSI simulation in terms of velocity profile shape and peak location was observed on the three planes in descending aorta (PLANE 4, 5 and 6). Higher velocities were obtained in descending aorta with the CFD simulation.

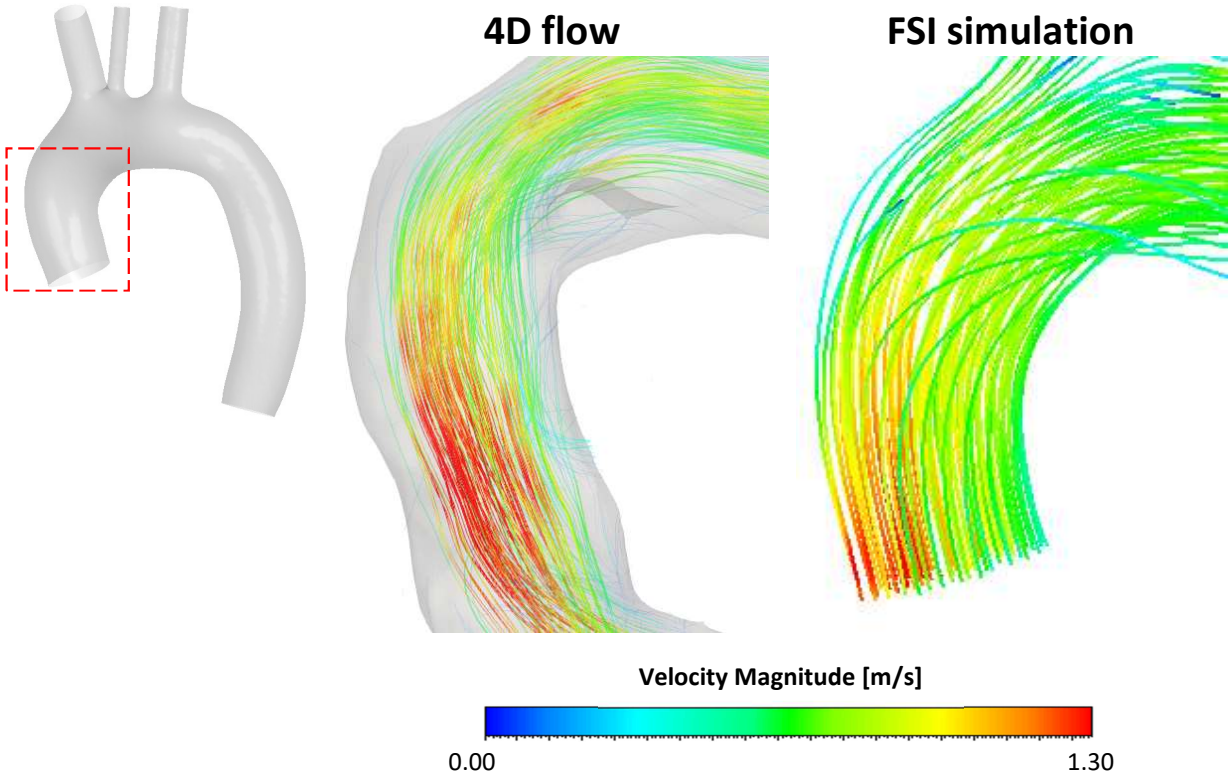

Figure 4.12. Comparison of streamlines in the ascending aorta (4D flow v. FSI simulation) at systolic peak.

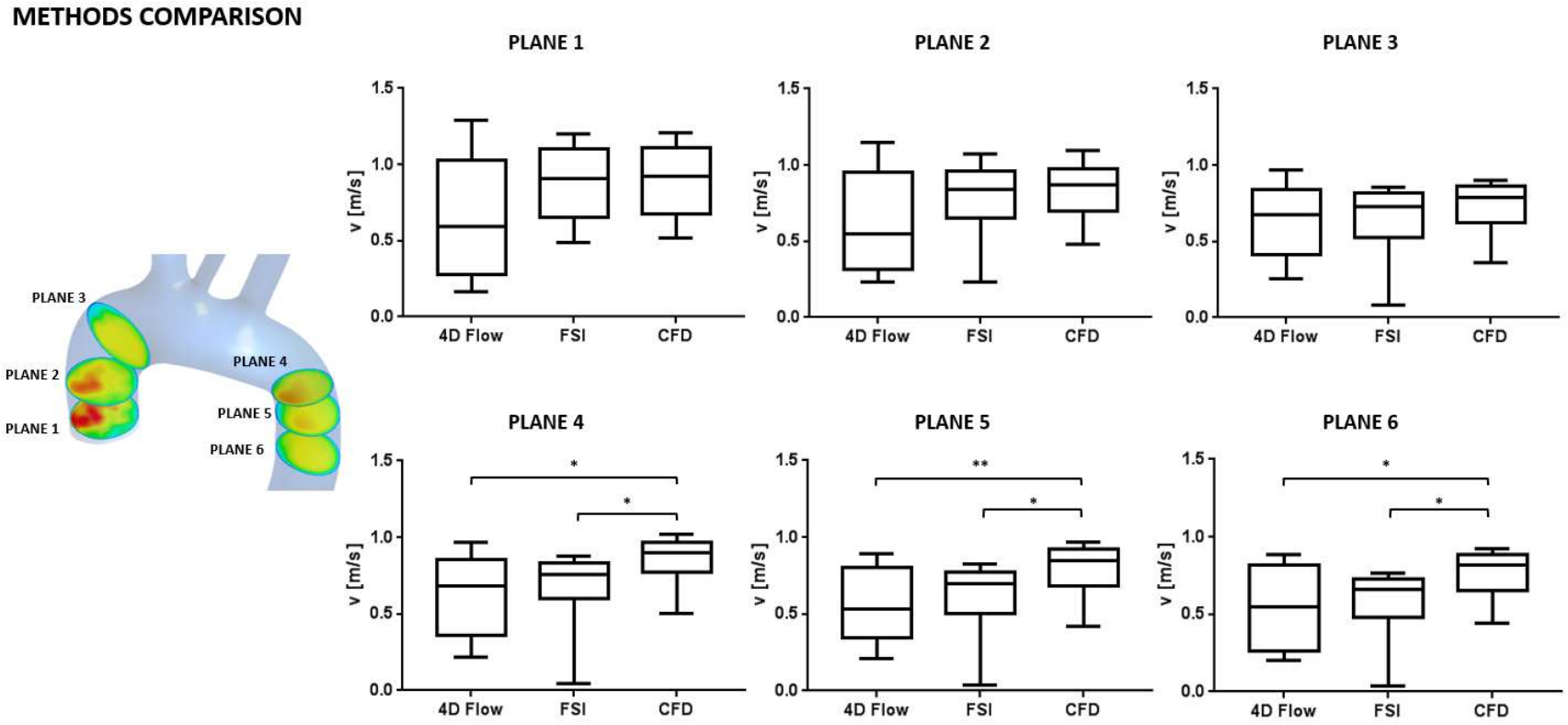

Figure 4.13. Comparison between percentiles population of velocities obtained with 4D flow analysis, FSI simulation and CFD simulation. On each plane, no statistical difference was observed between 4D flow and FSI population. Statistical difference was observed on PLANE 4-6 between 4D flow and CFD and between FSI and CFD. Asterisks indicate the *p*-value: * = $p<0.05$, ** = $p<0.01$, *** = $p<0.001$ and **** = $p<0.0001$.

Dataset of ANOVA results is reported in **Appendix**.

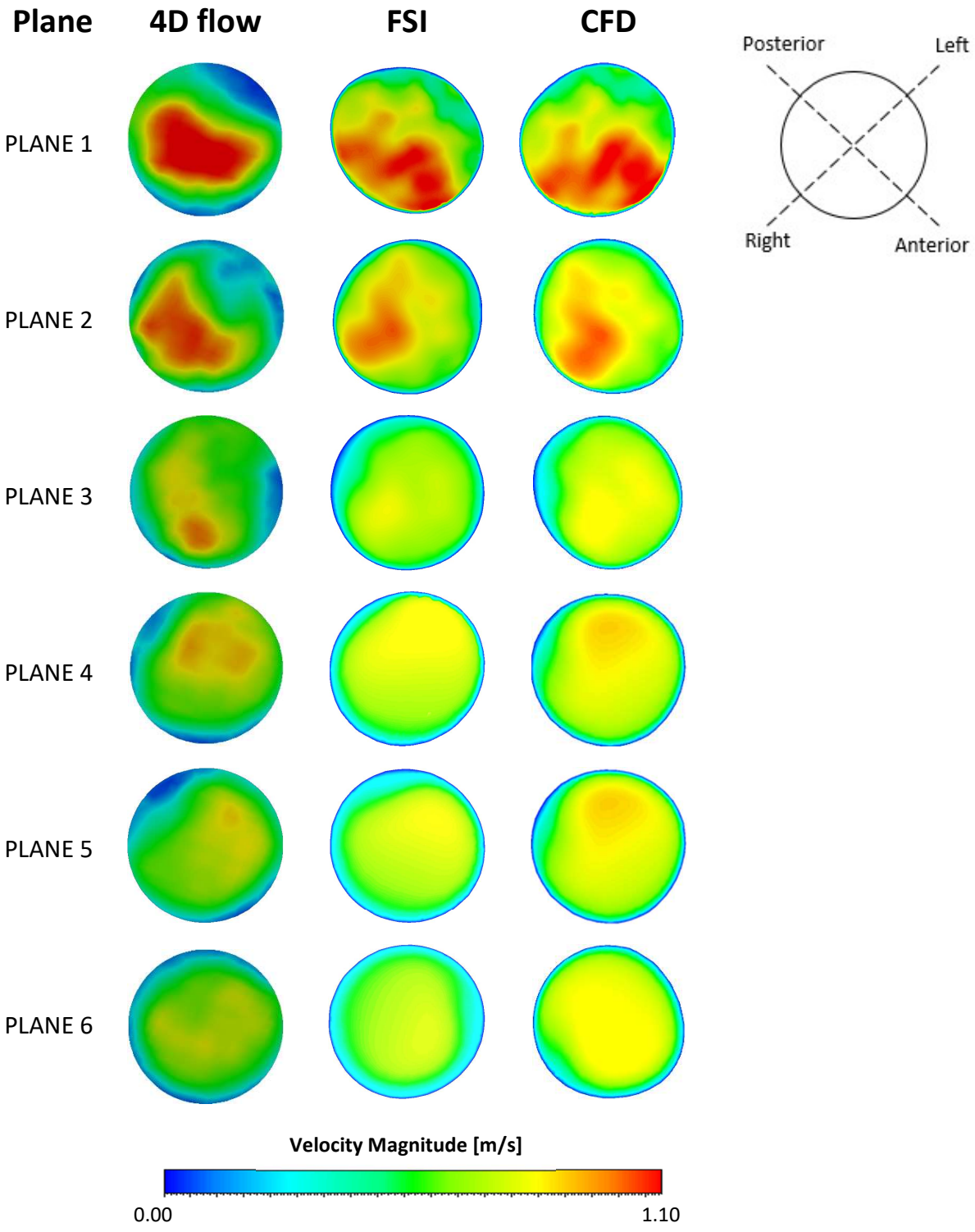

Figure 4.14. Velocity magnitude comparison (4D flow v. FSI v. CFD simulation) at systolic peak on the six cross-section planes considered (post-intervention).

4.5 Comparison pre-intervention v. post-intervention

4.5.1 Velocity

Pre-intervention

Velocity contours of blood on a longitudinal plane, obtained from FSI analysis, are illustrated in **Figure 4.15** for pre-intervention model, in the ascending (top row) and descending aorta (bottom row). A projection of the tangential component of local velocity was used to emphasize the formation of vortical structures in the ascending tract. At the intrados of the descending aorta vein fluid detachment was observed. At systolic peak a maximum velocity $v_{max} = 1.17$ m/s was obtained.

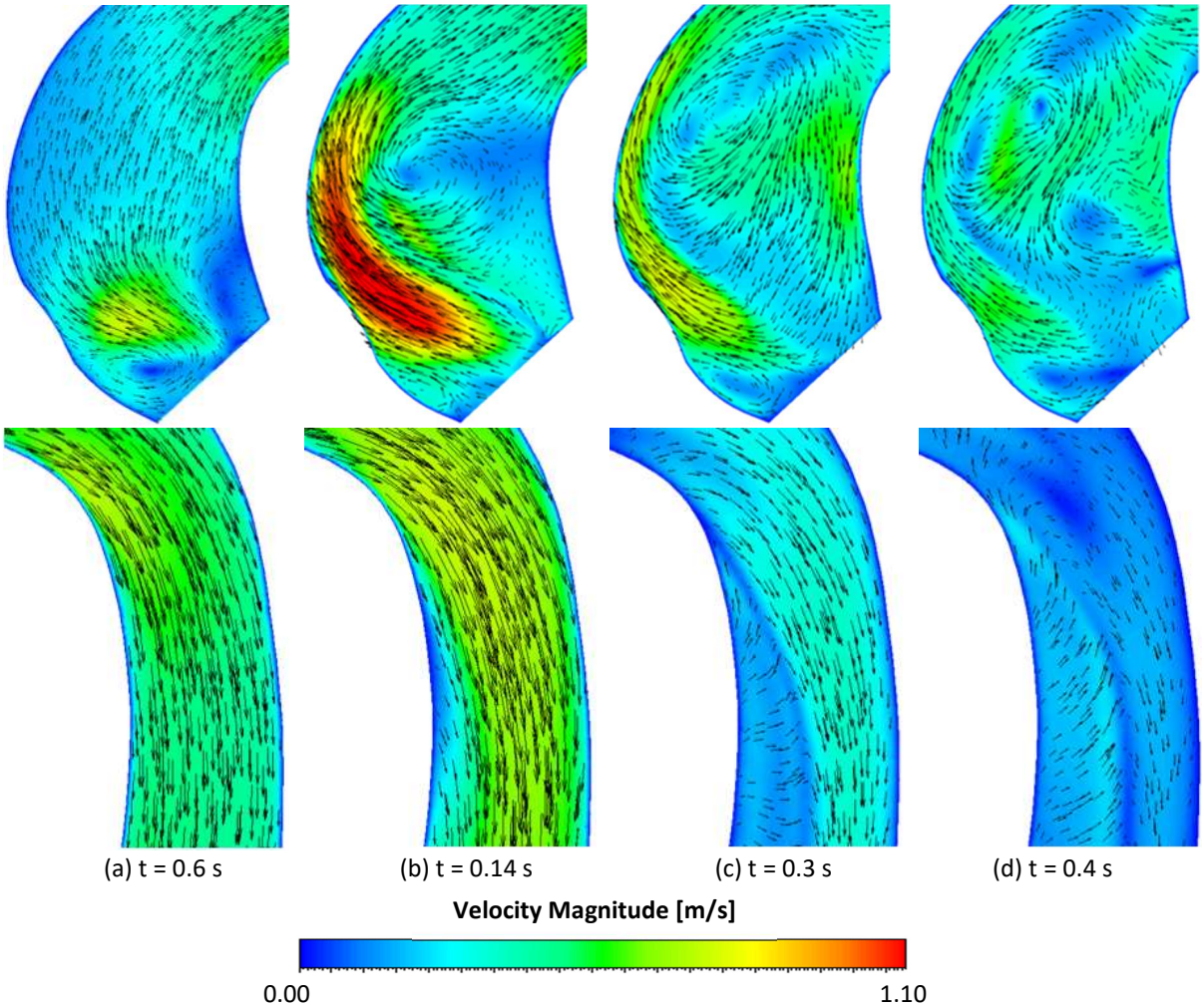

Figure 4.15. Velocity maps on a longitudinal plane in the ascending aorta (top row) and descending aorta (bottom row). Maps were taken at early systole (a), systolic peak (b), end systole (c) and early diastole (d).

Post-intervention

Velocity contours obtained from post-intervention FSI analysis, are reported in **Figure 4.16** in ascending (top row) and descending aorta (bottom row). As for pre-intervention model, a projection of the tangential component of local velocity was overlapped to the velocity map. No recirculation was observed during systolic phase, while it formed in diastole, in the ascending aorta. In diastole, at the intrados of the descending aorta vein fluid detachment was observed. At systolic peak a maximum velocity $v_{max} = 1.34$ m/s was obtained. In general, higher velocities were obtained, compared to the pre-intervention case.

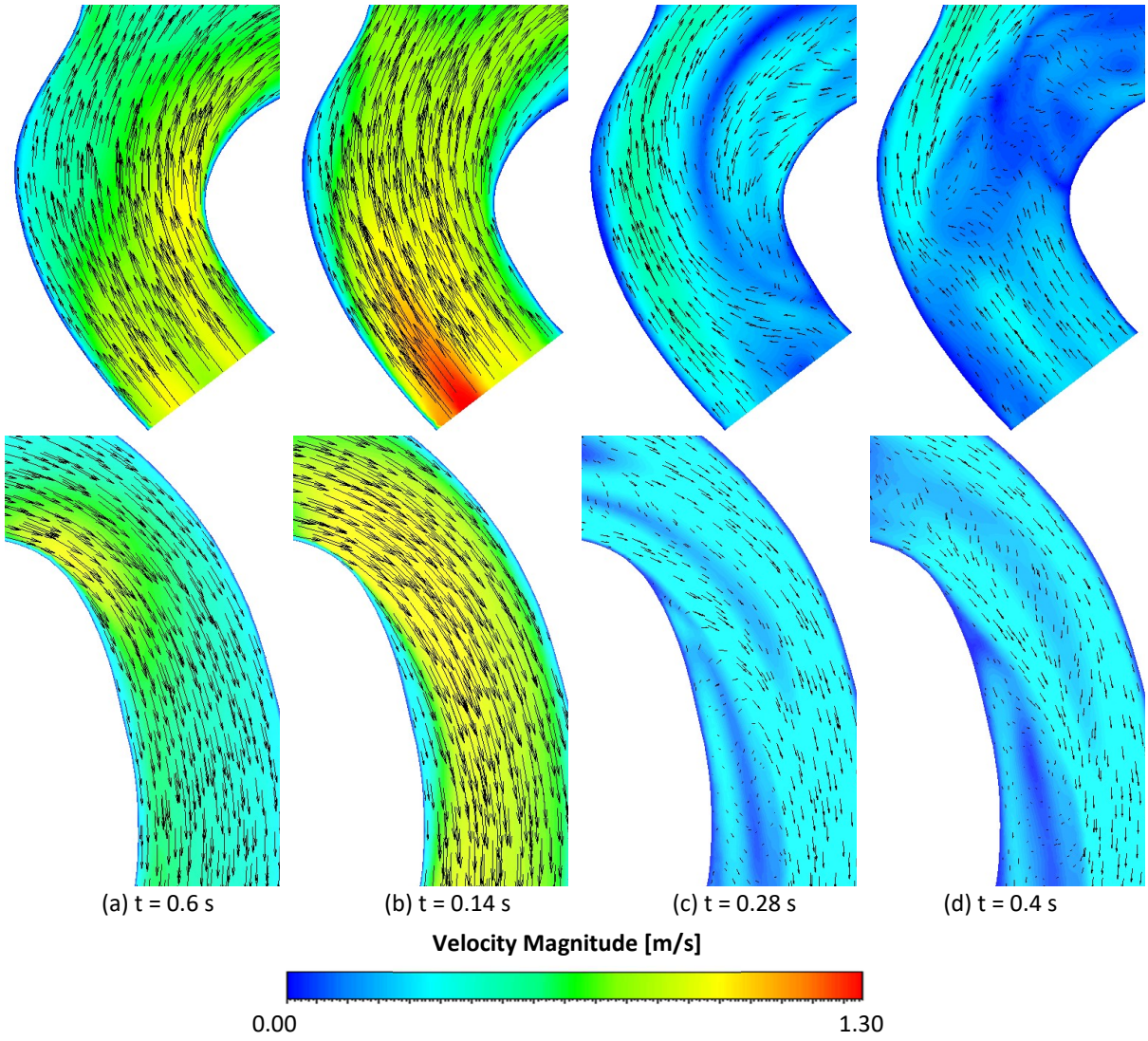

Figure 4.16. Velocity maps on a longitudinal plane in the ascending aorta (top row) and descending aorta (bottom row). Maps were taken at early systole (a), systolic peak (b), end systole (c) and early diastole (d).

4.5.2 Wall shear stress, OSI and TAWSS

Pre-intervention

Spatial distribution at systolic peak of WSS in the pre-intervention model is shown in **Figure 4.17**. Higher WSS magnitude were obtained at the supra-aortic branches (WSS exceeded 28 Pa in the LCCA), due to high speed flow and velocity gradients entering smaller branches [74]. A maximum value of WSS = 16 Pa was observed in the intrados of the descending aorta.

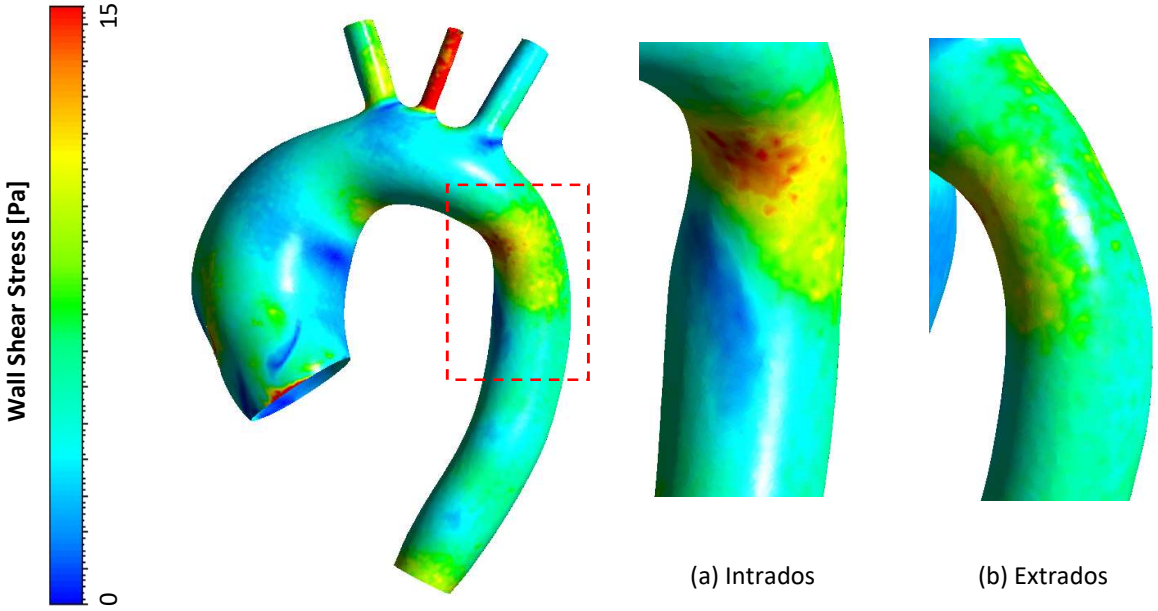

Figure 4.17. Wall shear stress (WSS) acting on the arterial wall at systolic peak. On the right side, a zoom-in (red box) of the WSS distribution in the intrados (a) and extrados (b) of the proximal descending aorta.

Figure 4.18 illustrate spatial distribution of oscillatory shear index (OSI) in the model. OSI values proximal to 0.5, index of the atherogenic process starting risk [26][75], were observed in various region of the model: in the extrados of the aortic root, in the aortic arch and in the intrados of the descending aorta.

Time average wall shear stress (TAWSS) distribution is illustrated in **Figure 4.19**. Higher TAWSS in the ascending aorta occurred in the extrados, with an average value of 5-7 Pa and a peak value of 10 Pa, in various isolated positions. In the descending aorta, an average TAWSS of 2-4 Pa was observed, with a maximum value of 5.5 Pa in the intrados, proximal to the aortic arch.

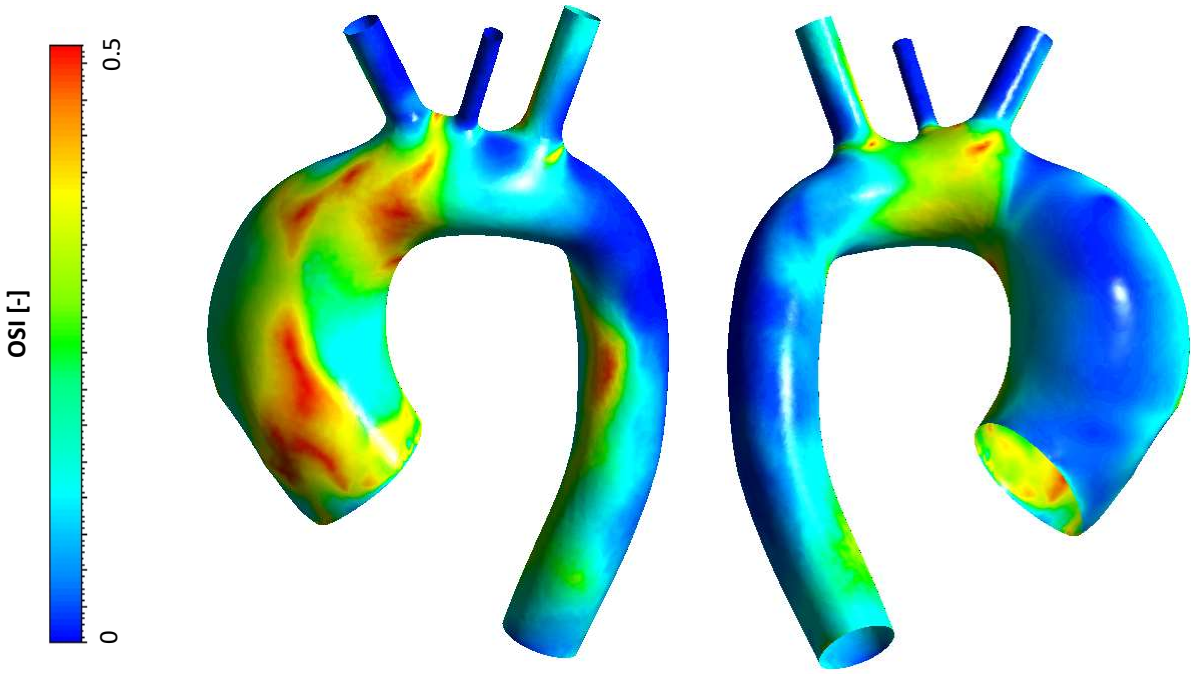

Figure 4.18. Oscillatory shear index (OSI) distribution in the aorta model.

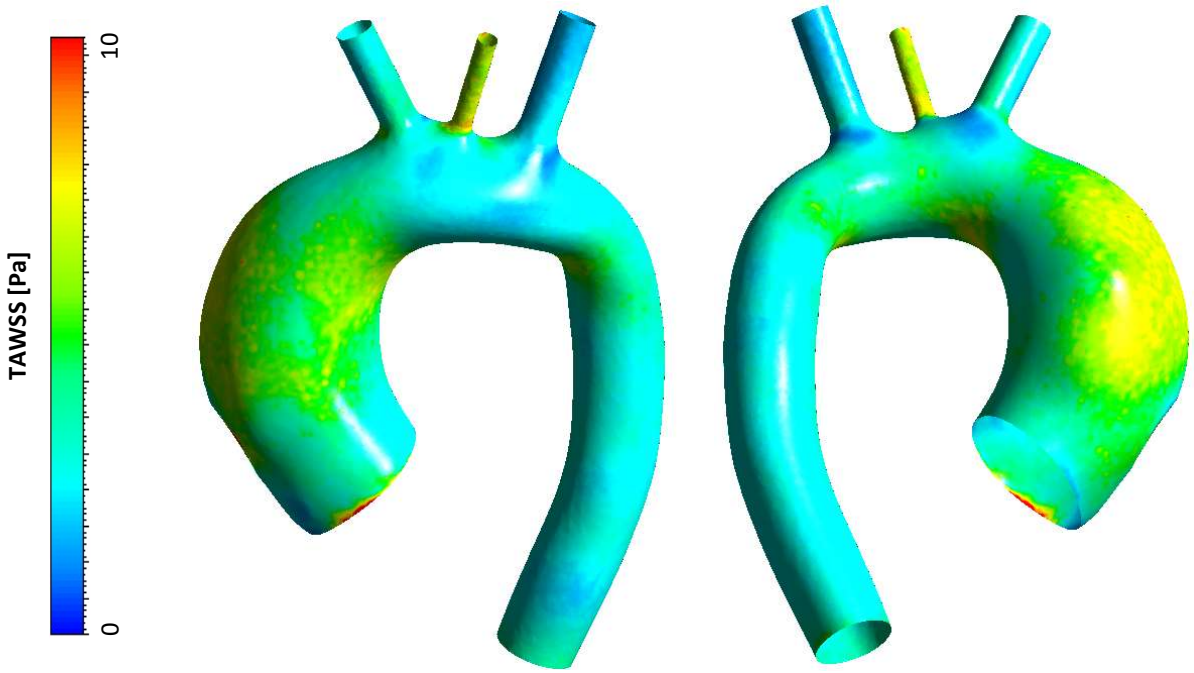

Figure 4.19. TAWSS distribution in the aorta model.

Post-intervention

WSS distribution in the arterial wall and PET graft is shown in **Figure 4.20**, at systolic peak. Maximum value of WSS occurred in the ascending tract (WSS = 29 Pa) next to the inlet section. In the descending aorta, in the intrados, a maximum value of WSS = 20.5 Pa was observed.

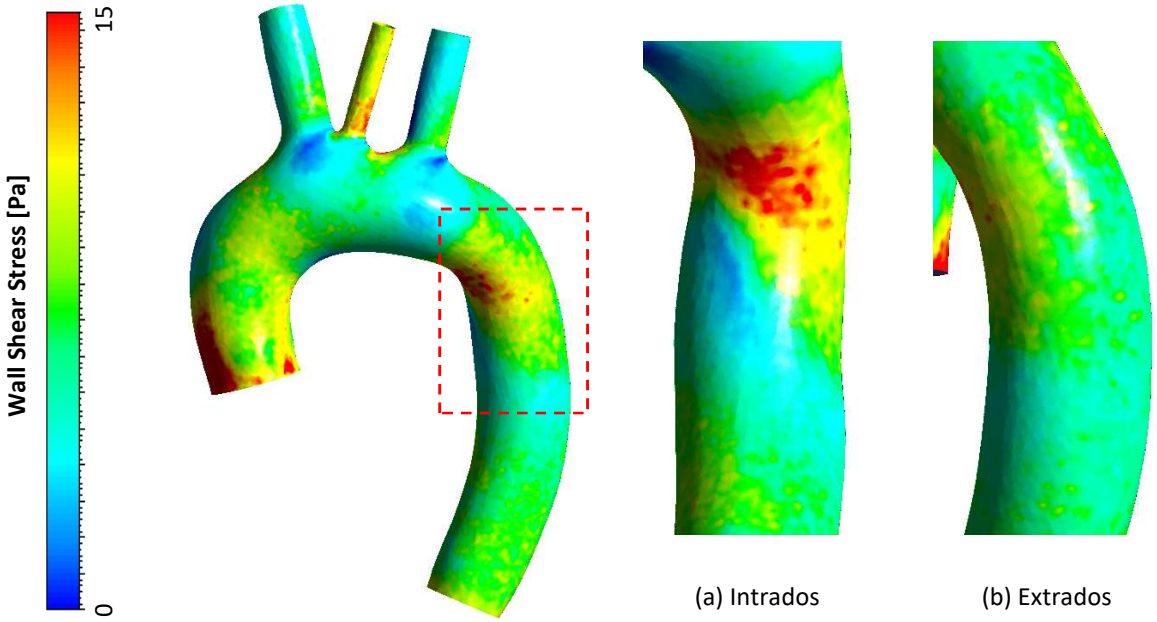

Figure 4.20. Wall shear stress (WSS) acting on the arterial wall at systolic peak. On the right side, a zoom-in (red box) of the WSS distribution on the intrados (a) and extrados (b) of the descending aorta.

OSI distribution is reported in **Figure 4.21**. Significantly lower value of OSI were obtained, compared to the distribution found in the pre-intervention model. Maximum value of OSI (0.489) occurred in the intrados of the aortic arch, downstream the suture site. In the descending aorta, a maximum value of OSI = 0.35 was observed, located in the area of fluid detachment. These areas are the riskiest in terms of aneurysm reformation.

TAWSS distribution in the model is shown in **Figure 4.22**. In the ascending aorta, high values of TAWSS (>10 Pa) were observed at inlfow. In the descending aorta, an average value of 2-4 Pa was observed, with a maximum value of TAWSS = 7 Pa, in the intrados, proximal to the arch.

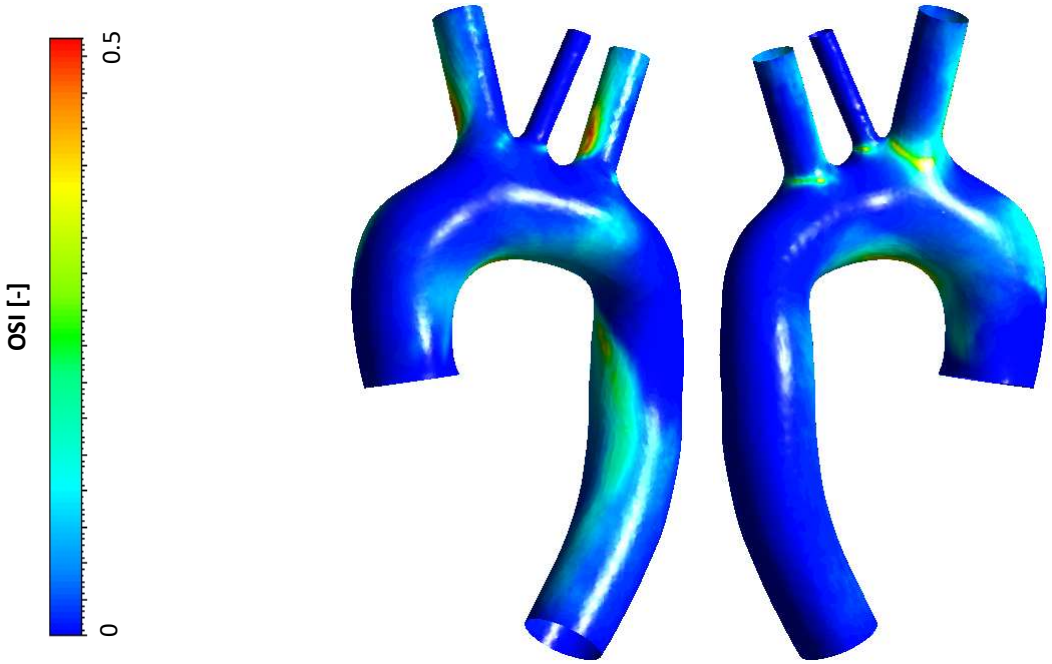

Figure 4.21. Oscillatory shear index (OSI) distribution in the aorta model.

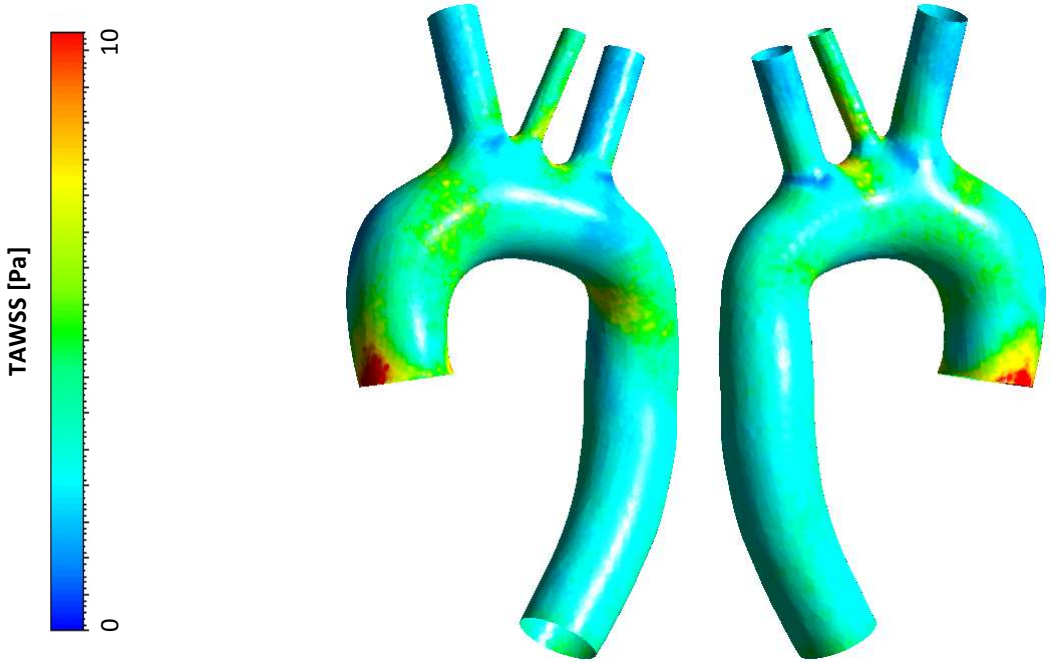

Figure 4.22. TAWSS distribution in the aorta model.

4.5.3 Strain and intramural stress

Pre-intervention

Results obtained from the solution of the solid domain Ω_s in the FSI analysis are herein reported (**Figure 4.23**). Wall displacement ($\boldsymbol{u}$), principal strain (ε_1) and principal stress (σ_1) were considered. Maximum of each considered quantity occurred at late systole (t = 0.34 s), at the intrados of the ascending aorta, consistently with literature works [43][38]. Maximum values of $\boldsymbol{u} = 4.53$ mm, $\varepsilon_1 = 0.185$ and $\sigma_1 = 299.15$ kPa were found.

In the descending aorta the maximum value of wall displacement occurred at the extrados ($\boldsymbol{u} =$ 3.07 mm). Strain and stress assumed average value of $\varepsilon_1 = 0.053$ and $\sigma_1 = 92.5$ kPa. No intensification area was observed.

A comparison between the undeformed configuration and the maximum stressed configuration is provided in **Figure 4.24**.

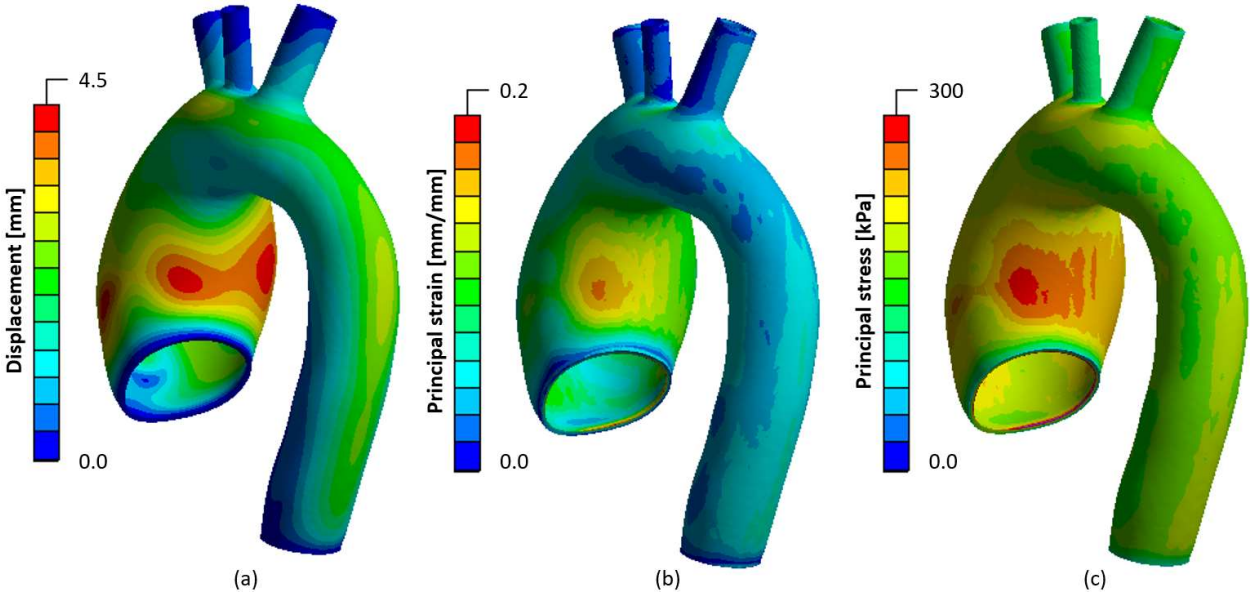

Figure 4.23. From left to right, displacement of the wall (a), principal strain (b) and principal stress (c) computed.

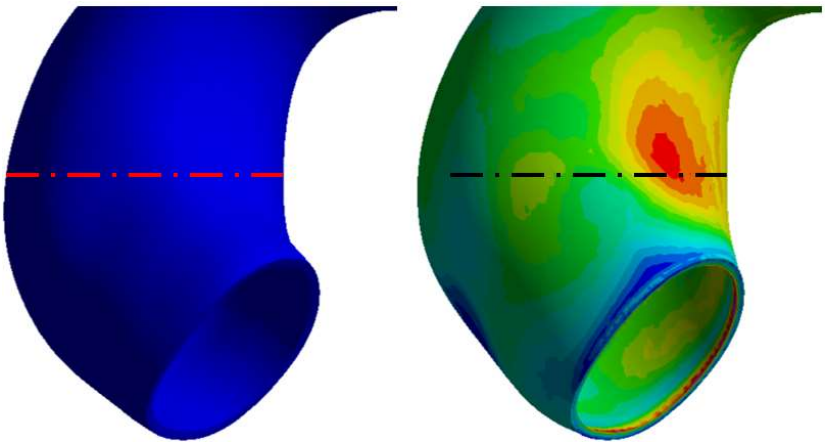

Figure 4.24. Comparison between undeformed (left) and maximum stressed (right) configuration. A dashed line (length = undeformed diameter) is exploited to highlight the deformation that occurs.

Post-intervention

Displacement ($\boldsymbol{u}$), principal strain (ε_1) and principal stress (σ_1) of the solid domain Ω_s obtained from FSI analysis are herein reported (**Figure 4.25**). Maximum of each quantity occurred at late systole (t = 0.38 s), as for the pre-intervention model.

Displacement maximum value, $\boldsymbol{u} = 3.1$ mm, occurred at the extrados of the descending aorta and along the arch (between BCA and LCCA) and was null in the tract where the PET graft was located.

Strain was almost null along the graft and assumed a maximum value $\varepsilon_1 = 0.143$ at the intrados of the aortic arch. Due to the higher stiffness of the graft ($E_{graft} \sim 10 E_{wall}$), it basically transmitted the boundary condition of no displacement to the native aorta tract.

Stress is homogeneous over the whole domain (~100 kPa), except for the graft suture site, where it sharply increases (**Figure 4.26**). In correspondence of the junction between the PET graft and the native vessel, a maximum value of $\sigma_1 = 516$ kPa were found. Intensification of stresses is local and occurs along the suture line, due to the change in the compliance mismatch (different stiffness).

Comparison between undeformed and maximum stressed configuration is shown in **Figure 4.27**.

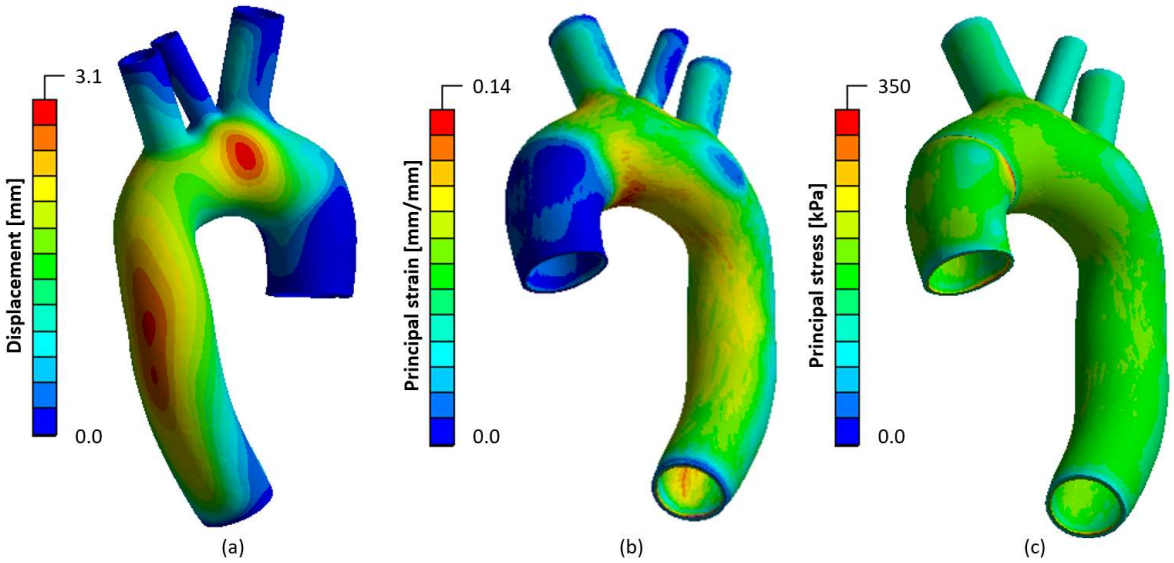

Figure 4.25. From left to right, displacement of the wall (a), principal strain (b) and principal stress (c) computed.

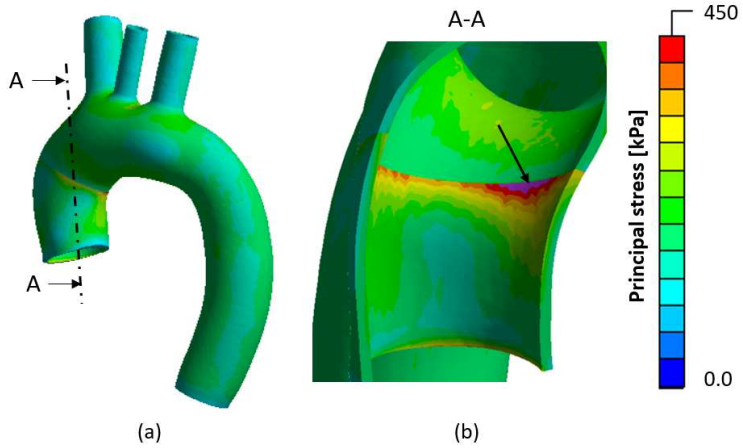

Figure 4.26. Section of the ascending aorta, showing the intensification of stress that occur along the suture line. The arrow in (b) points to the area where stress is maximum (516 kPa).

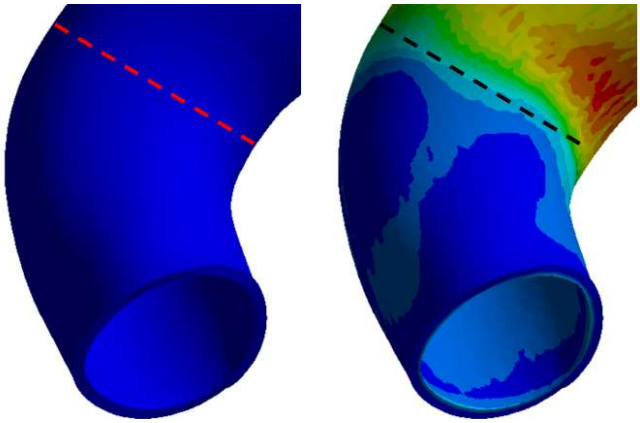

Figure 4.27. Comparison between undeformed (left) and maximum stressed (right) configuration. A dashed line (length = undeformed diameter) is exploited to highlight the deformation that occurs.

4.5.4 Focus on the descending aorta

A *t*-test was performed to compare results obtained from the two FSI simulations and CFD simulations. Comparison was made between population of systolic peak WSS, TAWSS and OSI for the pre and post intervention models. Two regions of the model were considered (**Figure 4.28**): the descending aorta and the proximal descending aorta.

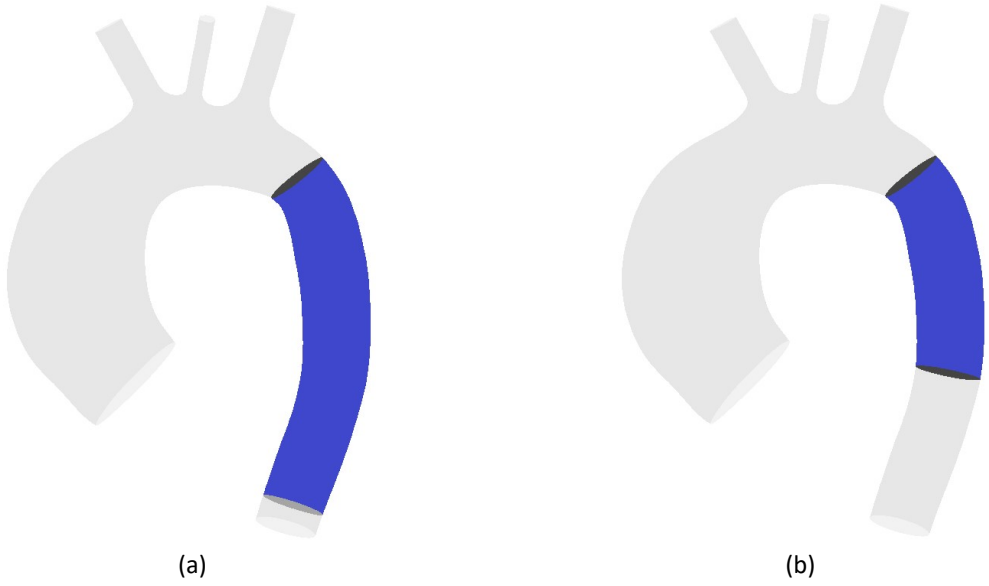

Figure 4.28. Regions where WSS, TAWSS and OSI where compared between simulations. From left to right, the entire aorta (a), the whole descending aorta (b) and proximal descending aorta (c).

Comparison in the descending aorta showed a statistically significant difference in distribution of WSS at systolic peak ($p<0.001$) obtained with FSI analysis, with higher WSS in the post-intervention model (**Figure 4.29**). No difference was observed between the two population in CFD simulations.

Both in FSI and CFD simulations, a marked difference ($p<0.01$) was observed in OSI distribution, with lower values of OSI predicted in the post-intervention model.

TAWSS obtained from FSI simulation showed no significant difference, while the difference was marked in TAWSS computed with CFD ($p<0.0001$). Higher TAWSS were observed in the post-intervention case.

In the proximal descending aorta (**Figure 4.30**), systolic WSS distribution differed ($p<0.05$) between pre and post-intervention FSI models. Higher WSS were obtained in the post-intervention case. No difference was observed in CFD model WSS distributions.
OSI distribution differed in both FSI ($p<0.05$) and CFD ($p<0.01$) models, with lower value of OSI in the post-intervention case.
No significant difference was observed between the pre and post-intervention TAWSS in the FSI models, while a marked difference was observed in CFD models ($p<0.0001$), with higher TAWSS in the post-intervention case.

Comparison with 4D flow

WSS in the descending aorta were computed also with the 4D flow postprocessing MATLAB™ tool developed by our group, to be compared with results from FSI. In the presurgical case, an average and a maximum WSS equal to 0.99 Pa and 1.34 Pa respectively were found, in the descending aorta. In the postsurgical case average and maximum WSS were 1.47 Pa and 2.45 Pa respectively.
WSS computed with 4D flow resulted strongly underestimated with respect to FSI simulation values. In the pre-intervention FSI model, an average WSS = 5.4 Pa and a maximum WSS = 9.2 Pa were found. In the post-intervention FSI model, an average WSS = 7.1 Pa and a maximum WSS = 10.3 Pa were found. These values are compatible with other literature works [43][52]. A comparison between 4D flow results and FSI results is given in **Table 4.3**.

	Pre-intervention		**Post-intervention**	
	WSS mean	WSS max	WSS mean	WSS max
4D flow	0.99	1.34	1.47	2.45
FSI solution	5.4	9.2	7.1	10.6

Table 4.3. Average and maximum value of WSS (given in Pa), measured in the descending aorta with the 4D flow analysis and FSI model.

The increase of WSS in the post-surgical case was observed with both approaches, however it was much more marked with 4D flow (48% and 81% for mean and maximum WSS respectively) than in the FSI model (31% and 15% for mean and maximum WSS respectively).

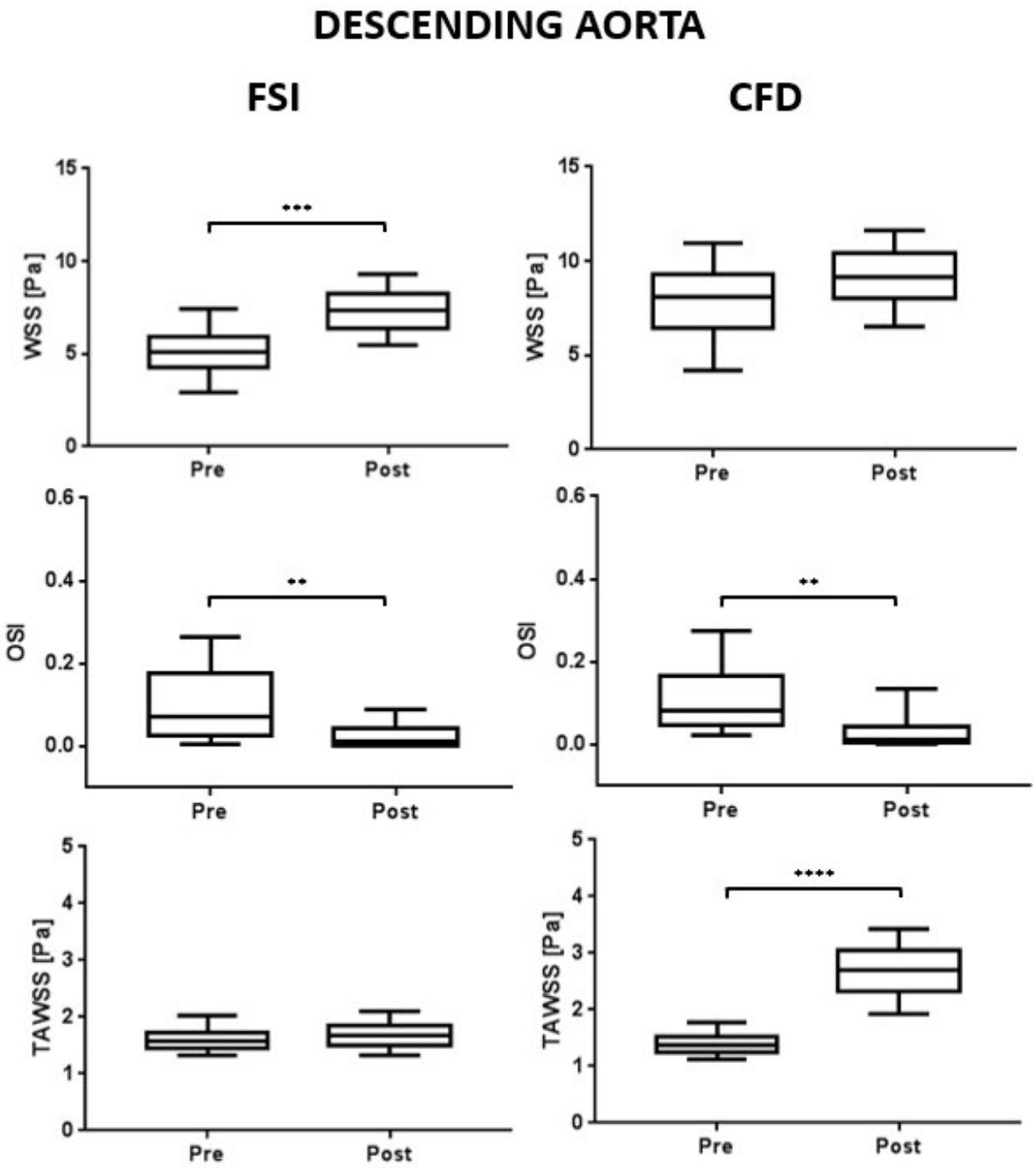

Figure 4.29. Comparison between percentiles population of systolic peak wall shear stress (WSS), oscillatory shear index (OSI) and time averaged WSS (TAWSS) obtained from the pre and post-intervention model of the descending aorta. On the left column, results from FSI analysis are compared, on the right column results from CFD are compared. Asterisks indicate the *p*-value: * = $p<0.05$, ** = $p<0.01$, *** = $p<0.001$ and **** = $p<0.0001$. Dataset of t-test results is reported in **Appendix**.

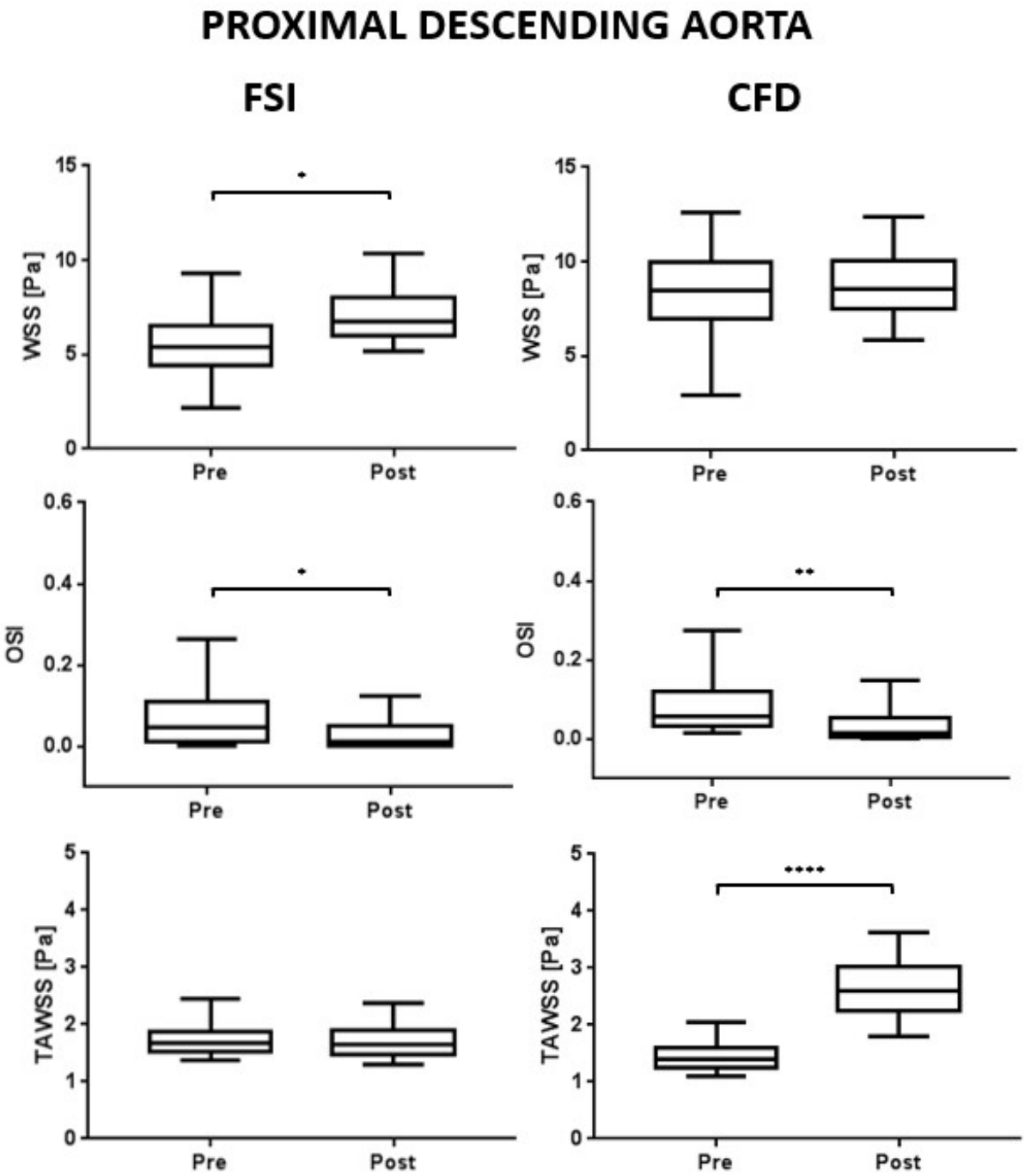

Figure 4.30. Comparison between percentiles population of systolic peak wall shear stress (WSS), oscillatory shear index (OSI) and time averaged WSS (TAWSS) obtained from the pre and post-intervention model of the proximal descending aorta. On the left column, results from FSI analysis are compared, on the right column results from CFD are compared. Asterisks indicate the *p*-value: * = $p<0.05$, ** = $p<0.01$, *** = $p<0.001$ and **** = $p<0.0001$. Dataset of t-test results is reported in **Appendix**.

4.6 Conclusions

In this chapter, the results obtained from numerical simulations were reported. Herein, a recap of the main achievements and their relevance is provided. A further discussion will be done in the next chapter (**Chapter 5**).

- *Mesh quality*: a mesh with a good mesh quality was generated both for the fluid and the solid domain. Sensitivity of the results to the mesh was tested and independency was achieved. A good quality of the grid and independency of the results are fundamental for the stability of numerical solver and the reliability of results.
- *Sensitivity to inlet boundary condition*: the comparison of three different boundary conditions, showed that only the patient specific inlet velocity was able to reproduce the hemodynamic pattern observed in 4D flow.
- *Solution method, FSI v. CFD*: the FSI model is the only one capable to properly reproduce velocity distributions (comparing it to 4D flow) along the whole aorta. CFD shows a marked difference (especially in descending aorta) and tend to overestimate velocities.
- *FSI, pre v. post-operation*: the comparison between the presurgical and postsurgical configuration showed an increase in velocity and systolic WSS, especially in the descending aorta (in agreement with clinical results), identifying it as a risky region for TAA reformation.
- *WSS, 4D flow v. FSI*: in both cases, WSS was significantly higher in the postsurgical case. However, values obtained from 4D flow were significantly lower than FSI and the difference pre v. post showed a very different trend, making 4D flow results unreliable.
- *Arterial wall biomechanics*: a significant intensification of stress was observed in the post-intervention case along the suture site, due to the compliance mismatch caused by the graft. In general, strain and stress distribution was significantly different in the post-surgical case. Only the FSI model could provide information regarding the wall biomechanics.

Chapter 5
Discussion and conclusions

Chapter summary

In this last chapter, the results presented in the previous chapter will be discussed. The reliability of the approach developed, the novelty aspects of this work and its limitations will be stressed. Finally, possible suggestions for the developments of the work will be given.

5.1 Discussion

In this thesis work an innovative numerical approach was developed for the assessment of the hemodynamics in patients operated for aTAA with VSR technique. Fluid-structure interaction simulations were performed on a patient specific geometry, to proper capture the coupling between native arterial wall, PET graft and blood. Simulations exploited patient specific inflow boundary conditions, extracted from 4D flow data. The aim of this work was to develop a reliable model to evaluate the alteration caused by the implantation of a synthetic graft, comparing a pre-intervention and a post-intervention model. In the following sections the results that were obtained will be discussed.

5.1.1 Reliability of results

The FSI results were compared with the available data from 4D flow analysis (accomplished in MATLAB™ and postprocessed in Paraview 5.7.0) and with clinical measurements, to evaluate the goodness of the numerical results.

FSI v. 4D flow numerical algorithm

Velocity contours were extracted on the same planes from the velocity field obtained with FSI simulation and 4D flow analysis. Three planes were considered in the ascending aorta and three planes in the descending aorta.

Quantitative comparison, achieved with an ANOVA, revealed no significant difference (p-value >0.05) between the FSI and 4D flow velocity distribution, furthermore the qualitative comparison of velocity patterns showed similar distribution for both pre and post-intervention model. In the ascending aorta a skewed velocity profile was found, with peaks were located in the extrados. In the descending aorta the profile was smoother.

Streamlines in the fluid domain were qualitatively compared. In the pre-intervention model, vortical structures formed in the FSI model in the same location (the intrados of ascending aorta) as 4D flow; in the post-intervention model the same sustained flow pattern was observed (straight streamlines).

Thus, the FSI models developed were able to capture properly the hemodynamics of the patient, with same velocity magnitude and distribution, in a physiological pressure operative range.

The comparison between values of WSS computed with the 4D flow analysis and the FSI simulation showed a marked difference both in the pre and postsurgical case, with lower WSS in the 4D flow case. In both approaches, WSS was higher after the surgery, however the increase was much more marked with 4D flow. These differences suggest that, due to its poor spatial resolution, the 4D flow analysis is not able to properly capture the wall velocity gradient and thus WSS results lower. To get a more precise measure of WSS, spatial resolution of 4D flow should be improved, otherwise numerical models such as FSI, combined with 4D flow data, represent a useful tool to access this measure.

CFD v. 4D flow numerical algorithm

The ANOVA revealed a significant discrepancy in distal ascending aorta and in the planes in descending aorta. The *p*-value resulting from the comparison of velocity distributions between CFD and 4D flow was always <0.001 for the pre-intervention model, with CFD overestimating the velocity values. In the post-intervention model, a less marked statistical difference ($p<0.05$) was observed in the descending aorta, still with higher velocities in the CFD model. Qualitative results comparison (contours and streamlines) showed similar flow pattern, with higher velocities in the CFD model, consistently with ANOVA results.

The accomplished results demonstrated that an FSI model is mandatory to simulate properly the hemodynamics in the aorta. The compliant action of the arterial wall cannot be neglected, otherwise velocities get overestimated, and the related results (WSS, OSI, TAWSS) are not reliable too. This is also proven by the comparison between systolic WSS distribution prior and after surgery: while FSI model is able to capture the increase in WSS magnitude, no statistical difference is observed between the pre and post WSS distributions obtained from CFD. Thus, a CFD approach, that is based on the assumption of rigid wall, is an oversimplified model for simulations of the aorta.

Discrepancy between velocity computed from CFD simulations are less marked in the post-intervention case. This is due to the fact that the graft implanted for the substitution of the ascending aorta is ~10 times stiffer than the native wall and thus, rigid wall assumption is reasonable, at least for that tract.

5.1.2 Novelty aspects

Various studies can be found in literature, exploiting FSI modeling approach to study the hemodynamics in the aorta, in presence of an aneurysm [38][43][46][48][50]. However, simplified geometry or boundary conditions are generally adopted. Furthermore, the focus of these studies is only on the pathologic configuration (i.e. before the aneurysm is treated); to the best of author's knowledge, a complete FSI model that compares the pathologic and the post-VSR surgery configuration is still lacking.

Accordingly, this thesis work represents the first FSI model that investigates the alterations in blood fluid dynamics caused by the graft implantation. The set-up of the model was developed to reliably reproduce the operating condition of the patient's aorta. To achieve this purpose, patient specific boundary conditions were applied to a geometry reconstructed from MRA images. At the inlet, velocities extracted from PC-MRI dataset, were assigned and at the outlets WK3 models were tuned with patient's available clinical data (systolic and diastolic pressure). This represents the best combination of boundary conditions, according to [39], to replicate aortic hemodynamic.

Results from FSI were validated against 4D flow and compared with CFD. This comparison proved that only the FSI approach was able to properly replicate the aortic hemodynamic, while CFD results and oversimplified method, that may provide unreliable results. Furthermore, a sensitivity analysis of the inlet boundary conditions was performed to determine weather, a flat, a parabolic or a patient specific velocity profile is the best option for aortic hemodynamic simulations.

Inlet boundary conditions

The comparison between the streamlines in the ascending aorta clearly showed that only the patient specific profile is able to reproduce a hemodynamics similar to 4D flow analysis. Vortical structures, visible in the intrados of the ascending segment in the 4D flow, formed in the patient specific profile CFD, while they didn't form neither in the flat profile nor in the parabolic profile CFD. Furthermore, the skewness of the inlet velocity profile and its angle were

reproduced only by the patient specific CFD. This suggest that both types of boundary conditions (flat and parabolic) are oversimplifications, that don't represent correctly the aortic hemodynamic:

Pre-intervention v. post-intervention

As previous studies conducted with 4D flow analysis pointed out [24][76], velocities in the descending aorta results higher after VSR of the ascending tract. This is due to the fact that the PET graft (that is much stiffer than native tissue) doesn't accomplish to the compliant function of the aorta and consequently, blood has a lower energy loss. When blood flows in the native aorta, part of its energy is absorbed in the filling of the compliant wall.

Focusing on the descending aorta, a *t*-test was performed between WSS, OSI and TAWSS distributions prior and after surgery. Clinically, it has been observed that the descending aorta is the segment where most frequently TAAs reform after VSR. The hemodynamic quantities that were considered are related to the atherogenic process starting: the magnitude of WSS and the change in time of its direction affect the endothelial cell of the wall, that deteriorate and trigger the atherogenic process. [25][26].

FSI models revealed a significant difference between pre and post-operation WSS distribution (p <0.001, higher WSS after surgery) and OSI distribution (p <0.01, lower OSI after surgery). No significant difference was observed for TAWSS distribution. The segment immediately after the aortic arch is the most affected by the high curvature of the vessel; there higher WSS values were found, compared to the whole descending aorta distribution, suggesting that proximal descending aorta is the most stressed segment

The significant lowering of OSI values suggest that a more physiological flow rate has been restored after the surgery, with no disturbed flow regions. However, WSS at systolic peak result higher and thus, the risk of atherogenic triggering is not negligible.

Aortic wall biomechanics

The solutions of the structural domain were compared in terms of maximum values and distribution. Displacement and strain were found to be grater in the pre-intervention case (4.53 mm and 18.5% respectively), in the intrados of the ascending aorta. Other works [38][43]

identified the intrados of the ascending aorta (in presence of an aTAA) as the location where maximum strain occurred.
In the post-intervention, maximum displacement (3.1 mm) and strain (14.3%) were found in the extrados and intrados of the descending aorta respectively. After the surgery the PET graft causes a marked change in strain and displacement distribution: due to its greater stiffness, the graft segment deformation is almost null, compared to the deformation of the native vessel and the aorta starts deforming only downstream the suture site.

Wall stress (computed as maximum principal stress) assumed similar average values in the pre and post-intervention model: 92.5 and 100 kPa respectively. Maximum stress occurred in the intrados of ascending aorta both in the presurgical model (consistently with literature [38][43]) and in the postsurgical, in which were located along the graft suture site connecting the aortic arch. A significant difference was observed in terms of maximum stress: while in the pre-intervention case $\sigma_{1,max} = 299$ kPa, in the post intervention case $\sigma_{1,max} = 516$ kPa. The sharp increase of wall stress is due to the compliance mismatch caused by the PET graft. Compliance mismatch in arteries that present suture sites causes oscillation of stress in the arterial wall, with peaks that are more pronounced for greater change in stiffness [77]. The intensification region may represent a risky spot for the starting of a TAA.

Information on the aortic wall biomechanics can be obtained only through an FSI model. Both 4D flow and CFD simulation provide results related to the hemodynamics, undoubtedly useful, but say nothing of the mechanics of the wall. The only way to achieve a complete characterization of the vessel biomechanics is through an FSI model.

5.1.3 Limitations

The FSI model developed is affected by some limitations and approximations. These set basis for further development and optimization. The main aspects to be improved are the following:

- *Arterial wall*: the wall of the aorta was modeled as an isotropic elastic material, with a Young's Modulus $E = 1.5$ MPa [63]. Despite the fact that this is common in FSI modeling of human vessels [38][52], it's well known that arterial tissue has a hyperelastic behavior, so a more complete constitutive model should be adopted.

- *Blood as a fluid*: blood is not a fluid, but a suspension of particles (RBCs, WBCs and platelets) in plasma. Treating blood as a Newtonian fluid is an approximation, however, due to the high shear rate in large vessel, this assumption is reasonable. If the model should be expanded (e.g. extending the supra-aortic branches, including coronaries…), blood modeling should be discussed.
- *Computational cost*: the simulation time of an FSI model is significantly higher compared to a simpler CFD model (~10 days v. 2 days on 24 cores respectively). To contain the cost of the simulation, some approximations were required, for example on the material properties.
- *Boundary conditions (fluid)*: according to [39] the boundary conditions applied to the fluid domain represent the best combination to reproduce patient specific hemodynamics in the aorta. However, the average flow rate in each aortic branch, used to compute the Windkessel parameter, was derived as a fraction (in agreement with [78]) of the inlet flow rate; an improvement could be using 4D flow analysis to measure it.
- *Boundary condition (solid)*: for the structural domain, a kinematic boundary condition (no displacement) was adopted on each extremity. An alternative could be using a fixed boundary condition for the aortic inlet and allow radial displacement at the other outlets. It should be noted that to adopt a patient specific velocity profile as inlet boundary conditions, the coordinates of the inlet must not vary, so the inlet must be fixed.
- *Patient pool*: in this work of thesis, the FSI approach was exploited to model one single patient. A wider pool is necessary to increase the interest that this approach may have in clinical practice.

5.2 Conclusions

The FSI model that was developed in this thesis work provided a comprehensive insight into the biomechanics of a pathologic and a VSR treated aorta. The model was able to reproduce the operative condition of the vessel and permitted to investigate both fluid dynamics and structural aspects.

The comparison of the FSI model with a CFD (with same boundary condition) demonstrated that, in order to properly capture the hemodynamics of the vessel a simple CFD is not sufficient

and provides unreliable results. Furthermore, comparing three different boundary conditions – plug, parabolic, patient specific velocity profile – demonstrated that the ability to reproduce properly the aortic fluid dynamics doesn't depend on the boundary conditions only, but also on the type of modeling that is adopted.

The current work set the basis to a promising methodology for the optimization of surgical procedure for the treatment o aTAAs, since it is able to predict – for a specific patient – regions where the fluid dynamics results altered and consequently the atherogenic process will most likely take place. A further development for this study may consist in reproduce this modeling on a wider pool of patients and investigate the effect that different graft (different length, stiffness…) induce.

Appendix

	4d flow	FSI	CFD
		Plane 1	
10th percentile	0.163	0.178	0.218
Median	0.440	0.429	0.459
90th percentile	0.788	1.142	1.172
		Plane 2	
10th percentile	0.172	0.117	0.122
Median	0.451	0.299	0.374
90th percentile	0.709	0.863	0.816
		Plane 3	
10th percentile	0.190	0.198	0.336
Median	0.356	0.377	0.492
90th percentile	0.627	0.428	0.511
		Plane 4	
10th percentile	0.197	0.047	0.596
Median	0.555	0.718	0.936
90th percentile	0.716	0.813	1.055
		Plane 5	
10th percentile	0.185	0.052	0.327
Median	0.517	0.616	0.816
90th percentile	0.684	0.750	0.977
		Plane 6	
10th percentile	0.276	0.060	0.378
Median	0.530	0.583	0.789
90th percentile	0.662	0.697	0.925

Table I. Comparison of the velocity (reported in m/s) populations in the pre-intervention model (results of ANOVA related to **Figure 4.9**).

	4d flow	FSI	CFD
		Plane 1	
10th percentile	0.162	0.487	0.514
Median	0.592	0.907	0.920
90th percentile	1.292	1.197	1.208
		Plane 2	
10th percentile	0.236	0.235	0.480
Median	0.551	0.841	0.869
90th percentile	1.145	1.073	1.094
		Plane 3	
10th percentile	0.252	0.082	0.358
Median	0.672	0.731	0.788
90th percentile	0.970	0.857	0.898
		Plane 4	
10th percentile	0.214	0.044	0.505
Median	0.682	0.755	0.896
90th percentile	0.970	0.880	1.022
		Plane 5	
10th percentile	0.212	0.035	0.421
Median	0.529	0.698	0.849
90th percentile	0.894	0.822	0.968

		Plane 6	
10th percentile	0.199	0.039	0.440
Median	0.550	0.662	0.816
90th percentile	0.888	0.762	0.923

Table II. Comparison of the velocity (reported in m/s) populations in the post-intervention model (results of ANOVA related to **Figure 4.13**).

	FSI		**CFD**	
	WSS pre	**WSS post**	**WSS pre**	**WSS post**
10th percentile	2.943	5.495	4.220	6.530
Median	5.132	7.358	8.105	9.184
90th percentile	7.425	9.295	10.96	11.63
	OSI pre	**OSI post**	**OSI pre**	**OSI post**
10th percentile	0.0052	0.0004	0.0227	0.0021
Median	0.0729	0.0132	0.0822	0.0116
90th percentile	0.2648	0.0907	0.2751	0.1362
	TAWSS pre	**TAWSS post**	**TAWSS pre**	**TAWSS post**
10th percentile	1.329	1.332	1.119	1.928
Median	1.567	1.667	1.378	2.693
90th percentile	2.021	2.098	1.775	3.417

Table III. Comparison of the WSS (Pa), OSI (-) and TAWSS (Pa) populations in the descending aorta: pre v. post model (results related to **Figure 4.29**).

	FSI		**CFD**	
	WSS pre	**WSS post**	**WSS pre**	**WSS post**
10th percentile	2.185	5.192	4.220	6.530
Median	5.410	6.744	2.953	5.814
90th percentile	9.289	10.330	12.63	12.40
	OSI pre	**OSI post**	**OSI pre**	**OSI post**
10th percentile	0.0024	0.0004	0.0166	0.0026
Median	0.0454	0.0115	0.0559	0.0143
90th percentile	0.2639	0.1236	0.2744	0.1471
	TAWSS pre	**TAWSS post**	**TAWSS pre**	**TAWSS post**
10th percentile	1.375	1.294	1.105	1.811
Median	1.665	1.662	1.390	2.592
90th percentile	2.440	2.375	2.040	3.633

Table IV. Comparison of the WSS (Pa), OSI (-) and TAWSS (Pa) populations in the proximal descending aorta: pre v. post model (results related to **Figure 4.30**).

Bibliography

[1] J. D. Humphrey and A. D. McCulloch, "The Cardiovascular System — Anatomy, Physiology and Cell Biology," *Biomech. Soft Tissue Cardiovasc. Syst.*, no. Lv, pp. 1–14, 2003, doi: 10.1007/978-3-7091-2736-0_1.

[2] J. G. Betts *et al.*, "Fluids and Transport: The Cardiovascular System," in *Anatomy & Physiology*, 2015, pp. 783–974.

[3] E. Ladich, K. Yahagi, M. E. Romero, and R. Virmani, "Vascular diseases: aortitis, aortic aneurysms, and vascular calcification," *Cardiovasc. Pathol.*, vol. 25, no. 5, pp. 432–441, 2016, doi: 10.1016/j.carpath.2016.07.002.

[4] E. Earl and H. Mohammadi, "Biomechanics of Human Blood," *Biomechanics*, pp. 1–17, 2019, doi: 10.5772/intechopen.78305.

[5] J. D. Kelley and J. V. Ashurst, "Anatomy, Thorax, Aortic Arch," *StatPearls*, 2019.

[6] D. Case, J. Seinfeld, Z. Folzenlogen, and D. Kumpe, "Anomalous Right Vertebral Artery Originating from the Aortic Arch Distal to the Left Subclavian Artery: A Case Report and Review of the Literature.," *J. Vasc. Interv. Neurol.*, vol. 8, no. 3, pp. 21–214, 2015.

[7] G. S. Kassab, "Biomechanics of the cardiovascular system: The aorta as an illustratory example," *J. R. Soc. Interface*, vol. 3, no. 11, pp. 719–740, 2006, doi: 10.1098/rsif.2006.0138.

[8] "World Health Organization." [Online]. Available: https://www.who.int/health-topics/cardiovascular-diseases/#tab=tab_1.

[9] K. H. Chau and J. A. Elefteriades, "Natural history of thoracic aortic aneurysms: Size matters, plus moving beyond size," *Prog. Cardiovasc. Dis.*, vol. 56, no. 1, pp. 74–80, 2013, doi: 10.1016/j.pcad.2013.05.007.

[10] J. I. E. Hoffman and S. Kaplan, "The incidence of congenital heart disease," *J. Am. Coll. Cardiol.*, vol. 39, no. 12, pp. 1890–1900, 2002, doi: 10.1016/S0735-1097(02)01886-7.

[11] M. L. Brown *et al.*, "Coarctation of the aorta: Lifelong surveillance is mandatory following surgical repair," *J. Am. Coll. Cardiol.*, vol. 62, no. 11, pp. 1020–1025, 2013, doi: 10.1016/j.jacc.2013.06.016.

[12] F. J. Criado, "Aortic dissection: A 250-year perspective," *Texas Hear. Inst. J.*, vol. 38, no. 6, pp. 694–700, 2011.

[13] I. Kronzon and P. A. Tunick, "Aortic atherosclerotic disease and stroke," *Circulation*, vol. 114, no. 1, pp. 63–75, 2006, doi: 10.1161/CIRCULATIONAHA.105.593418.

[14] I. I. ABUBAKAR, T. TILLMANN, and A. BANERJEE, "Global, regional, and national age-sex specific all-cause and cause-specific mortality for 240 causes of death, 1990-2013: a systematic analysis for the Global Burden of Disease Study 2013," *Lancet (London, England)*, vol. 385, no. 9963, pp. 117–171, 2015, doi: 10.1016/S0140-6736(14)61682-2.Global.

[15] S. Verma and S. C. Siu, "Aortic dilatation in patients with bicuspid aortic valve," *N. Engl. J. Med.*, vol. 370, no. 20, pp. 1920–1929, 2014, doi: 10.1056/NEJMra1207059.

[16] R. Mahadevia *et al.*, "Bicuspid Aortic Cusp Fusion Morphology Alters Aortic 3D Outflow Patterns, Wall Shear Stress and Expression of Aortopathy," vol. 129, no. 6, pp. 673–682, 2015, doi: 10.1161/CIRCULATIONAHA.113.003026.Bicuspid.

[17] V. van de Pol, K. Kurakula, M. C. DeRuiter, and M. J. Goumans, "Thoracic aortic aneurysm development in patients with bicuspid aortic valve: What is the role of endothelial cells?," *Front. Physiol.*, vol. 8, no. NOV, pp. 1–14, 2017, doi: 10.3389/fphys.2017.00938.

[18] A. Saeyeldin, M. Zafar, and J. A. Elefteriades, "Natural history of aortic root aneurysms in Marfan syndrome," *Ann. Thorac. Surg.*, vol. 6, no. 6, pp. 625–632, 2017.

[19] M. Gaudino, C. Lau, M. Munjal, D. Avgerinos, and L. N. Girardi, "Contemporary outcomes of surgery for aortic root aneurysms: A propensity-matched comparison of valve-sparing and composite valve graft replacement," *J. Thorac. Cardiovasc. Surg.*, vol. 150, no. 5, pp. 1120-1129.e1, 2015, doi: 10.1016/j.jtcvs.2015.07.015.

[20] T. E. David and C. M. Feindel, "An aortic valve-sparing operation for patients with aortic incompetence and aneurysm of the ascending aorta," *J. Thorac. Cardiovasc. Surg.*, vol. 103, no. 4, pp. 617–622, 1992, doi: 10.1016/s0022-5223(19)34942-6.

[21] E. M. Isselbacher, "Thoracic and abdominal aortic aneurysms," *Circulation*, vol. 111, no. 6, pp. 816–828, 2005, doi: 10.1161/01.CIR.0000154569.08857.7A.

[22] R. De Paulis *et al.*, "Long-term results of the valve reimplantation technique using a graft with sinuses," *J. Thorac. Cardiovasc. Surg.*, vol. 151, no. 1, pp. 112–119, 2016, doi: 10.1016/j.jtcvs.2015.08.026.

[23] R. K. V. Sethi, A. J. Henry, N. D. Hevelone, S. R. Lipsitz, M. Belkin, and L. L. Nguyen, "Impact of hospital market competition on endovascular aneurysm repair adoption and outcomes," *J. Vasc. Surg.*, vol. 58, no. 3, pp. 596–606, 2013, doi: 10.1016/j.jvs.2013.02.014.

[24] M. Gaudino *et al.*, "Aortic flow after valve sparing root replacement with or without neosinuses reconstruction," *J. Thorac. Cardiovasc. Surg.*, vol. 157, no. 2, pp. 455–465, 2019, doi: 10.1016/j.jtcvs.2018.06.094.

[25] J. M. Zhang, L. P. Chua, D. N. Ghista, S. C. M. Yu, and Y. S. Tan, "Numerical investigation and identification of susceptible sites of atherosclerotic lesion formation in a complete coronary artery bypass model," *Med. Biol. Eng. Comput.*, vol. 46, no. 7, pp.

689–699, 2008, doi: 10.1007/s11517-008-0320-4.

[26] D. N. Ku, D. P. Giddens, C. K. Zarins, and S. Glagov, "Pulsatile flow and atherosclerosis in the human carotid bifurcation. Positive correlation between plaque location and low and oscillating shear stress," *Arteriosclerosis*, vol. 5, no. 3, pp. 293–302, 1985, doi: 10.1161/01.atv.5.3.293.

[27] H. Meng, V. M. Tutino, J. Xiang, and A. Siddiqui, "High WSS or Low WSS? Complex interactions of hemodynamics with intracranial aneurysm initiation, growth, and rupture: Toward a unifying hypothesis," *Am. J. Neuroradiol.*, vol. 35, no. 7, pp. 1254–1262, 2014, doi: 10.3174/ajnr.A3558.

[28] D. B. Plewes and W. Kucharczyk, "Physics of MRI: A primer," *J. Magn. Reson. Imaging*, vol. 35, no. 5, pp. 1038–1054, 2012, doi: 10.1002/jmri.23642.

[29] G. Coppini, S. Diciotti, and G. Valli, *Bioimmagini*. 2001.

[30] J. P. Hornak, "Functional MRI of stimulus interference on auditory processing in normal listeners and tinnitus patients," 2015.

[31] C. J. Elkins and M. T. Alley, "Magnetic resonance velocimetry: Applications of magnetic resonance imaging in the measurement of fluid motion," *Exp. Fluids*, vol. 43, no. 6, pp. 823–858, 2007, doi: 10.1007/s00348-007-0383-2.

[32] J. Lotz, C. Meier, A. Leppert, and M. Galanski, "Cardiovascular flow measurement with phase-contrast MR imaging: Basic facts and implementation," *Radiographics*, vol. 22, no. 3, pp. 651–671, 2002, doi: 10.1148/radiographics.22.3.g02ma11651.

[33] M. Markl, A. Frydrychowicz, S. Kozerke, M. Hope, and O. Wieben, "4D flow MRI," *J. Magn. Reson. Imaging*, vol. 36, no. 5, pp. 1015–1036, 2012, doi: 10.1002/jmri.23632.

[34] C. Tang, D. D. Blatter, and D. L. Parker, "Accuracy of phase-contrast flow measurements in the presence of partial-volume effects," *J. Magn. Reson. Imaging*, vol. 3, no. 2, pp. 377–385, 1993, doi: 10.1002/jmri.1880030213.

[35] S. Nordmeyer *et al.*, "Flow-sensitive four-dimensional cine magnetic resonance imaging for offline blood flow quantification in multiple vessels: A validation study," *J. Magn. Reson. Imaging*, vol. 32, no. 3, pp. 677–683, 2010, doi: 10.1002/jmri.22280.

[36] A. Roldán-Alzate *et al.*, "In vivo validation of 4D flow MRI for assessing the hemodynamics of portal hypertension," *J. Magn. Reson. Imaging*, vol. 37, no. 5, pp. 1100–1108, 2013, doi: 10.1002/jmri.23906.

[37] G. Biglino, D. Cosentino, and S. Schievano, "Using 4D Cardiovascular Magnetic Resonance Imaging to Validate Computational Fluid Dynamics: A Case Study," *Front. Pediatr. 3*, 2015.

[38] R. Campobasso, F. Condemi, M. Viallon, P. Croisille, S. Campisi, and S. Avril, "Evaluation of Peak Wall Stress in an Ascending Thoracic Aortic Aneurysm Using FSI Simulations: Effects of Aortic Stiffness and Peripheral Resistance," *Cardiovasc. Eng.*

Technol., vol. 9, no. 4, pp. 707–722, 2018, doi: 10.1007/s13239-018-00385-z.

[39] S. Pirola *et al.*, "On the choice of outlet boundary conditions for patient-specific analysis of aortic flow using computational fluid dynamics," *J. Biomech.*, vol. 60, pp. 15–21, 2017, doi: 10.1016/j.jbiomech.2017.06.005.

[40] A. B. Fisher, S. Chien, A. I. Barakat, and R. M. Nerem, "Endothelial cellular response to altered shear stress," *Am. J. Physiol. - Lung Cell. Mol. Physiol.*, vol. 281, no. 3 25-3, pp. 529–533, 2001, doi: 10.1152/ajplung.2001.281.3.l529.

[41] M. Cibiş, *Haemodynamics of Large Vessels by Phase Contrast MRI*. 2016.

[42] A. D. Caballero and S. Laín, "A Review on Computational Fluid Dynamics Modelling in Human Thoracic Aorta," *Cardiovasc. Eng. Technol.*, vol. 4, no. 2, pp. 103–130, 2013, doi: 10.1007/s13239-013-0146-6.

[43] V. Mendez, M. Di Giuseppe, and S. Pasta, "Comparison of hemodynamic and structural indices of ascending thoracic aortic aneurysm as predicted by 2-way FSI, CFD rigid wall simulation and patient-specific displacement-based FEA," *Comput. Biol. Med.*, vol. 100, no. May, pp. 221–229, 2018, doi: 10.1016/j.compbiomed.2018.07.013.

[44] J. Donea, A. Huerta, and J. Ponthot, "Chapter 14: Arbitrary Lagrangian–Eulerian Methods," *Encycl. Comput.*, pp. 1–25, 2004.

[45] F. Cuomo, S. Roccabianca, D. Dillon-Murphy, N. Xiao, J. D. Humphrey, and C. A. Figueroa, "Effects of age-associated regional changes in human central artery mechanics on systemic hemodynamics revealed by computational modeling," *PLoS One*, vol. 12, no. 3, pp. 1–21, 2017, doi: 10.7302/Z24B2Z7Z.

[46] T. Khamdaeng and P. Terdtoon, "Regional pulse wave velocity and stress in aneurysmal arch-shaped aorta," *Biomed. Mater. Eng.*, vol. 29, no. 4, pp. 527–549, 2018, doi: 10.3233/BME-181007.

[47] R. Jayendiran, B. Nour, and A. Ruimi, "Fluid-structure interaction (FSI) analysis of stent-graft for aortic endovascular aneurysm repair (EVAR): Material and structural considerations," *J. Mech. Behav. Biomed. Mater.*, vol. 87, no. May, pp. 95–110, 2018, doi: 10.1016/j.jmbbm.2018.07.020.

[48] C. J. Drewe, L. P. Parker, L. J. Kelsey, P. E. Norman, J. T. Powell, and B. J. Doyle, "Haemodynamics and stresses in abdominal aortic aneurysms: A fluid-structure interaction study into the effect of proximal neck and iliac bifurcation angle," *J. Biomech.*, vol. 60, pp. 150–156, 2017, doi: 10.1016/j.jbiomech.2017.06.029.

[49] N. Xiao, J. Alastruei, and C. A. Figueroa, "A systematic comparison between 1-D and 3-D hemodynamicsin compliant arterial models," *Int. Journey Numer. methods Biomed. Eng.*, 2014.

[50] S. Lin, X. Han, Y. Bi, S. Ju, and L. Gu, "Fluid-structure interaction in abdominal aortic aneurysm: Effect of modeling techniques," *Biomed Res. Int.*, vol. 2017, 2017, doi: 10.1155/2017/7023078.

[51] P. Reymond, P. Crosetto, S. Deparis, A. Quarteroni, and N. Stergiopulos, "Physiological simulation of blood flow in the aorta: Comparison of hemodynamic indices as predicted by 3-D FSI, 3-D rigid wall and 1-D models," *Med. Eng. Phys.*, vol. 35, no. 6, pp. 784–791, 2013, doi: 10.1016/j.medengphy.2012.08.009.

[52] R. Savabi, M. Nabaei, S. Farajollahi, and N. Fatouraee, "Fluid structure interaction modeling of aortic arch and carotid bifurcation as the location of baroreceptors," *Int. J. Mech. Sci.*, vol. 165, no. July 2019, 2020, doi: 10.1016/j.ijmecsci.2019.105222.

[53] A. M. Robertson, A. Sequeira, and R. G. Owens, "Rheological models for blood," *Model. Simul. Appl.*, vol. 1, pp. 211–241, 2009, doi: 10.1007/978-88-470-1152-6_6.

[54] G. A. Holzapfel, T. C. Gasser, and R. W. Ogden, "A new constitutive framework for arterial wall mechanics and a comparative study of material models," *J. Elast.*, vol. 61, no. 1–3, pp. 1–48, 2000, doi: 10.1023/A:1010835316564.

[55] C.-Y. Liu, D. Chen, D. A. Bluemke, and W. G. Hundley, "Evolution of aortic wall thickness and stiffness with atherosclerosis: Long-term follow up from the Multi-Ethnic Study of Atherosclerosis (MESA)," *HHS Public Access*, vol. 69, no. 1, pp. 110–120, 2015, doi: 10.1016/j.socscimed.2009.04.010.Are.

[56] W. Karel van den Hengel, "Abdominal aortic wall thickness and compliance The possibilities to measure and the effect of variation in the analysis of aneurysms," *Blood*, no. April, 2008.

[57] B. A. Craven, E. G. Paterson, G. S. Settles, and M. J. Lawson, "Development and verification of a high-fidelity computational fluid dynamics model of canine nasal airflow," *J. Biomech. Eng.*, vol. 131, no. 9, pp. 1–11, 2009, doi: 10.1115/1.3148202.

[58] W. L. Oberkampf, "Verification and Validation in Computational Simulation," *2004 Transp. Task Force Meet.*, vol. 21, no. 3, pp. 359–367, 2004, doi: 10.1016/j.cma.2004.03.002.

[59] "ANSYS User Guide," 2016. .

[60] H. Rutishauser, "The Jacobi Method for Real Symmetric Matrices," *Numer. Math.*, vol. 9, pp. 1–10, 1966.

[61] J. D. Cutnell and K. W. Johnson, *Physics (4th Edition, Volume 1)*. 1997.

[62] L. Dintenfass, *Blood Viscosity, Hyperviscosity & Hyperviscosaemia*. Springer Science & Business Media, 1985.

[63] T. Khamdaeng, J. Luo, J. Vappou, P. Terdtoon, and E. E. Konofagou, "Arterial stiffness identification of the human carotid artery using the stress – strain relationship in vivo," *Ultrasonics*, vol. 52, no. 3, pp. 402–411, 2012, doi: 10.1016/j.ultras.2011.09.006.

[64] H. Taghizadeh, M. Tafazzoli-shadpour, M. B. Shadmehr, and N. Fatouraee, "Evaluation of Biaxial Mechanical Properties of Aortic Media Based on the Lamellar Microstructure," pp. 302–316, 2015, doi: 10.3390/ma8010302.

[65] A. V Kamenskiy *et al.*, "Biaxial mechanical properties of the human thoracic and abdominal aorta , common carotid , subclavian , renal and common iliac arteries," pp. 1341–1359, 2014, doi: 10.1007/s10237-014-0576-6.

[66] A. N. Azadani *et al.*, "Biomechanical Properties of Human Ascending Thoracic Aortic Aneurysms," *Ann. Thorac. Surg.*, vol. 96, no. 1, pp. 50–58, 2013, doi: 10.1016/j.athoracsur.2013.03.094.

[67] G. Tasca *et al.*, "Aortic Root Biomechanics After Sleeve and David Sparing Techniques: A Finite Element Analysis," *Ann. Thorac. Surg.*, vol. 103, no. 5, pp. 1451–1459, 2017, doi: 10.1016/j.athoracsur.2016.08.003.

[68] J. F. Ladisa *et al.*, "Computational simulations for aortic coarctation: Representative results from a sampling of patients," *J. Biomech. Eng.*, vol. 133, no. 9, 2011, doi: 10.1115/1.4004996.

[69] A. S. Les *et al.*, "Quantification of hemodynamics in abdominal aortic aneurysms during rest and exercise using magnetic resonance imaging and computational fluid dynamics," *Ann. Biomed. Eng.*, vol. 38, no. 4, pp. 1288–1313, 2010, doi: 10.1007/s10439-010-9949-x.

[70] P. Reymond, F. Merenda, F. Perren, D. Rüfenacht, and N. Stergiopulos, "Validation of a one-dimensional model of the systemic arterial tree," *Am. J. Physiol. - Hear. Circ. Physiol.*, vol. 297, no. 1, pp. 208–222, 2009, doi: 10.1152/ajpheart.00037.2009.

[71] M. Hafifi, "ANSYS System Coupling User Guide."

[72] T. E. Tezduyar, S. Sathe, T. Cragin, B. Nanna, and M. Schwaa, "Modelling of fluid–structure interactions with the space–time finite elements: Arterial fluid mechanics," *Int. J. Numer. Methods Fluids*, vol. 54, no. October 2010, pp. 901–922, 2007, doi: 10.1002/fld.

[73] Chiu JJ and Chien C, "Chiu JJ. (2011). NIH Public Access. Physiol Rev, 91(1). https://doi.org/10.1152/physrev.00047.2009.Effects," *Physiol rev*, vol. 91, no. 1, 2011, doi: 10.1152/physrev.00047.2009.Effects.

[74] K. M. Tse, R. Chang, H. P. Lee, S. P. Lim, S. K. Venkatesh, and P. Ho, "A computational fluid dynamics study on geometrical influence of the aorta on haemodynamics," *Eur. J. Cardio-thoracic Surg.*, vol. 43, no. 4, pp. 829–838, 2013, doi: 10.1093/ejcts/ezs388.

[75] K. Yamaga, C. Chang, T. Dobashi, M. Hasegawa, and A. Sakanishi, "Mechanical Properties of Synthetic Artificial Grafts," *Nihon Reoroji Gakkaishi(Journal Soc. Rheol. Japan)*, vol. 17, no. 1, pp. 55–59, 1989, doi: 10.1678/rheology1973.17.1_55.

[76] N. Galea *et al.*, "Novel insights by 4D Flow imaging on aortic flow physiology after valve-sparing root replacement with or without neosinuses," *Interact. Cardiovasc. Thorac. Surg.*, vol. 26, no. 6, pp. 957–964, 2018, doi: 10.1093/icvts/ivx431.

[77] F. He, L. Hua, and L. Gao, "A Computational Model for Biomechanical Effects of

Arterial Compliance Mismatch," vol. 2015, 2015.

[78] T. Mueller, F. Rengier, D. Kotelis, H. U. Kauczor, and H. von Tengg-Kobligk, "Supra aortic blood flow distribution measured with phase- contrast MR angiography," *Eur. Soc. Radiol.*, pp. 1–17, 2012.